JPL Publication 87-20

DOE/ET29372-7
Distribution Category UC-97b

AC and DC Electric Field Meters Developed for the U.S. Department of Energy

H. Kirkham
A. Johnston
S. Jackson
K. Sheu

February 1987

Prepared for
Office of Energy Storage and Distribution
U.S. Department of Energy
Through an Agreement with
National Aeronautics and Space Administration
by
Jet Propulsion Laboratory
California Institute of Technology
Pasadena, California

JPL Publication 87-20

DOE/ET29372-7
Distribution Category UC-97b

AC and DC Electric Field Meters Developed for the U.S. Department of Energy

H. Kirkham
A. Johnston
S. Jackson
K. Sheu

February 1987

Prepared for
Office of Energy Storage and Distribution
U.S. Department of Energy
Through an Agreement with
National Aeronautics and Space Administration
by
Jet Propulsion Laboratory
California Institute of Technology
Pasadena, California

Prepared by the Jet Propulsion Laboratory, California Institute of Technology, for the U.S. Department of Energy through an agreement with the National Aeronautics and Space Administration.

This publication reports on work performed under NASA Task RE-152, Amendment 203 and sponsored through DOE/NASA Interagency Agreement No. DE-AI01-79ET 29372 (Mod. A009).

ABSTRACT

This report describes two space-potential electric field meters developed at the Jet Propulsion Laboratory under the auspices of the United States Department of Energy. One of the meters was designed to measure dc fields, the other ac fields. Both meters use fiber optics to couple a small measuring probe to a remote readout device, so as to minimize field perturbation due to the presence of the probe. By using coherent detection, it has been possible to produce instruments whose operating range extends from about 10 V/m up to about 2.5 kV/cm, without the need for range switching on the probe. The electrical and mechanical design of both meters is described in detail. Data from laboratory tests are presented, as well as the results of tests at the National Bureau of Standards and the Electric Power Research Institute's High Voltage Transmission Research Facility.

ACKNOWLEDGEMENTS

The electric field meters described in this report could not have been built without contributions from a large number of people. First among these is Ken Klein, Director of the Office of Energy Storage and Distribution of the United States Department of Energy, whose financial support began the whole effort, and whose moral support helped us maintain momentum.

The authors would also like to acknowledge the help of Dick Sheller, a consultant, in the mechanical design of the dc field meter probe, and of Brad Swenson at JPL in the construction of the first prototype. Also at JPL, Joe Toczylowski and Lee Gee made the ion-generating test cage, and constructed the first prototype of the ac probe. Ke-Li Wang produced the gallium arsenide diode segments used to energize the ac field meter probe. The JPL hybrid laboratory built the hybrid ICs used in both probes, and assembled the hybrid photodiode array.

Walt Gajda, Chairman of the Electrical Engineering Department of the University of Missouri at Rolla, provided many helpful comments, and in particular helped with the solution of the ion current transient in the test cage.

The tests of the dc meter performed at the National Bureau of Standards in collaboration with Martin Misakian helped establish that the meter was performing well in a space charge environment. We gratefully acknowledge his assistance, both in the setting up of the experimental apparatus, and in the performance of the tests. We also acknowledge the assistance of Dr. Misakian in the calibration of the ac meter.

Field tests of the dc meter were performed at the High Voltage Transmission Research Facility of the Electric Power Research Institute. We appreciate the help of Gary Johnson in arranging for us to have laboratory time at that facility. The contribution of Bill McGonigle, also of HVTRF, in furnishing us with HVTRF data, in helping us with our apparatus and for being, at times, a test subject, is also acknowledged with thanks.

Two local utilities provided support in the development of the field meters. We would like to thank Mike Reavis and Tin Fong of the Los Angeles Department of Water and Power for their help in testing the dc meter at a site near Sylmar. We thank Henry Lee, acting General Manager of the Pasadena Department of Water and Power for arranging for us to have a 17-kV transformer. This was the *sine qua non* of realistic tests of our ac field meter.

Finally, the authors thank Ms. Charlotte Marsh, our editor at JPL, for her careful reviews of the manuscript, and her considerable help with its preparation.

PREFACE

This report describes the work performed at the Jet Propulsion Laboratory on the measurement of electric fields in air. The work was sponsored by the Office of Energy Storage and Distribution of the United States Department of Energy.

Throughout the 'seventies and early 'eighties there was continuing public interest in the possible biological issues associated with the transmission of electrical power. Responding to this, the Department of Energy, as well as some electric utilities, sponsored research to investigate the effects (if any) that electric fields had on animals, both large and small.

Some of the experimental work was done indoors, under well-controlled conditions. Other investigations were carried out in an uncontrolled outdoor environment. Unless the field-producing apparatus and the experimental subject can be accurately modelled, the field actually experienced by the organism cannot be known. Further, charged particles of animal hair or fur could modify the field or space charge environment in an indoor facility in a different way than in the outdoors. There is, then, some advantage to being able to measure the actual field with the test subject present in this kind of experiment.

In the case of dc fields, this was not possible prior to the work described in this report. The state of the art in field measurement was as follows. Alternating fields could be measured in air with devices that would characterize the undistorted field generated by a power line quite accurately. The distorted field near a test subject could be measured with less accuracy. Direct fields could be measured in the plane of the ground, both in the absence and the presence of ions. While some field measurements above ground had been made, the equipment needed to measure the dc field near a distorting object did not exist.

The group at the Jet Propulsion Laboratory was charged with the application of the technology of fiber optics to the problems of power system measurements. In view of the issues discussed above, it was decided that an early application would be the use of a fiber optic measurement system to make possible the measurement of dc electric fields in air. This work is described in Part 1 of the report. As the work on a dc field meter progressed, it became clear that it would be possible to produce an improved ac field meter using much of the same hardware. This task was therefore added to the goals of the work during 1986, and is described in Part 2.

CONTENTS

LIST OF FIGURES

EXECUTIVE SUMMARY

For some while there has been public and scientific interest in the possibility of biological interactions from high voltage power lines. Universities and utilities are conducting experiments to study the issue.

When the possibility was first raised, no specific mechanism for an interaction between the high voltage power line and a biological organism was proposed. However, it seemed reasonable to suppose that the stronger the electric fields associated with the power line, the greater the interaction with the biological subject. Therefore, in order to understand any biological interaction discovered, the field conditions under which the interaction took place must be specified. This is not an easy task, since the biological subject modifies the electric field environment into which it is placed.

A field which is uniform can be analyzed mathematically. This is not possible if the field is made nonuniform by the biological subject. Mathematical models of biological specimens are quite limited. Consequently, there existed a need for the experimental measurement of electric field. In the case of dc lines, there was no equipment that would permit the measurement of an electric field above the surface of the ground in the presence of a distorting body.

Under the sponsorship of the Department of Energy, Office of Storage and Distribution, a group at the Jet Propulsion Laboratory has met this need. They have developed the instrumentation required to measure direct current electric fields above ground in the presence of distorting objects.

The field meter consists of two parts. The sensing is performed by a probe, which contains all of the components of a conventional cylindrical field mill. The data are displayed by a separate meter. The two are interconnected by fiber optics, so that the probe is electrically isolated from the display unit. The probe can thus be placed on an insulating pole and used without a ground reference. This enables electric field to be measured at space potential.

The two semi-cylindrical electrodes which comprise the field mill are rotated in the field. The charge induced on their surface by the electric field passes from electrode to electrode as the electrodes rotate, producing a current proportional to the electric field. This current is then telemetered to the display unit, or receiver, by means of a fiber optic umbilical. At the receiver, the signal representing the electric field is resolved into vertical and horizontal components. Each component is separately displayed on a digital panel meter.

The probe electronics is contained in one hybrid integrated circuit, which rotates as part of the probe. It produces optical pulses at a low duty cycle with a center frequency of 90 kHz. This pulse rate is frequency modulated by the current signal which represents the electric field. The light pulses are launched into a fiber optic coupler which connects them to a non-rotating fiber in the fixed part of the probe. By this means the use of slip-rings is avoided. Motive power for the rotation is furnished by a compressed-gas turbine, similar to the turbine used in a dentist's drill. Figure ES-1 is a photograph of the probe.

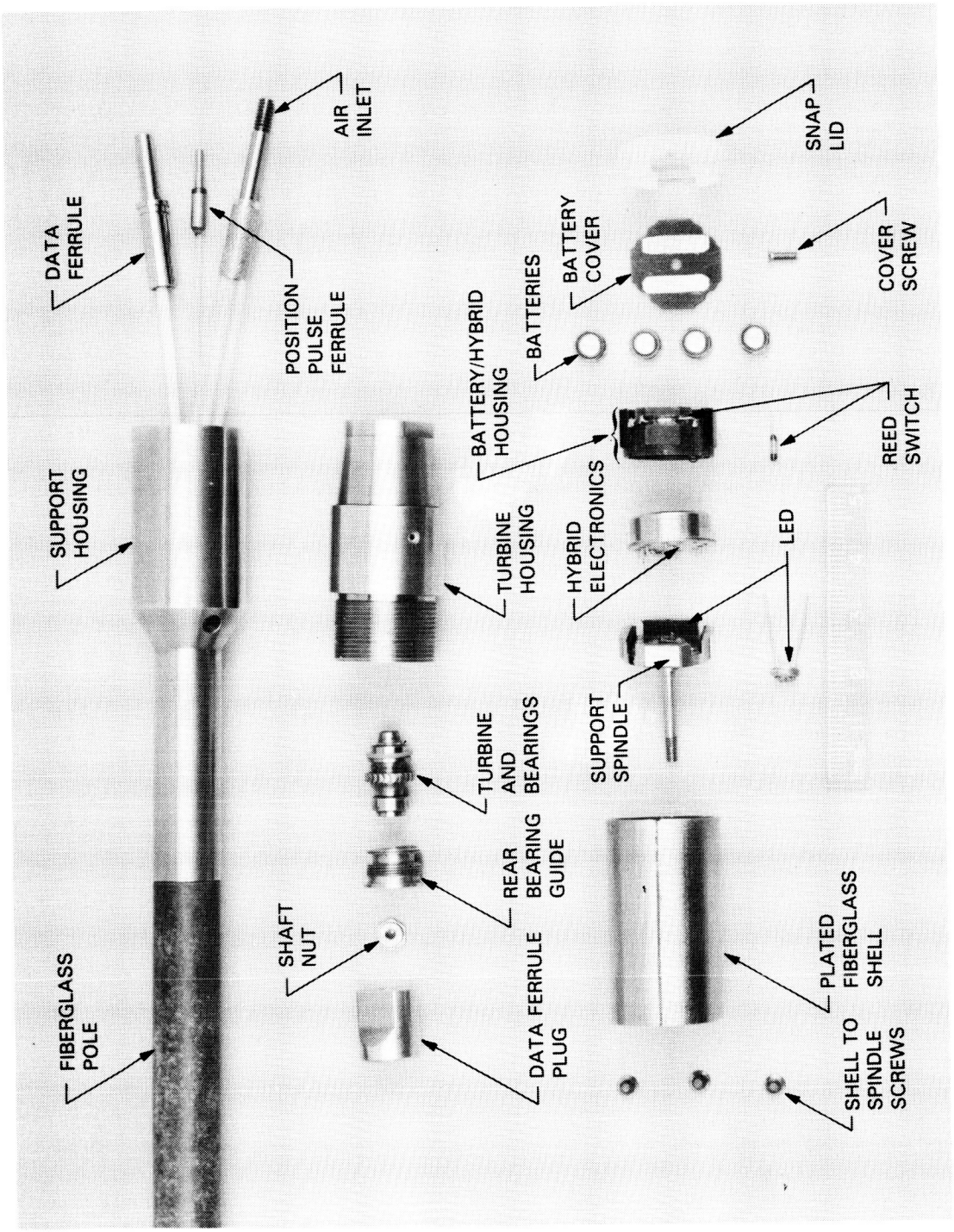

Figure ES-1. Photograph of dc field meter probe (disassembled)

In the receiver, the modulating waveform is recovered by means of a phase-locked loop FM discriminator. The signal amplitude is measured by coherent detection, triggered from a reference pulse derived from a small mirror spot at the edge of one of the rotating electrodes. Coherent detection is used to obtain maximum dynamic range. There is no mechanism in the probe for range switching. Nevertheless, the meter has a dynamic range of about 100 dB. This means that the meter can measure fields from the level of the normal atmospheric field (a few hundred V/m) up to the range at which the air breaks down as an insulator (about 30 kV/cm)[1].

For the measurement of dc electric field, two problems had to be solved which do not arise in the case of ac fields. They are self-charge and pole leakage.

Self-charge arises because the field environment in the vicinity of high voltage dc transmission lines is characterized not only by the electrostatic field due to the potential of the conductor, but also a space charge generated by the breakdown of the atmosphere at the surface of the conductor. This space charge has no counterpart in the ac transmission line. The air breakdown caused by local field intensification at the surface produces ions of both positive and negative polarities. Whether the line is energized positively or negatively, one of these ion species will be attracted back to the surface of the line, and the other will be repelled. In either case, therefore, the line appears to be a cathode, i.e, a source of charge. The space charge so produced drifts away from the cathode under the influence of the electric field. Because it is in atmosphere rather than vacuum, collisions between the charged ions and atmospheric molecules result in the equivalent of a large viscous drag. Rather than being accelerated by the field, the ions follow the electric field to the surface of the ground, or to any distorting object near the surface of the ground. They would therefore also collect on the probe of the dc field meter.

In complete isolation, the dc field meter is incapable of measuring any charge accumulated in this way. However, as the meter is designed to be used in the presence of another object in the field, it is necessary to consider the effect of the image of the charge on the probe caused by the presence of the other distorting object. The probe can indeed measure the charge on its image. Fortunately, the self-charge process is self-limiting. The total field which results can be thought of as the sum of two separate components. There is first the electric field into which the probe is placed; secondly there is the electric field due to the charge on the probe. Superposition can be used. The field at the top of the probe will be less than the field at the bottom because at the top of the probe the two fields tend to cancel. At the bottom they tend to add. When the self-charge component of the total field is equal to the external component, the net field at the top of the probe will be zero. At this point no further self-charge can be acquired.

---

[1] In a uniform applied field of 15 kV/cm, the field at the surface of the cylindrical electrodes is 30 kV/cm, because the metallic electrodes intensify the field. Because of this, the measurement of fields above this value is not possible. With a spherical probe (such as the ac meter described below) this geometrical field enhancement limits the measurable field to 10 kV/cm.

The condition for equilibrium depends on the magnitude of the external field. The magnitude of space charge or ion current determines only the time taken to reach equilibrium. Calculations show that at large distances from conducting objects, the equilibrium self-charge produces an error equivalent to making the measurement of field at a location different from the axis of the probe by about one probe diameter. In all practical applications this can be considered to be a very small error. As the probe approaches a conducting surface, the error increases, reaching about 10% at a distance of 5 probe diameters. This, too, is an acceptable error. Note that these errors drive the probe design towards a smaller diameter.

The other error in the measurement of free space electric fields is caused by leakage down the pole holding the probe. In the prototype dc field meter, the probe was held in place by a fiberglass pole two meters long with a resistivity of the order of 10^{16} Ω/m. For most ordinary uses, such a material could be considered to be a very good insulator. For the measurement of dc fields, it is quite inadequate. Consider that the probe is inserted into an electric field of strength of 10 kV/m. At a height of one meter above the ground, the probe is at a potential of 10 kV. The other end of the fiberglass rod holding the probe is at ground potential. (Usually an operator is holding that end.) A current will flow down the pole, because of leakage. If the probe has a capacitance to ground of a few pF and the pole resistance is of the same order as mentioned above, then a time constant in the order of a minute results. After a minute or so, the potential on the probe is no longer 10 kV, but begins to approach ground potential. The result of this change in potential of the probe is field intensification. The probe will now measure an enhanced field. The amount of enhancement depends on the geometry of the field above the probe.

The current down the pole is not large, just a few pA, but it must be supplied from somewhere other than the probe itself in order to maintain the capability of an accurate measurement. The solution used in the DOE field meter was to use a small polonium alpha source located on the probe housing. This source produces alpha particles which ionize the atmosphere in the vicinity of the probe and, in essence, connect the probe to the atmosphere at that point. With the leakage current supplied by the ion source, field readings can be made with the probe at quite large potentials.

To take full advantage of the field plotting capability of the field meter, a novel photographic technique was employed to record the data. Two cameras with synchronized shutters were used. One camera recorded the position of the probe and the subject, so that their relative locations could be measured later. The other camera recorded the reading on the field meter at the same time. Data recorded in this way were entered into a computer program later, and field plots of the dc electric field around human subjects standing under transmission lines were obtained.

The conventional way to plot field vectors is to have the length of the line representing the vector proportional to the magnitude of the vector. We have instead adopted an inverse relationship. By having shorter lines where there is a more intense field, the plot resembles a normal field plot. In this case, the length of the line can be thought of as proportional to the spacing between equipotential lines. Figure ES-2 is an example of such a field plot.

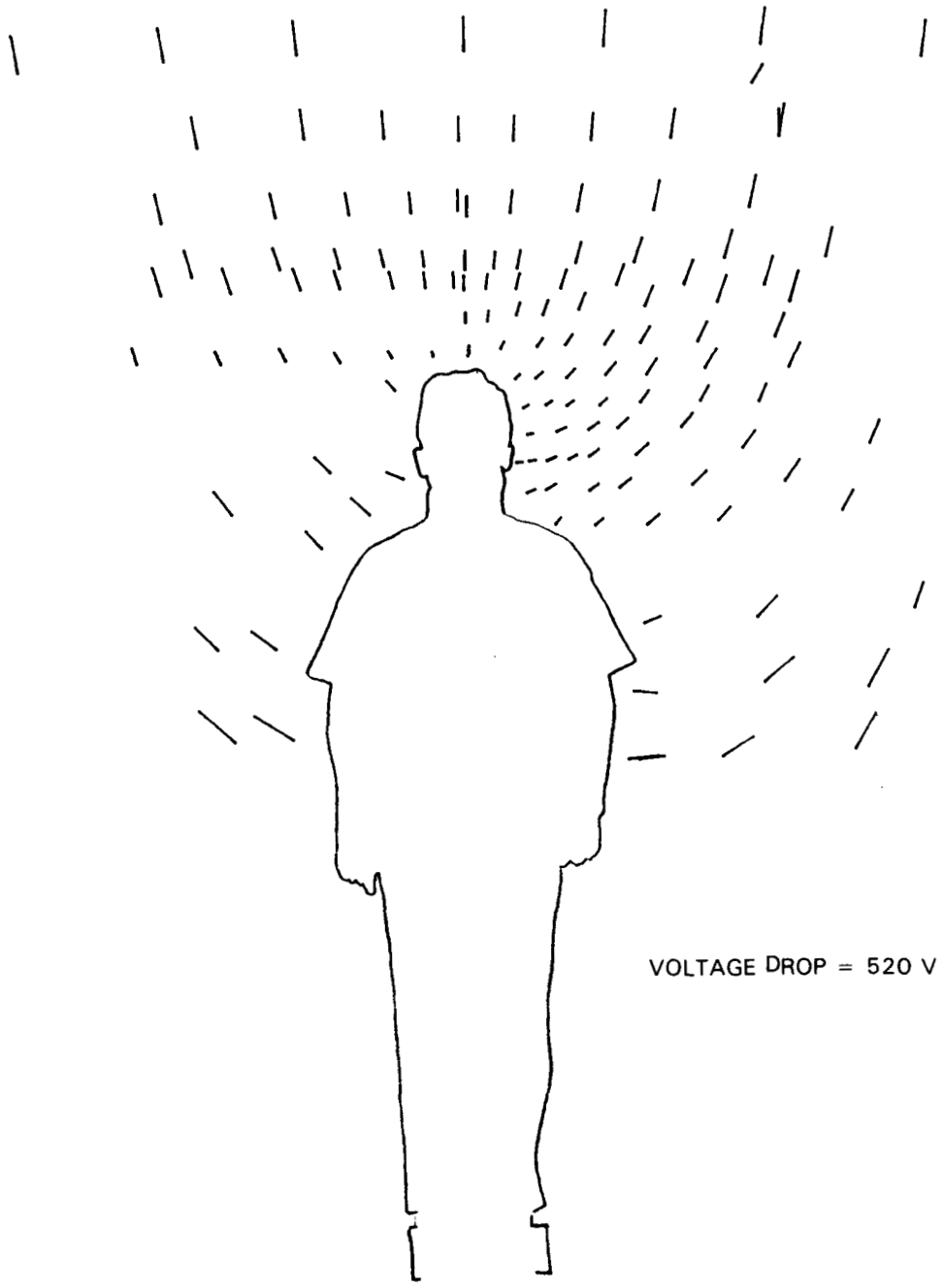

Figure ES-2. Electric field around human subject under transmission line

The original intention of the work on the dc electric field meter was to bring it to a state of equivalence with ac field meters. These meters have existed for some time and are reasonably commonplace in transmission line research. However, the dc field meter produced under the auspices of DOE is much smaller than the ac field meters that are used in transmission line work, and it has a much larger dynamic range. It therefore seemed a natural extension of this work to use the same technology to develop a small ac meter.

An ac field meter was therefore built using as much as possible of the approach that had been used with the dc meter. The field meter probe is spherical, and two centimeters in diameter. A spherical shape has the advantage that it causes the minimum field intensification and it permits an absolute calibration to be made. The ac field meter has a large dynamic range, approximately the same range as the dc field meter, again obtained through the use of coherent detection. The coherent detector operates through a phase-lock loop synchronized to the signal itself since there is no reference pulse available. Figure ES-3 shows the ac field meter probe.

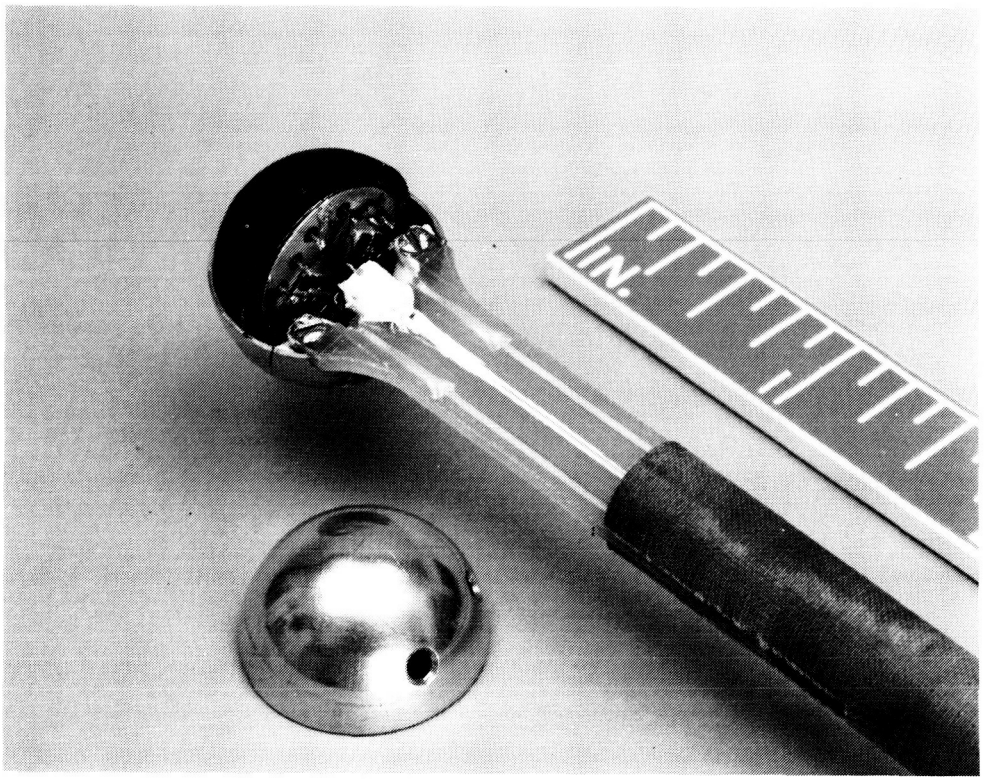

Figure ES-3. Ac field meter probe

In order to keep the size to a minimum, the probe of the ac field meter is energized optically. Two high power lasers (each generating up to 50 mW of optical energy) send infrared energy into the probe over separate fibers. Each fiber illuminates a small hybrid array of gallium arsenide photodiodes. These arrays produce the voltage necessary to energize the hybrid IC electronics. The photodiode arrays are shown in Figure ES-4.

The ac field meter has been used to measure free-body ac fields in the range of 10 V/m up to about 2 kV/cm. As in the case of the dc field meter, such a wide range permits use of the probe in an environment with unknown field, without the necessity to approach the probe in order to change its range. This means that operation is not only convenient, but it is also inherently safe.

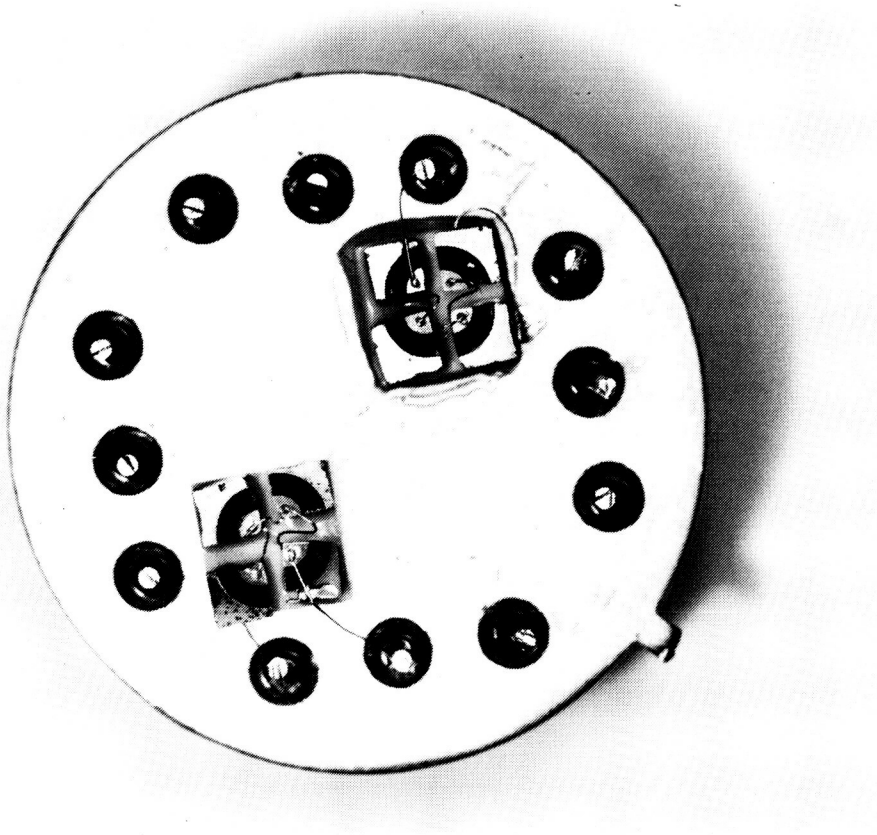

Figure ES-4. Photodiodes used to energize probe electronics

At the present time, the electric field meters described here are among the smallest and most accurate meters ever made. The dc meter is the first such meter to allow free-body field measurement. Measurements are now possible that could not have been made before. The ac meter is smaller than the most commonly used ac field meters by a factor of a thousand or so. This means that measurements can be made much closer to conducting bodies than was previously possible. Measurements made using these meters should enable the mathematical models of field effects to be refined, and should lead to greater understanding of the phenomena associated with electric fields.

Modifications to the field meters are planned, so they can measure magnetic fields instead of electric. Although the electrical isolation necessary for measurement of space-potential electric fields will not be required, it will not be a disadvantage in the magnetic measurement. The safety advantage of an isolated meter in a high voltage environment will be retained.

PART 1

THE DC FIELD METER SYSTEM

1. THE DC FIELD METER SYSTEM

1.1. Introduction

For some while there has been interest in the effects of the electric fields associated with electric power transmission. As transmission lines were designed and built to operate at higher and higher voltages, their presence became more noticeable. A casual observer can hear the audible effect of rain on a high voltage alternating current transmission line, and sometimes the electric field itself can be sensed. A number of laboratories throughout the world have undertaken to investigate the effects, if any, of the fields associated with the transmission of electric power. These effects include the production of audible noise already alluded to, the generation of radio interference, and effects on biological systems.

These studies were conducted, in the main, to investigate the effects of alternating electric fields. Almost all the transmission lines in the world carry alternating current (ac), so this was a reasonable place to begin. However, under some circumstances, the transmission of power by direct current (dc) can be more efficient and more economical, and several large dc lines have been built. A natural extension of the work on ac field effects was to perform similar studies for dc fields.

It would be fair to stress, at this point, that the biological studies were faced with a very difficult problem. The authors of this report are all engineers or physical scientists. Under ordinary circumstances, any unknown in our world can be calculated using well understood theoretical concepts. The same cannot be said of the early attempts to investigate the impacts of the electric fields associated with the transmission of electric power. No satisfactory mechanism for biological impact had been proposed. No clear-cut experimental result had demonstrated a biological effect. The work was definitely of a pioneering nature.

In the scientific world, when you don't know the answer or the method, you have to perform an experiment. Biological experiments are among the most difficult ones to perform because many variables, aside from the ones that are the subject of the study, can affect the outcome of the experiment. Under such circumstances repeated studies, with controls and carefully monitored conditions, are the only way that an increased understanding can be gained. The method is simple in principle: experimental subjects are exposed to electric fields for some amount of time, and later examined for possible effects. The subjects might be linemen working near high voltage equipment, or farm animals grazing under real transmission lines, or small animals in indoor test apparatus.

Naturally, since electric field is the parameter under investigation, it is essential to be able to measure or calculate the electric field that the subject experiences. The branch of electrical engineering known as field theory can describe the electric field at any point in space provided the correct "boundary conditions" are given. Closed form mathematical solutions to field problems are given in all the standard texts for boundaries that have an appealing degree of symmetry. In the case of the animals that graze under

transmission lines, it is not possible to transform the problem to one of suitable symmetry. Closed form solutions are not possible, and even numerical solutions are difficult. The presence of space charge considerably complicates the situation.

A much more satisfactory solution is the experimental measurement of the electric field environment as part of the study. In this way, the effects of variables that are not well understood (atmospheric humidity, temperature, etc.) can be accommodated along with those parameters that are known to be important (such as voltage and conductor-ground spacing). Appropriate instrumentation is essential.

For studies of ac lines, a number of instruments have been developed that can measure the value of the electric field under a transmission line, either at the surface of the ground or above it. Instruments with sensing elements that are isolated are known as free-body or space-potential instruments, because they permit the measurement of the field at the potential of the space in which they are used, without affecting that potential in any significant way. For dc lines, the situation has been rather different. Only the ground-level field of a transmission line could be measured. Some free-body instruments have been built that did permit above-ground fields to be measured (Smiddy and Chalmers, 1958; Gathman, 1968), but these were large instruments, built for atmospheric investigations, and were quite unsuited to the investigation of the electric fields near transmission lines. Other instruments developed specifically for power line measurements (Maruvada, Dallaire and Pednault, 1983) permitted above-ground measurements, but were themselves grounded. To use these instruments, the field being measured had to be undisturbed by the presence of another object, such as an experimental animal.

When the United States Department of Energy decided to fund a program applying fiber optics technology to power system measurements, the problem of the space-potential measurement of dc fields above ground was one that was considered worthy of study.

The first dc electric field meter that could measure the value of transmission line fields above ground even in the presence of another object was designed and built at the Jet Propulsion Laboratory in 1985. A number of measurements were made with this instrument that demonstrated the capability of above-ground measurement of nonuniform fields (Johnston, Kirkham and Eng, 1986). Electric fields ranging in value from less than 1 kV/m up to some tens of kV/m were easily measured, and the field around a test subject was measured and plotted graphically.

The instrument was built in two parts, interconnected by fiber optics. A rotating probe, on the end of a fiberglass pole, actually sensed the field, and communicated information about its direction and magnitude to a receiver nearby. The chief drawback to the instrument was its size. With a diameter of about 8 cm, the probe could not furnish accurate field measurements closer than about 30 cm to a conducting surface. To make it more useful, its diameter would have to be reduced. Other improvements were also considered.

1.1.1. Sensor Development Approach

Results with the prototype field meter (the beercan sensor[1]) were encouraging. The measurement of dc electric fields in air away from the surface of the ground had been demonstrated, in the presence or absence of charged ions. Yet the measuring system, the probe and the receiver taken together, was still very much a prototype. Two aspects of the system in particular required improvement. First, there was the need, mentioned above, to reduce the diameter of the probe in order to minimize the errors caused by the image charge. Second, there was a need to improve the dynamic range of the receiver. The dynamic range of the system had been established as about 50 dB, but to obtain this range, a commercial lock-in amplifier had been used. If copies of the dc field meter were to be useful in making field measurements, a less expensive and more portable measuring system had to be developed.

A number of trade-offs and improvements seemed indicated. For example, as the diameter of the probe is reduced, the current in the first stage of the electronics is reduced. If this reduced current is not to cause an increase in the minimum field that can be measured, some means of compensating for it must be found. Increased speed of rotation is such a mechanism. However, the electric motor drive used in the beercan probe was not capable of producing the speeds needed, nor was it efficient enough to be practical. Instead, an air turbine of the kind used in a dentist's drill was used. Such turbines are rated to operate at speeds up to 300 000 rpm, but a much lower speed was adequate for our application. Table 1 shows the planned sequence of events.

TABLE 1. DEVELOPMENT SEQUENCE FOR DC FIELD METER

	Field meter version	
Parameter	Beercan	Final
Diameter (cm)	8	2
Length (cm)	20	10
Speed (rpm)	600	100 000
Motive power	electric	air turbine
Electronics	discrete IC	hybrid IC
Electronics power	batteries	optical
Detector	envelope	synchronous

Performance requirements were never formally determined. Unofficially, it was hoped to be able to measure dc electric fields ranging in magnitude from the normal outdoor ambient value of about 100 V/m up to the point at which the air

[1] Because of the general appearance of the probe (cylindrical, 20 cm long and 8 cm in diameter) the prototype device became known as the beercan sensor. This name has become so ingrained that to attempt now to use another term to describe the meter would be churlish. We shall therefore retain the name.

itself breaks down, about 30 kV/cm. The measurement should be made with an accuracy of a few percent, with or without ions in the field being measured. It will be shown later that we came very close to achieving these performance objectives.

1.2. Design of Field Meter

This section discusses the design of the dc field meter system. We begin with an overview of how the dc field meter works. Figure 1-1 shows a generalized measurement system of the type used in the dc field meter.

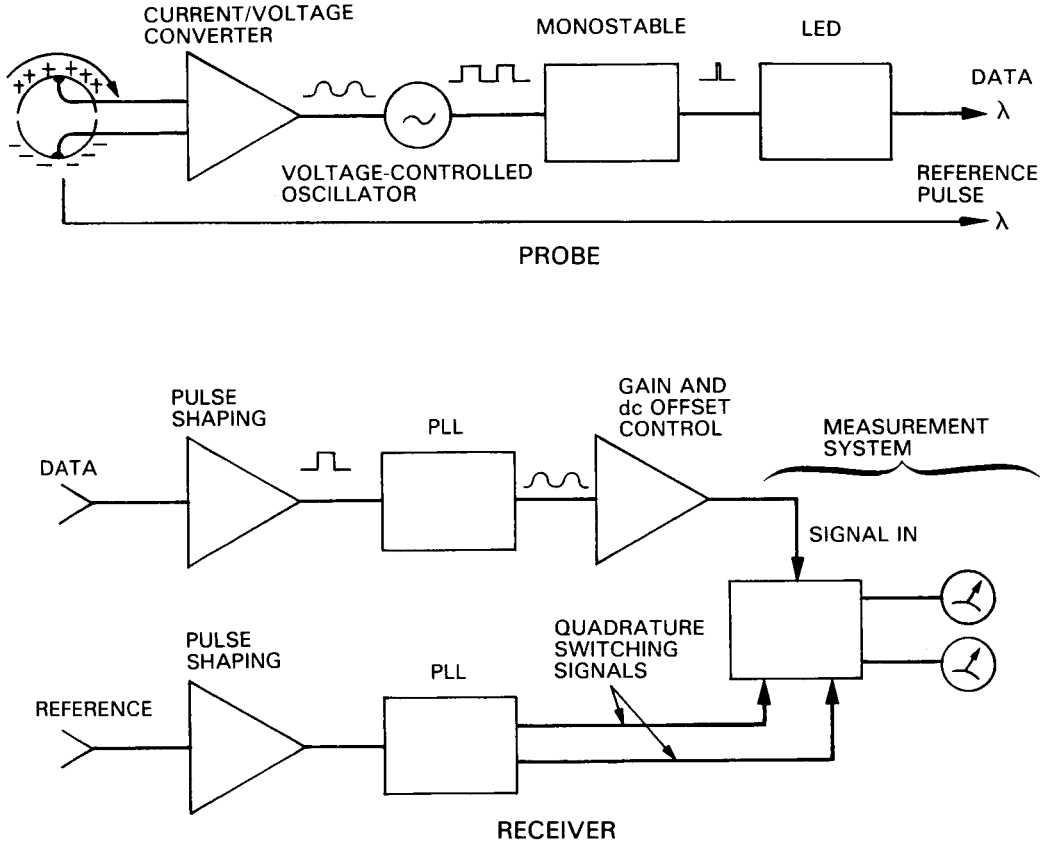

Figure 1-1. Generalized measurement system

The electric field to which the probe is exposed induces a charge on the surface of the probe. The charge is proportional to the magnitude of the field. As the electrodes rotate, the charge remains fixed with respect to the field, and so it passes from electrode to electrode by way of the input to the first stage of the amplifier. This stage converts the current at its input to an alternating voltage with magnitude proportional to the field-induced charge. The voltage modulates a voltage controlled oscillator (VCO). Narrow pulses are generated by the VCO and converted into optical pulses by a light emitting

diode (LED). These pulses are injected into an optical fiber, and transmitted to the receiver portion of the system.

At the same time, an optical pulse is generated once each revolution for angle reference purposes. In the beercan version, the pulse was generated optically, and encoded onto the data pulses electronically. In that design, only one fiber was required between the sensor probe and the receiver, and the separation of the two pieces of information was electronic. In the miniaturized probe, the pulse is generated by a small reflective spot on the edge of the rotating shell, which reflects light back into the fiber that illuminates it. This is a different fiber than the one that carries the data. A directional coupler separates the reflected energy from the illumination. This leads to a much simpler design for the probe electronics, which is important in terms of reducing the size and power consumption of the hybrid IC used in the probe.

The voltage signal that modulates the probe VCO is regenerated in the receiver by an identical IC configured as a phase locked loop (PLL) detector. It is functionally similar to an fm detector in a radio. The receiver is in fact recovering the modulation from an fm carrier which has been encoded as a low-duty-cycle pulse train for optical transmission.

Synchronous detection is used to obtain maximum dynamic range, and to ease the filtering requirements in the receiver. Compared to the usual synchronous detector, such as might be used in a radio receiver, this system has the advantage of a strong synchronizing pulse, with an amplitude that is independent of the signal being detected. This pulse is used to generate the switching signals for the synchronous detector, by means of a second PLL. The switching signals for two quadrature components are generated.

In order to display the data, or to provide outputs suitable for data loggers, low-pass filtering is performed on the detected signals, as is standard practice in phase-locked detection. This effectively converts the output of the synchronous detectors into a dc voltage whose amplitude is proportional to the appropriate component, in-phase or quadrature, of the input. Digital panel meters are used for data display in the prototype receiver.

The remainder of this section will describe the design of the field meter in detail. Three very different aspects are covered. The mechanical design of the probe is discussed in Section 1.2.1, the probe electronic design is described in Section 1.2.2 and the receiver design is the topic of Section 1.2.3.

1.2.1. Mechanical design of probe

The major mechanical design goals were:

1. The outside diameter of the probe was to be as small as possible, and the length was to be as short as possible.

2. Some type of air turbine would be used to spin the rotating section of the probe (an electric motor was out of the question due to lack of space for batteries).

3. A rotational speed high enough to provide sufficient induced current from the electrodes, so that electrometer amplifier input drift is not a significant source of error.

4. A passive type of position pick-off system to reduce both the electronics package size and the battery requirements.

6. Easy access to batteries, electronics package, ferrules, turbine motor, etc. for replacement and service.

8. A means to turn on and off the electronics. Even the smallest commercially available switch is quite large.

1.2.1.1. Turbine Drive Design

After considering the complexity and cost involved in the design of a turbine motor from scratch, it was decided that it would be simpler to modify an existing turbine. Suitable turbine motors are used in dental-drill handpieces. The drill turbine, together with its bearings, could be removed from its handle (see Figure 1-2) and an external shell designed to provide air transfer to the housing and accommodate the fiber optic ferrules used for the data link and the position pulse. The drill collet, normally used to hold a dental burr, was found to be inadequate to hold the probe's rotating spindle assembly, and another method was used.

The inside of the custom turbine housing was modeled very closely after the original dental handpiece to achieve proper bearing placement, adequate air flow, etc. Measurements were taken directly from a dissected handpiece.

The first drive unit was machined from brass and tested by using it to spin an aluminum spindle (which approximated the expected weight of the sensor's rotating assembly). At speeds above 20 000 rpm, the collet failed to hold the spindle securely, causing it to wobble violently. The spindle's mounting shaft was bent.

The problem was solved by enlarging the diameter of the shaft passing through the turbine bearings. The new shaft, approximately twice the diameter of the original dental drill burr, was threaded at its end and mounted to the turbine with a nut, eliminating the need for the collet.

The final drive unit was mechanically tested at speeds up to 60 000 rpm without failure using the mock-up aluminum spindle.

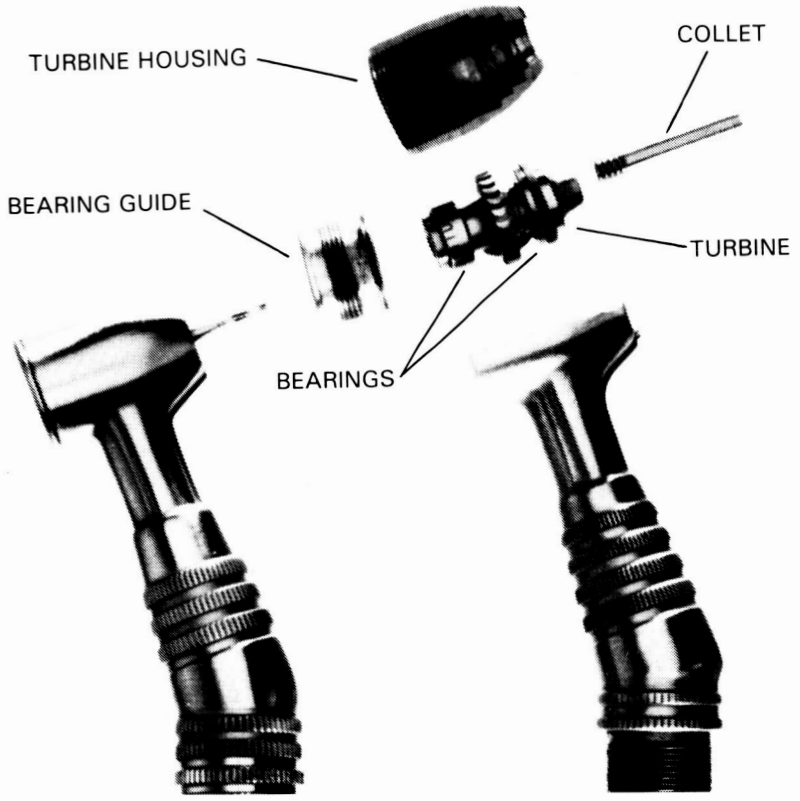

Figure 1-2. Photograph of dissected dental drill handpiece

1.2.1.2. Fiber Optics - Mechanical Considerations

The drive unit design was finalized with the addition of fiber optic ferrules and a brass housing. The fiber ferrules are derived from standard optical fiber connecter hardware by minor machine-shop modifications. One ferrule couples the optical data signal from the rotating element, while the other acts as the fixed optical element of the position sensor.

The data ferrule, a modified SMA connector, is mounted in a brass plug which fits inside the turbine housing directly behind the turbine on the central axis of the probe as seen in Figure 1-3. This ferrule is butt-coupled to the rotating fiber in the shaft. Its proximity to the end of the shaft is adjusted with the aid of a set-screw located in the brass plug.

The position reference ferrule was mounted at a nine-degree angle in order to point it at the edge of the rotating shell.

A brass housing screws onto the rear of the turbine assembly and tapers down to mate to a 3/8 inch fiberglass support tube. The housing and support tube conceal and protect the fiber optic cables and air hose.

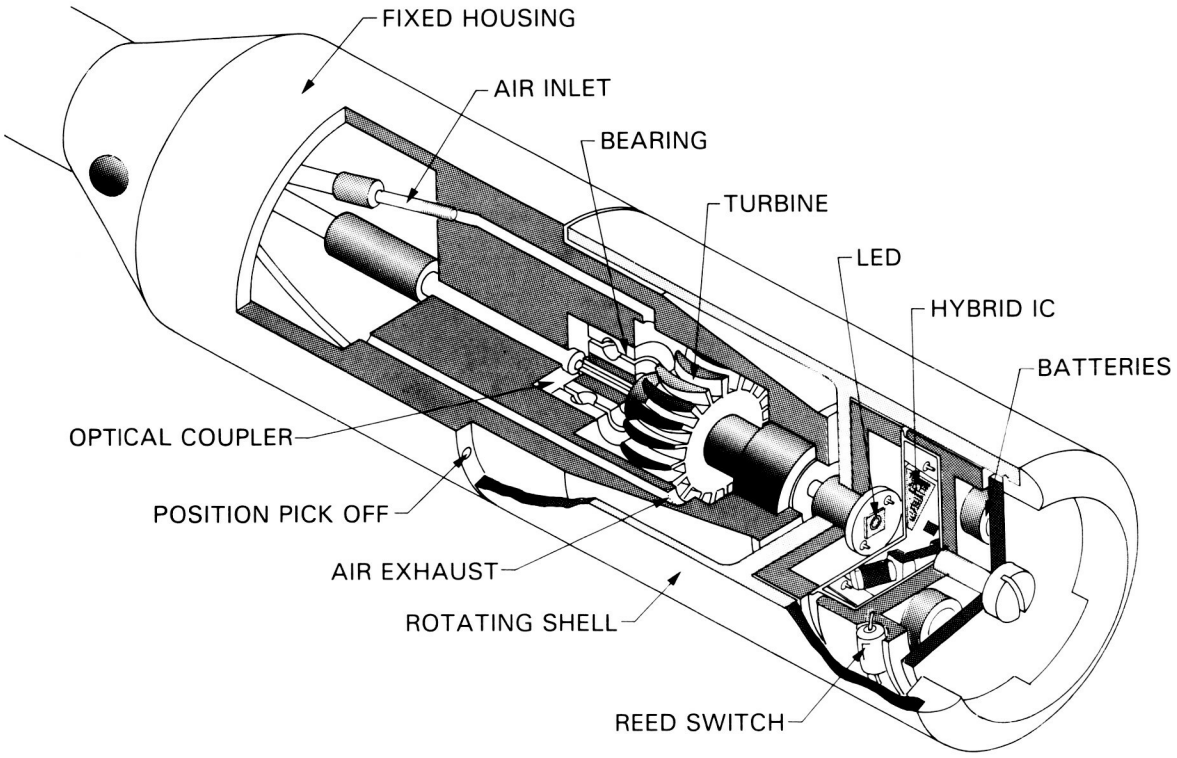

Figure 1-3. Isometric view of sensor probe

1.2.1.3. Rotating Assembly

The rotating section of the sensor contains all of the field sensing electronics. The major parts of the rotating probe are the fiberglass shell with its plated electrodes and nylon snap lid; the electronics package with its hybrid micro-circuit, batteries and power switch; and the support shaft, or spindle, with its internal optical fiber and light emitting diode.

The shell was machined from a solid piece of flight-quality[1] fiberglass, a material commonly used as the base material in the manufacture of printed circuit boards. Fiberglass was chosen for its weight, its physical and dielectric strength, and because it could be readily plated.[2] The shell is cylindrical, measuring 0.75 inches (19 mm) in diameter and 1.30 inches (33 mm) in length, and has a minimum wall thickness of 0.070 inch (0.18 mm).

---

[1] The term "flight-quality" is loosely applied at JPL to components that have been qualified for spaceflight. In this particular instance, the material was Type GE epoxy glass laminate, NEMA Grade FR4.

[2] One drawback to the use of fiberglass in this application, however, is that very careful machining is required. Some difficulty was encountered with lower quality fiberglass: it tended to crack during the machining. In future versions of the field meter, the use of Delrin or other plastic material might be explored.

The end of the shell closest to the turbine has a nine degree beveled surface which, when plated and masked, becomes the mirror used in the position pick-off system. The inside surface at the outboard end of the shell has four raised flats which orient and snugly hold the shaft, the electronics package and its battery cover. Grooves were cut near the end of the shell to accept the prongs of a nylon snap lid. The snap lid holds the electronics package in place while also providing a smooth rounded surface at the end of the shell.

The semi-cylindrical field sensing electrodes and the mirrored surface of the position sensor are created in several layers by standard plating processes. After the final layer is plated, the rear surface of the shell is polished on a special jig which has a nine-degree beveled surface. This produces the high lustre needed for the mirrored surface of the position sensor. Gold is used for the final plate, primarily to prevent the mirror from tarnishing. After plating, the inside surface of the shell is painted with conductive paint to shield the electrodes from the internal housing. This reduces the effect of capacitive coupling between the electrodes and the stationary turbine housing.

The electronics package incorporates the hybrid circuit in its TO-8 can (diameter 0.6 in, 14 mm), four miniature silver-oxide batteries, a miniature reed switch and the necessary interconnection wires and foils. The package frame itself, made from Delrin 500-AF, is designed to fit snugly inside the fiberglass shell and is held in place by the nylon snap lid.

An extremely good connection to the batteries is necessary to prevent electrical noise, or microphonics, caused by probe vibration. The connection is made by gold foil pads cushioned with neoprene rubber and bonded into the battery holes. Two additional connection foils are glued to the battery cover, which is held on by a screw that is tightened until the neoprene compresses, making excellent battery connections.

A microminiature reed switch was used to activate the electronics. It measures only 0.055 inch (1.4 mm) in diameter and 0.210 inch (5.3 mm) long. It is glued to the side of the electronics package and oriented so that its movable blade will throw outward in response to centrifugal force, making contact with its stationary blade when the probe spins at speeds above 20 000 rpm.

The shaft, machined from 303 stainless steel, is threaded at one end so that it can be secured to the turbine with a nut. At the opposite end of the shaft is a mounting bracket for the fiberglass shell. A 0.025 inch (0.63 mm) hole has been drilled the entire length of the shaft to accommodate a 400 μmeter optical fiber, which is polished at both ends before installation. An infrared LED is centrally mounted in a recessed area of the bracket with its emitting region located extremely close to the fiber. The LED, a Hitachi HE8403R, is small, lightweight, and has a 419 μmeter diameter domed lens which focuses its light very efficiently into the 400 μmeter fiber. With the aid of an optical power meter attached to the threaded end of the shaft, the LED is positioned for maximum power out of the fiber before it is bonded in place.

All electrical interconnections between the hybrid, batteries, switch, LED and electrode pads are made with 38 gauge enamelled copper wire soldered to each component.

1.2.2. Probe electronics design

The electronics section of the miniature probe is a simplified version of that used in the beercan probe. All of the electronics is contained in the probe's rotating section. The active position reference encoding circuitry of the earlier design was not used. This lowered the chip count and simplified the production of a hybrid integrated circuit. The power requirement was also reduced.

1.2.2.1. Circuitry

The block diagram shown in Figure 1-4 illustrates the principle of operation of the probe electronics. The semi-cylindrical electrodes, plated on the outside of the fiberglass shell, are connected to an operational amplifier configured in a charge measurement (integrating) mode. When the sensor rotates in a dc field, a current is induced between the two half-cylinders. This current is proportional to the rotational frequency as well as the field intensity. Capacitive feedback networks remove the rotational frequency-dependence and set the gain of the amplifier. Thus, while the input current for a given field intensity increases as the speed increases, the amplifier gain decreases at 6 dB per octave, and exactly compensates.

The circuit of the probe is shown in Figure 1-5. The values were selected to provide optimum performance, taking into consideration the small electrode size and high speed of rotation. The small size means that the induced charge will be less than that produced by the beercan sensor, but the faster speed increases the current proportionally. Although the amplifier was initially designed for an expected rotation frequency of 1666 Hz (100 000 rpm), the values used provide frequency independence of the scale factor at any speed above about 300 rpm. In other words, the amplifier produces a constant voltage for a constant field over a very wide speed range.[1]

The operational amplifier, an RCA 3420A, was selected for its high input impedance and low bias- and drift-currents.

The output signal from the operational amplifier modulates a voltage-controlled oscillator (CD4046) with a center frequency of 90 kHz. The output from the VCO is a frequency-modulated (FM) square-wave, whose modulation level is proportional to the magnitude of the sine-wave input. As described below, the output from the VCO is converted to very short pulses. This reduces the duty cycle of the LED used to transmit the signal out of the probe and this, in turn, reduces the overall power drain, a vital consideration for an electrically isolated probe.

---

[1] This was important, because the hybrid integrated circuit was being fabricated at the same time as the probe. Consequently, the actual speed of rotation was not known until after the hybrid was completed.

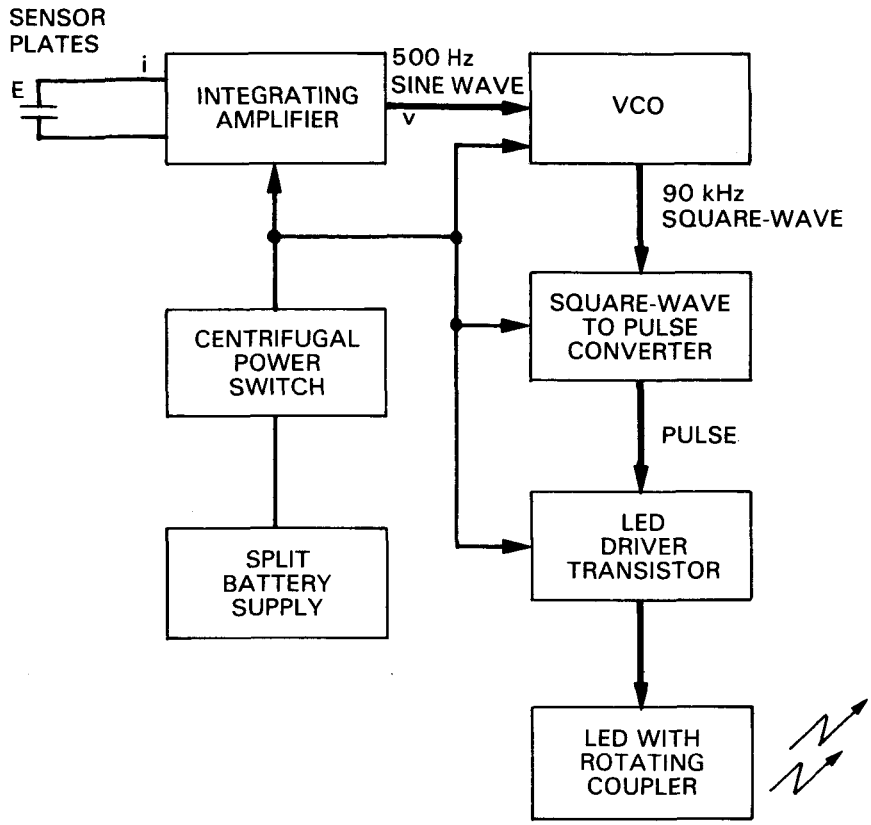

Figure 1-4. Block diagram of the probe electronics.

The CD4046 contains two different phase comparators along with the probe VCO. The output of the VCO is connected to both inputs of the "type 2" phase comparator. The signals arriving at the comparator will be slightly out of phase because one of the inputs (normally used for the signal input) has an amplifier that inserts a small delay (about 100 ns). As a result, an auxiliary output of the phase comparator (normally used as a lock indicator) produces a pulse of approximately 250 ns. This pulse is used to drive the LED. Since the VCO has a center frequency of 90 kHz, this represents a reduction in the duty-cycle from 50% to about 2%.

The negative-going pulse is amplified by an PNP transistor and drives the LED with 10 mA pulses. The current is enough to provide a comfortable power margin in the link, while still being considerably below the LED rating. The LED, mounted to the spindle, couples its infrared light pulses into a short piece of 400-μm optical fiber mounted on the axis of the shaft, then across a 0.010 inch (0.25 mm) air gap into a fixed, non-rotating fiber. The fixed fiber, also a 400-μm type, leads through the fiberglass support pole to the receiver. The measured optical power margin of this data fiber arrangement is 13 dB.

NOTE: NUMBERS IN PARENTHESIS ARE HYBRID PINOUTS

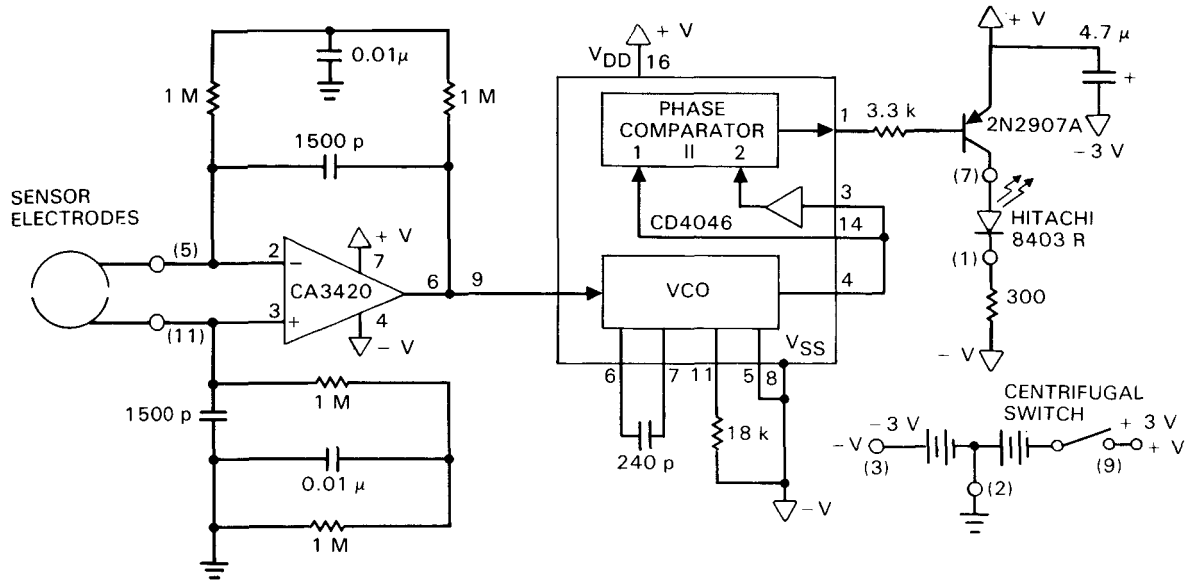

Figure 1-5. Diagram of the probe electronics

The power drain of the rotating circuitry is approximately 8 mW. The LED accounts for less than 20%, and the operational amplifier is responsible for about 40% of the total drain. Four silver oxide watch batteries power the probe for over four hours of continuous service. In intermittent use, battery life is observed to be many times longer. (Battery life could be extended by using a micro-power amplifier chip.)

1.2.2.2. Hybrid circuit design

The probe electronics was miniaturized into hybrid form by JPL's System Integration Section.

Figure 1-6, a labeled computer printout of the hybrid circuit layout, can be used to identify the components. The hybrid circuit is shown in the photograph, Figure 1-7. The two integrated circuit dice can be seen in opposite corners of the substrate. Eight chip resistors, six chip capacitors and one transistor are also shown. The circuit was laid out with the aid of a computer on a square substrate, 0.5 inches on a side, and fits within the pins of a TO-8 header.

Since the probe rotates at such high speed, balance is important. Care was taken to balance the component layout on the hybrid substrate. The heaviest component, a 4.7 μF tantalum filter capacitor, was mounted on-axis in the center of the substrate. The VCO timing capacitor was "piggy-backed" on top of the filter capacitor. Interconnections were thermobonded using the shortest wires possible to minimize wire vibration and possible electronic noise caused by it. The components were carefully cemented to the substrate to make the circuit as robust as possible. A cover was bonded to the header using conductive epoxy to ensure good electrical contact for circuit shielding.

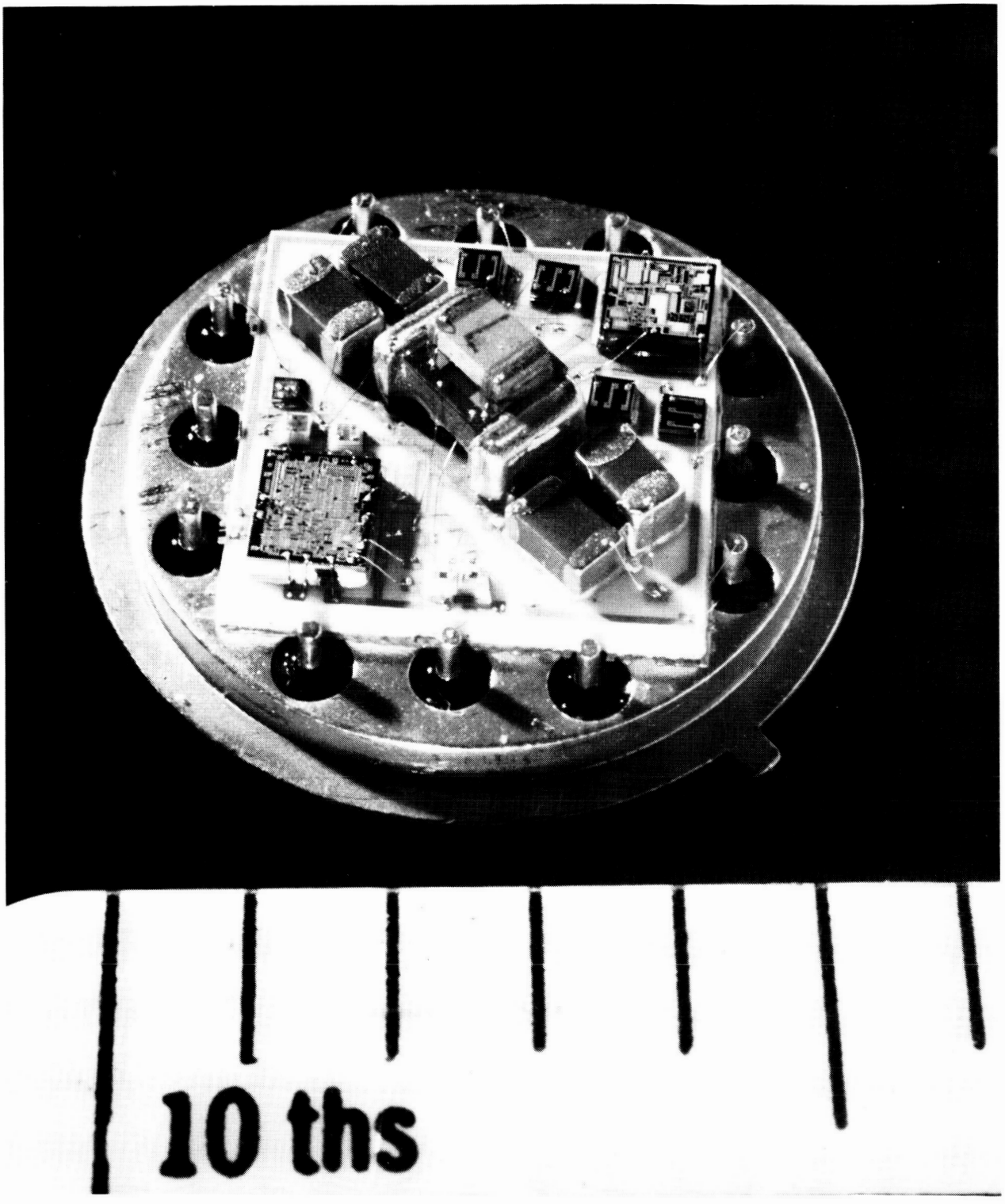

Figure 1-7. Photograph of hybrid circuit with cover removed

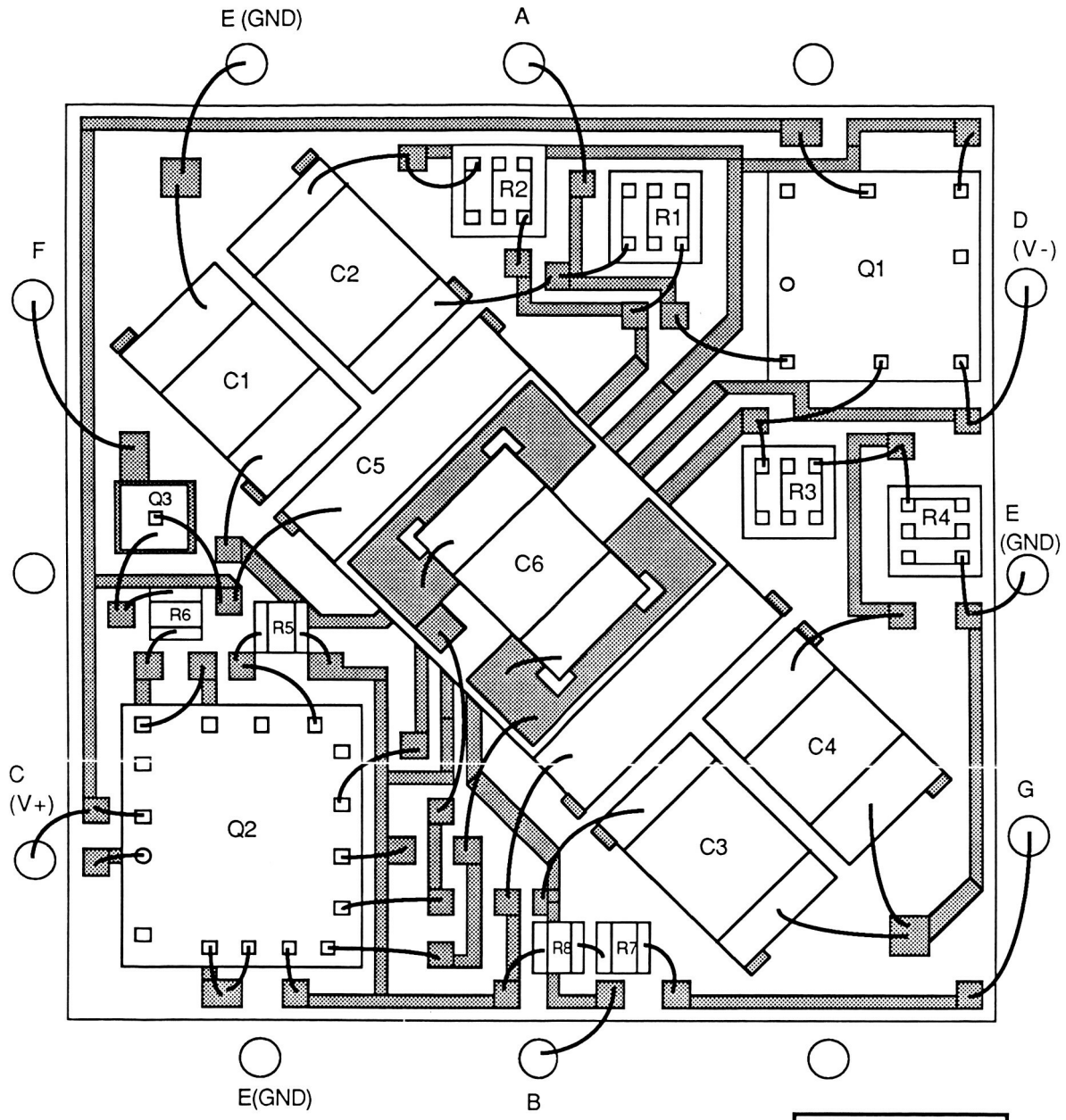

R1,R2,R3,R4 - 1MΩ
R5 - 18kΩ
R6 - 3.3kΩ
R7,R8 - 150Ω

C1,C4 - .01μf
C2,C3 - 1500pf
C5 - 4.7μf
C6 - 240pf

Q1 - CA3420E
Q2 - CD4046BE
Q3 - 2N2907A

PACKAGE TYPE:
T08 HEADER

ALL COMPONENTS
BONDED WITH ABELFILM
517
Q3,C6 WITH H20 E

Figure 1-6. Labeled printout of hybrid substrate layout

1.2.2.3. Position Reference System

The position reference system is used to generate information about the angular position of the probe. One pulse is produced each revolution of the shell, by means of an optical/electrical system, shown in Figure 1-8.

An infrared light emitting diode injects about 300 μW of optical energy into a directional coupler. The output is coupled into a 100 μm fiber optic cable, which passes, along with the data fiber and the air hose, down the middle of the pole used to hold the probe. Inside the probe, this fiber is attached to a ferrule which points at the edge of the shell.

Most of the edge of the shell is painted with a dark paint, but a small spot is made reflective, and returns some of the incident energy into the fiber when it is in front of the ferrule. In order to increase the amount of light reflected into the fiber, the ferrule includes a ball lens, which collimates the output beam. (In spite of the collimator, losses in the reflection are still large.)

The reflected energy is fed back to the directional coupler, which splits the power between the LED (where it is wasted) and a PIN diode. About 2-3 μW of optical energy is present at the PIN diode, which produces an electrical pulse corresponding to each optical pulse.

The current pulse from the PIN diode is amplified and converted to a voltage by a transimpedance amplifier, and sharp-edged pulses are produced by a voltage comparator. These pulses are used by the receiver as a synchronous reference for the coherent detector and for the tachometer.

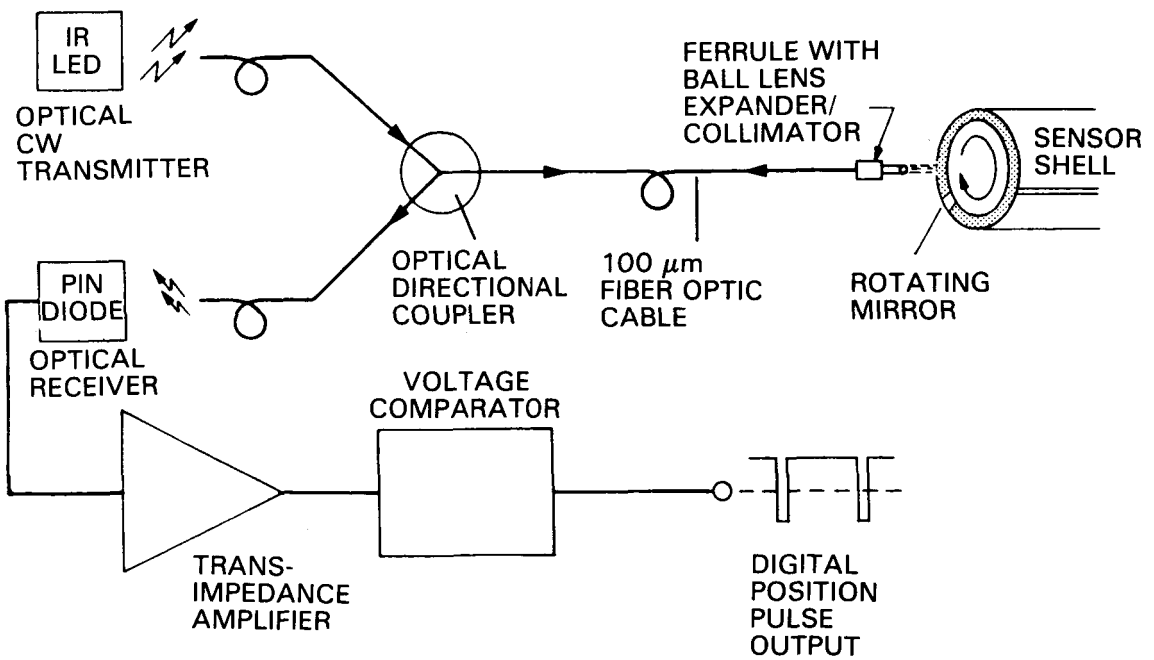

Figure 1-8. Position reference system

1.2.3. Receiver design

A block diagram of the synchronous detector used in the DOE field meter is shown in Figure 1-9. For clarity, the design is divided into four parts: the data channel, the reference channel, the measurement section and the power supply. Each will be described in turn.

1.2.3.1. Data Channel

The circuit of the data channel is shown in Figure 1-10. The frequency modulated optical carrier, at a center frequency of 90 kHz, is received by diode D1, a Hewlett-Packard HFBR 2202. The current generated by the incoming photons is coupled directly to an amplifier inside the receiver assembly, which furnishes logic-level pulses to the remainder of the circuit. Since the optical system is driven by a light emitting diode in the probe, the received light level is quite high (78 μW pk) so that the associated circuitry can be rather straightforward.

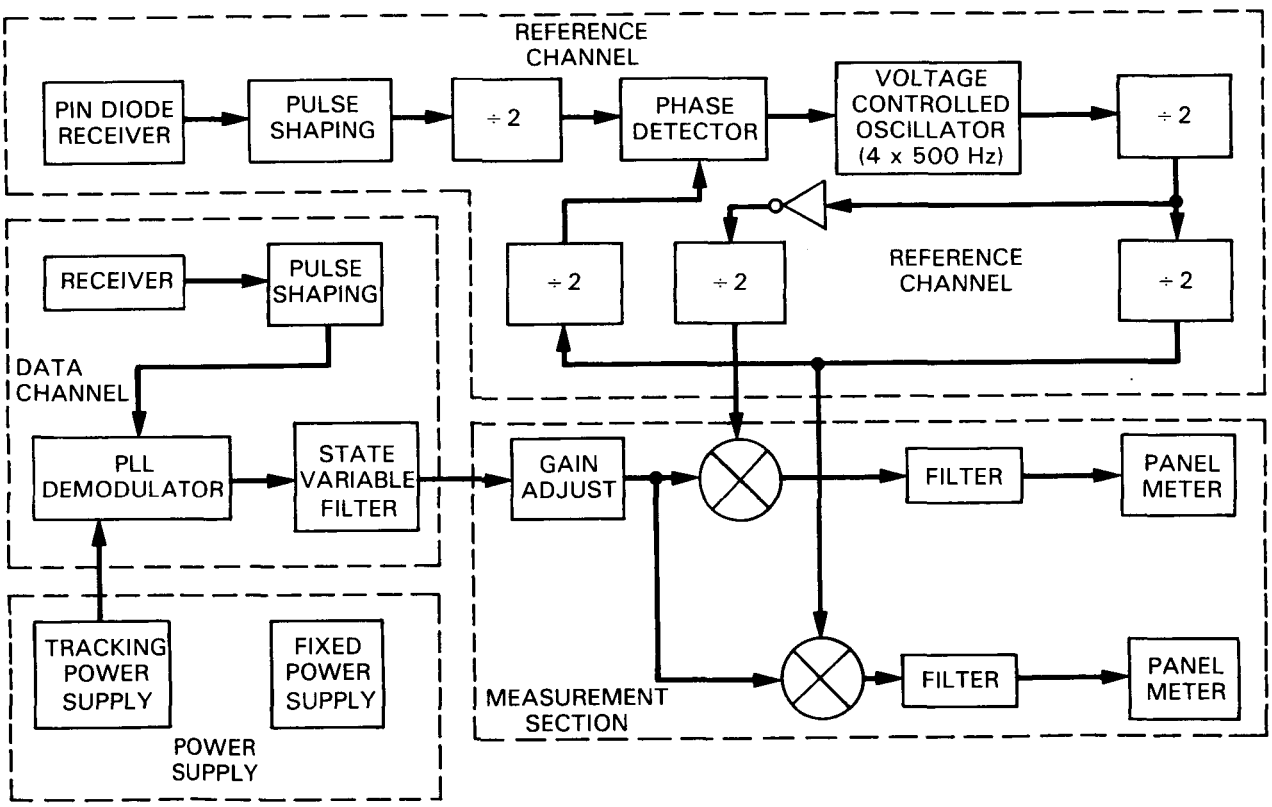

Figure 1-9. Receiver block diagram

The narrow pulses from the receiver are level-shifted by transistor Q1 to CMOS voltages. (The receiver diode is not rated for operation at the 10 volts used in our CMOS receiver.) The pulses are then inverted by U8, and applied to the phase locked loop detector, U6, a CD4046. In order to track the probe VCO as

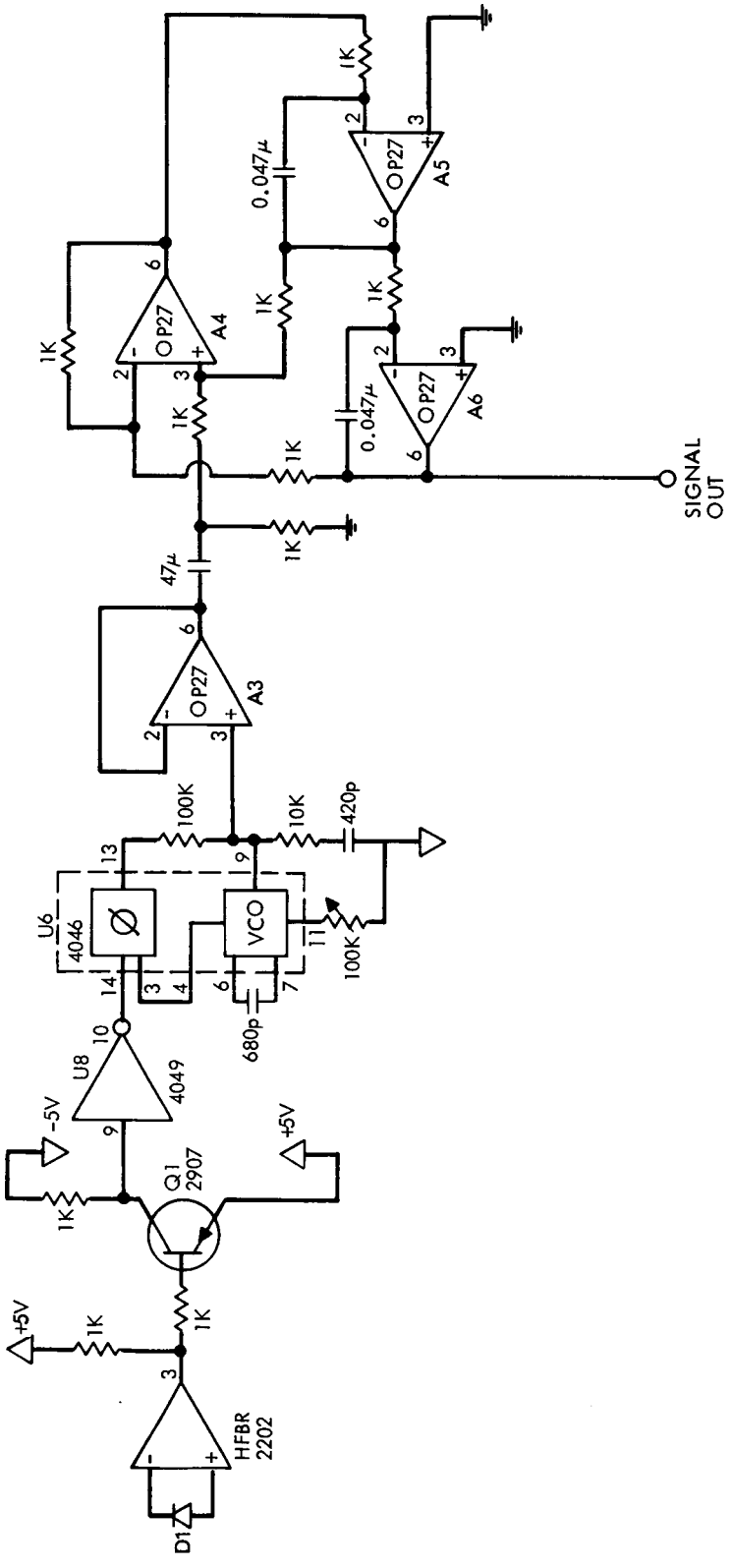

Figure 1-10. The receiver data channel

closely as possible, the PLL is operated from reduced voltage power regulators to match the operating conditions of the VCO in the probe. The output of this stage represents the instantaneous modulation applied by the probe to the carrier. The output signal is buffered by amplifier A3, which is a unity gain non-inverting amplifier. The maximum signal level at the output is about a volt, limited largely by the low voltage of the power supply.

Noise in the demodulated signal is reduced slightly by the filtering provided by the PLL loop filter. However, since synchronous detection is used to measure the amplitude of the signal, the PLL filtering can be optimized for the operation of the loop, rather than to provide a noise-free signal.

One further stage of filtering is provided by a state-variable filter. The main purpose of this filter is to reduce noise spikes, to ensure that the instantaneous value of the signal and the noise applied to the detector stage does not exceed its linear range. In addition, a "cleaner" waveform is obtained at the various test points in the circuit.

1.2.3.2. Reference channel

The reference channel is used to generate switching signals that are synchronous with the rotation of the probe, and are in phase quadrature. These signals are used in conjunction with the data signal to obtain the two orthogonal components of the field.

An optical pulse is reflected from the rotating shell of the probe once each revolution. This pulse is used to furnish information on the orientation of the field with respect to the probe. Switching signals for the synchronous detector are derived from this pulse train. The circuit of the reference channel is shown in Figure 1-11.

Optical energy is generated by a laser diode D1, an HP HFBR2208, and coupled into the optical fiber that illuminates the rotating shell by way of an optical directional coupler. Energy reflected by the shell is coupled to the receiving diode D2 by this coupler. The light energy at the receiving diode is lower than that in the corresponding part of the data channel because of losses in reflection, and two passes through the 3 dB coupler. Because of the low level of returned light, a somewhat different amplifier system (A1 and A2) is used.

The integrated circuit phase-locked loop contains two phase detectors. One is the conventional exclusive-OR type detector, which requires both inputs to be approximately square waves. The other is an edge-triggered phase detector, with tri-state output. (This detector is actually a frequency and phase detector, and can operate over a wide range of frequencies. The detector output can be used to show the relation between the reference and VCO frequencies even when the loop is not locked.) It is a property of the exclusive-OR phase detector that it has noise in its output at twice the input frequency. In order to furnish this detector with a square-wave signal, the reference channel input pulses would have to be squared, which can be done most easily by halving the input frequency. This approach leaves noise at the data channel input frequency (500 Hz) in the phase detector output. Since this would be a significant source of error, another approach was used. The edge-

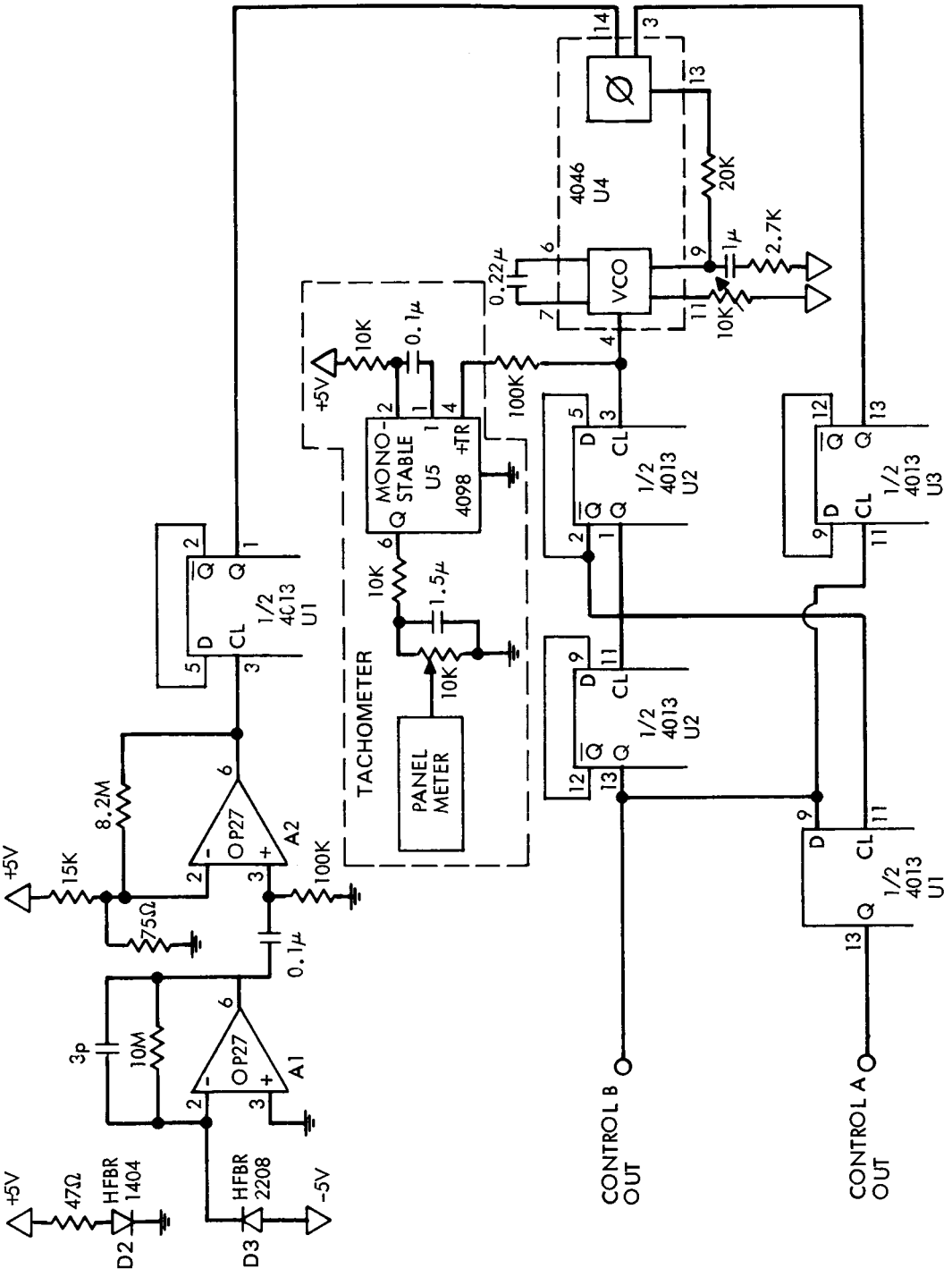

Figure 1-11. Receiver reference channel

triggered phase detector produces only low-frequency noise in its output. This noise is not expected to cause errors in the measurement.

The CD4013 flip-flops U2 and U3 divide the frequency of the VCO U4 by eight, and close the phase locked loop. The Q and $\bar{Q}$ outputs of the first divider after the VCO (part of U2) are at twice the synchronous frequency, and 180° out of phase. The Q outputs from the dividers that these signals feed (parts of U1 and U2) are at synchronous frequency, and in phase quadrature. The loop is closed at half the synchronous frequency by the edge-triggered phase detector in U4.

1.2.3.3. Measurement system

The measurement system is shown in Figure 1-12. The system consists of a gain adjustment potentiometer, ac amplifier A7, synchronous switch U7 and output amplifiers A8 and A9.

The signal from the FM demodulator is amplified by A7, and applied to the synchronous switch U7. Note that the output of the amplifier is ac coupled to the switch. This reduces the accumulated effects of amplifier offset and oscillator frequency drift. Since the waveform of the current representing the field is symmetrical, its average value is zero. The ac coupling to the switch removes any dc offset, and restores the zero average value.

A potentiometer is used for calibration. The gain of the amplifier A7 is switchable. The combination of the potentiometer and A7 gives a minimum gain of approximately unity, so that with the maximum signal from the PLL demodulator, about one volt is applied to the synchronous switch.

The gain of the system is set by the range switch, in steps of 20 dB (factors of 10). As the available signal from the probe decreases from its maximum value, the gain of the amplifier A7 can be increased, to a maximum of 40 dB. The gain of this part of the circuit is kept fairly low to avoid overload of the switch, and to help ensure stability.

The signal applied to the switch U7 is (if the system is linear) a sine-wave. Since the switching function is driven by a pair of quadrature signal of exactly one half-cycle of the synchronous frequency, the output of the switch is either zero (if the switch is "off") or part of the incoming sine-wave (if the switch is "on"). Thus:

$$E_o = E_i \cos(\omega t + \phi) \qquad 0 < \omega t < \pi \qquad (1\text{-}1)$$

$$E_o = 0 \qquad \pi < \omega t < 2\pi \qquad (1\text{-}2)$$

where ϕ is the phase angle between the signal and the switching function, E_i is the peak amplitude of the input signal and E_o is the output amplitude.

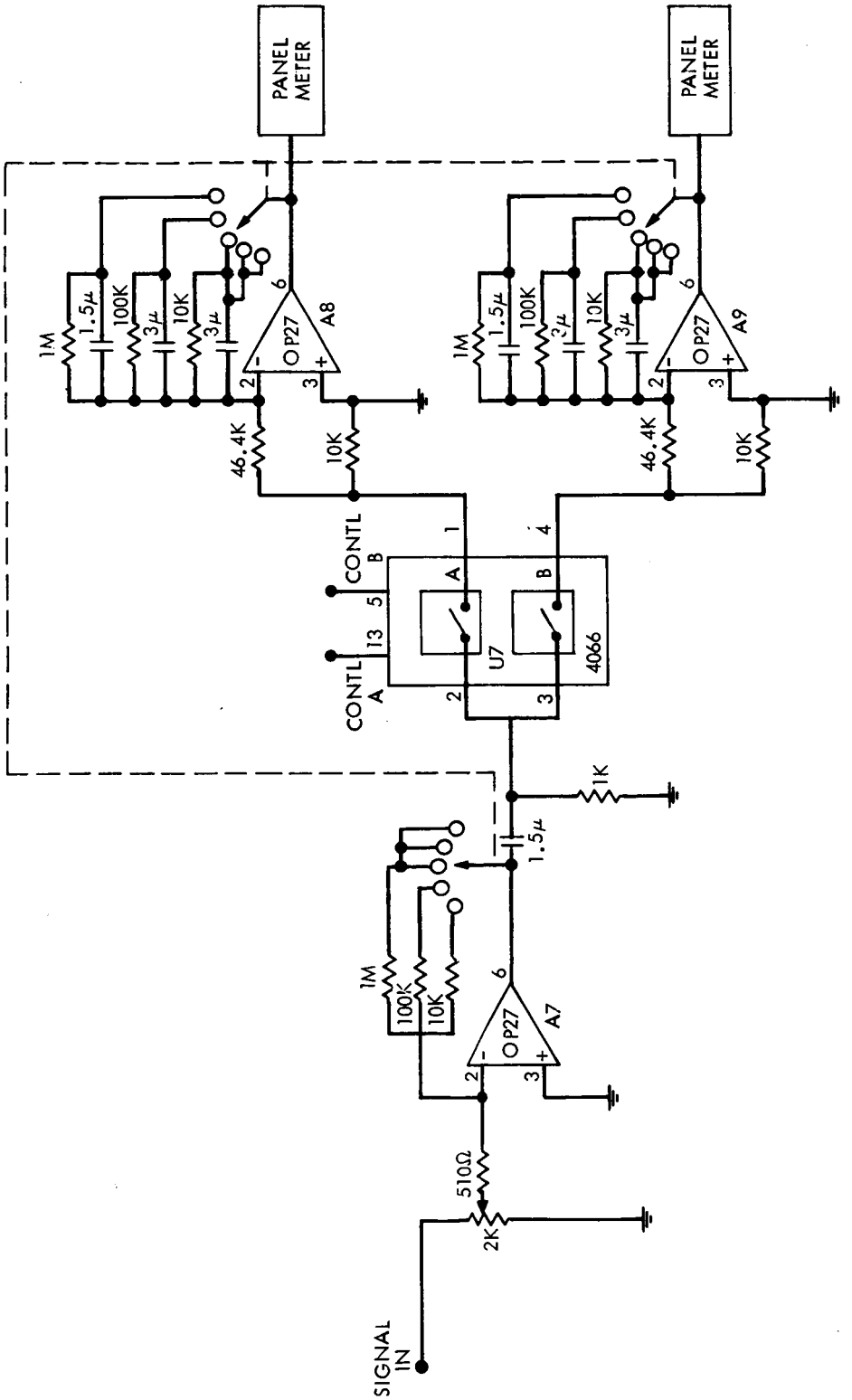

Figure 1-12. Measurement system

The amplifiers A8 and A9 "smooth" the signal detected by the switch, and present the result to the panel meters used for output display. Mathematically:

$$E_d = \frac{E_i}{2\pi} \int_0^{\pi} \cos(\omega t + \phi)\, d\omega t \tag{1-3}$$

$$= -\frac{E_i}{2\pi} \sin \phi \tag{1-4}$$

where E_d is the amplitude of the displayed signal. Since the panel meters require only 200 mV for full-scale reading, the minimum gain of the output amplifiers is about 0.2, or about −14 dB.

During operation the range would be changed to accommodate reductions in the incoming signal from a maximum of about a volt. The output amplifiers operate at minimum gain until the first stage, A7, reaches maximum gain. Since A7 is ac coupled to the synchronous switch, changing the gain does not affect the offset. Further, the switch is guaranteed to have the maximum signal possible, minimizing the effect of coupling from the switching signal. However, since A7 is a wideband stage, it was not thought prudent to allow 60 dB gain, which would have been the next step, as there might have been stability problems. Consequently, when a further increase in gain is called for, the post-detection amplifiers A8 and A9 are used. The maximum gain of these stages is about 20 times, or 26 dB. This relatively modest gain increase is unlikely to cause stability problems because the gain of the amplifiers rolls off above a few Hertz. In addition, problems of amplifier offset are minimized by having the dc stages operate at low gain. Use of an offset-correcting meter (such as the Ferranti ZN451) would simplify the design in future implementations.

Because digital display devices operate (usually) with full-scale readings of 199..., the field meter ranges are (full scale) 200 V/m, 2000 V/m, 20 000 V/m, 200 000 V/m and 2 MV/m. (Or, in the more usual units, 200 V/m, 2 kV/m, 20 kV/m, 2 kV/cm and 20 kV/cm.) Air insulation breaks down at about 30 kV/cm. The DOE field meter was not really designed to operate in such a high field; it is unlikely that the operator of any dc line would permit personnel to get sufficiently close to a line to measure a field even approaching this value. Consequently, the maximum field that can be measured by the DOE meter, about 5 kV/cm, is quite adequate.

Apart from the maximum readable field, which causes the probe electronics to overload, and which occurs part way into the highest scale of the meter, the panel meters are arranged to be the first part of the system to overload as the signal is increased. The front panel display indicates this condition (only the leading ½ digit is displayed) as an indication that the range of the instrument should be changed.

By these means, the gain of the measurement system is adjustable in steps of 20 dB over a range of 80 dB. This permits measurements to be made over a dynamic range of about 100 dB using 3½ digit panel meters.

1.2.3.4. Power Supply

The field meter is designed for portable operation, and uses a battery power supply. In the prototype instrument, series regulators were used to stabilize the electronics voltage. Separate supplies were used for the data channel, to minimize the errors due to coupling of synchronous noise. The circuit of the power supply is shown in Figure 1-13.

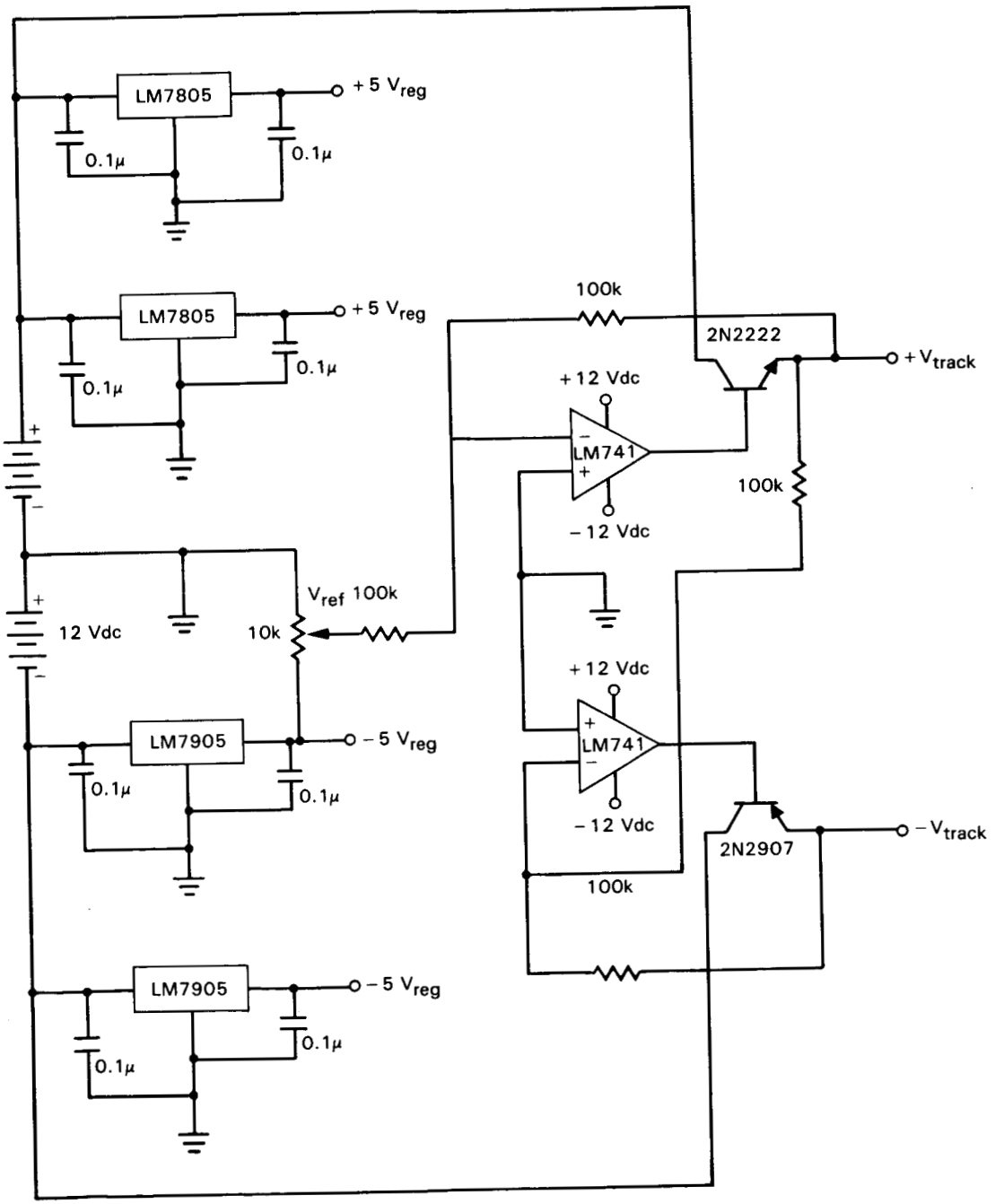

Figure 1-13. Receiver power supply

An additional tracking power supply was built for the data PLL, so that the supply voltage for this stage could be adjusted independently of the remainder of the system, in order to linearize the data link. (See Section 1.3.1.2 and Appendix C.)

1.3. Test results

The dc field meter was designed to be used in the environment of a power transmission line. Before we tested the meter under these conditions, it was calibrated and tested under controlled laboratory conditions, both at the Jet Propulsion Laboratory and the National Bureau of Standards. These tests, and the subsequent tests of the meter under realistic power line conditions, are described in this section.

1.3.1. Tests at JPL

1.3.1.1. Mechanical performance

The sensor probe provides very quiet and smooth operation at speeds up to approximately 40 000 rpm. Once the sensor is spun up to working speed (normally 25 000 rpm), its speed is stable and there is little need for adjustment in air flow. The turbine needs oiling once a day. This is accomplished by spraying a small quantity of dental drill oil into the air hose at the receiver end. At 25 000 rpm the probe can run approximately six hours on a full K-type nitrogen bottle. The prototype device has shown itself to be reliable: the sensor turbine had to be serviced only once (after about 30 hours of operation) to remove some foreign material (which presumably entered by way of the air hose).

The probe requires a balancing after servicing or when the batteries are changed. Sets of batteries with closely matching weights could possibly eliminate the need for balancing entirely. Balancing the spindle, changing the batteries, or swapping the spindle assembly completely can be done in under five minutes, using standard tools such as Allen keys and screwdrivers.

1.3.1.2. Data link

For purposes of understanding and increasing the linearity of the data link, the voltage to frequency and the frequency to voltage conversions were tested individually, outside of the system. The variables whose influence was examined are the particular IC itself, the timing components which determine the center frequency, the center frequency, the low-pass filter components (f/v only), and the power supply voltage.

First, the effect of different integrated circuits of the same type was examined. It was found that for different ICs (for either conversion), different transfer function curves result, as shown in Figure 1-14.

Both the center frequency and the conversion slope appear to depend on the device used. The fact that the two circuits produced different frequency to voltage curves means that, in general, the voltage to frequency curve of the probe VCO can be expected to differ from the frequency to voltage curve of the

receiver. The use of different components is unavoidable. However, when the same IC was used for both conversions, the slopes of the frequency to voltage and voltage curves are complementary. This is shown in Figure 1-15.

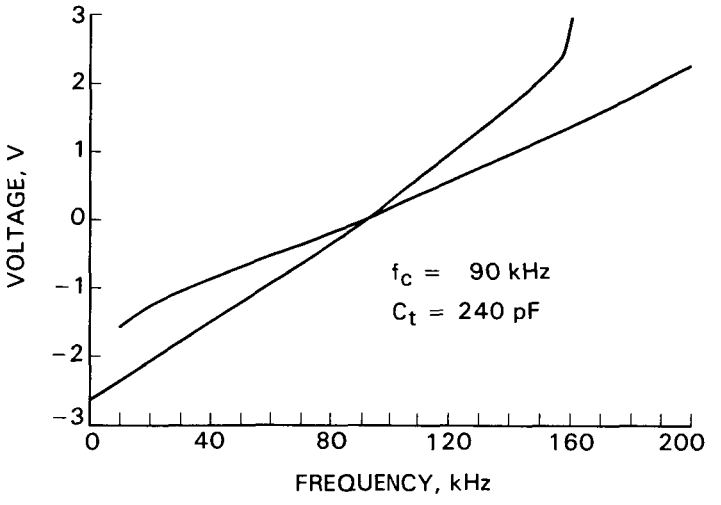

Figure 1-14. Frequency to voltage curves for two different integrated circuits

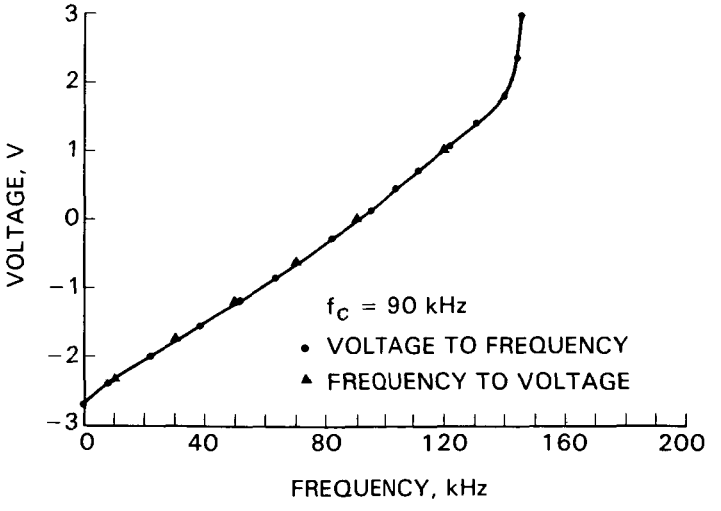

Figure 1-15. Frequency to voltage and voltage to frequency curves for the same integrated circuit

It appears that each individual IC has a characteristic slope. In order to increase the linearity of the system, either the components need to be matched, or some 'tailoring' of the slopes must be done.

The timing components chosen had little or no effect on the slope or the capture range over the frequencies tested. This can be seen in Figure 1-16, which compares two values of timing capacitance, C_t.

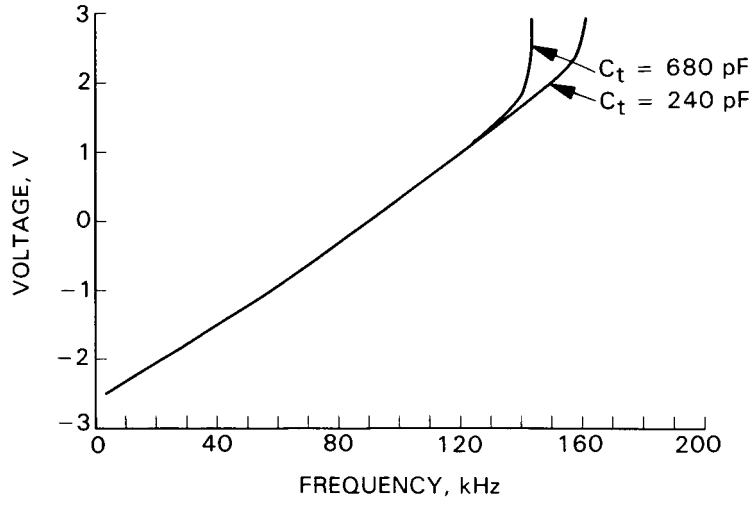

Figure 1-16. Effect of timing component values on conversion characteristics

As the center frequency, f_c, was increased, the slope of the curve decreased. This change appears to be a linear relationship. Since, in normal operation, both conversions must be at the same frequency, altering either center frequency cannot be used to match the slopes of the curves. Figure 1-17 demonstrates this.

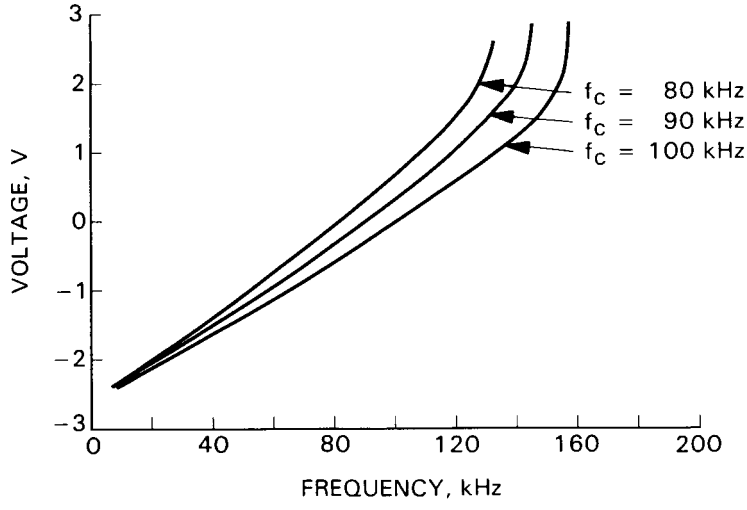

Figure 1-17. Change in slope with center frequency

The effect of the filter components is quite complex. The testing done here was all static, and in actual use the filter affects the dynamics (capture

range and tracking ability) of the PLL. No effect on the static conversion characteristics was observed as loop filter components were charged. Increasing the voltage of the power supply has the effect of increasing the slope of the voltage/frequency curve. Normalized data are plotted in Figure 1-18.

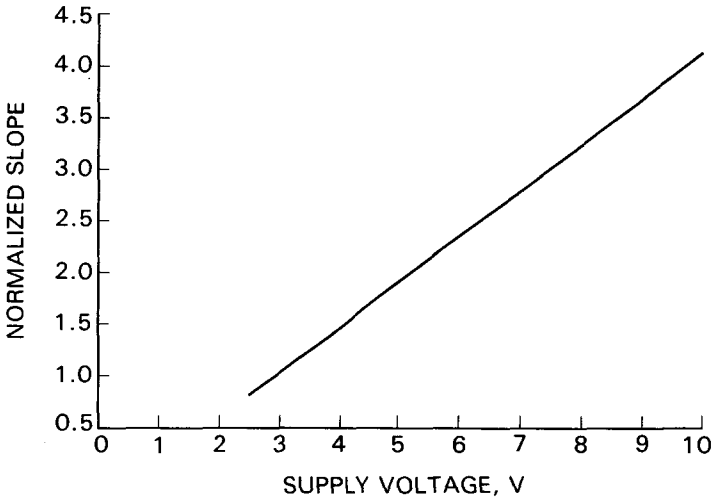

Figure 1-18. Effect of voltage on conversion slope

It appears that voltage trimming could be used for matching the characteristics of the probe voltage to frequency converter to the receiver frequency to voltage converter. The receiver PLL stage can readily be operated from a separate (tracking) power supply which can be adjusted to match the receiver to the probe characteristics.

1.3.1.3. Effect of pole resistance

It was observed that when the test cage was energized with asymmetrical voltages, the calibration of the meter was not constant. Even though the cage generated a uniform field, as verified by the field meter with the probe potential at zero, the meter indicated a higher field near the high voltage electrode. The problem was eventually traced to leakage current down the pole supporting the probe. This current essentially grounded the probe, so that there was field intensification at the location of the measurement.

The resistance of the offending pole was independently measured (at 30 kV/m) and found to be in the range 3 to 10 $\times$ 10^{10} Ω/m. Thus at 30 kV, this pole could drain off nearly 0.1 μA. Although surface cleaning made a small improvement, the leakage was essentially a volume effect. The leaky pole was then replaced with a fiberglass (type GEE fiberglass, a light green material) pole. The resistance of this material was at the limit of our measurement instruments, $>10^{16}$ Ω/m. The fiber cables and air hose were also tested and found to have a resistance of $>10^{16}$ Ω/m, bringing the potential leakage current under the same conditions to $\leq 10^{-12}$ A.

The leakage phenomenon was further illustrated by observing the change in the sensor output following energization of the field cage. The results are shown in Figure 1-19 for the original, leaky pole, and in Figure 1-20 for the GEE fiberglass pole. No ion current was present. The observed relaxation curve represents the charging of the probe-ground capacitance by charge leakage, which includes both pole leakage current and ambient ionization of the air. The time constant for the leaky pole was 20 sec, and for the GEE pole, 13 minutes. The sensor was located 9 cm from the charged screen of the cage. The screen spacing was 1 m.

It can be seen that under these conditions, namely with the sensor near the charged conductor, supported from the ground, and with no space charge present, neither result would be very satisfactory. Measurements might be possible with the good pole, if great care was taken to take readings quickly and then discharge the probe, but would not be possible with the leaky pole.

The addition of a small radioactive source of the type used in an antistatic camera lens brush was found to be an effective means of coupling the probe to the local space potential. The polonium-α source was attached to the base of the sensor adjacent to the rotating electrodes.

The amount of radioactivity used involves a compromise between providing an adequate source of ions to charge the sensor to equilibrium, and creating an ion cloud so dense that it perturbs the field to be measured. Unshielded, the polonium-α source generates enough ions to measurably decrease the field seen by the probe. With the source well shielded, the leakage problem returns. To be useful, the ion production must be enough to supply the pole leakage current without changing the local field. It appears that considerable margin is available to meet these conditions.

The addition of the radioactive source resulted in constant readings after about 1 second, the instrumentation time constant. This means that the probe was remaining at space potential, in spite of the slight leakage of the pole.

The electric field data shown in Figure 1-21 were obtained with a source on the probe. The intensity of our source was estimated to be 10 μCuries. A simple calculation of the total number of ion pairs per second produced in air by a polonium-α source indicates that 0.01 to 0.1 μCi would have been adequate to drain off the expected leakage current.

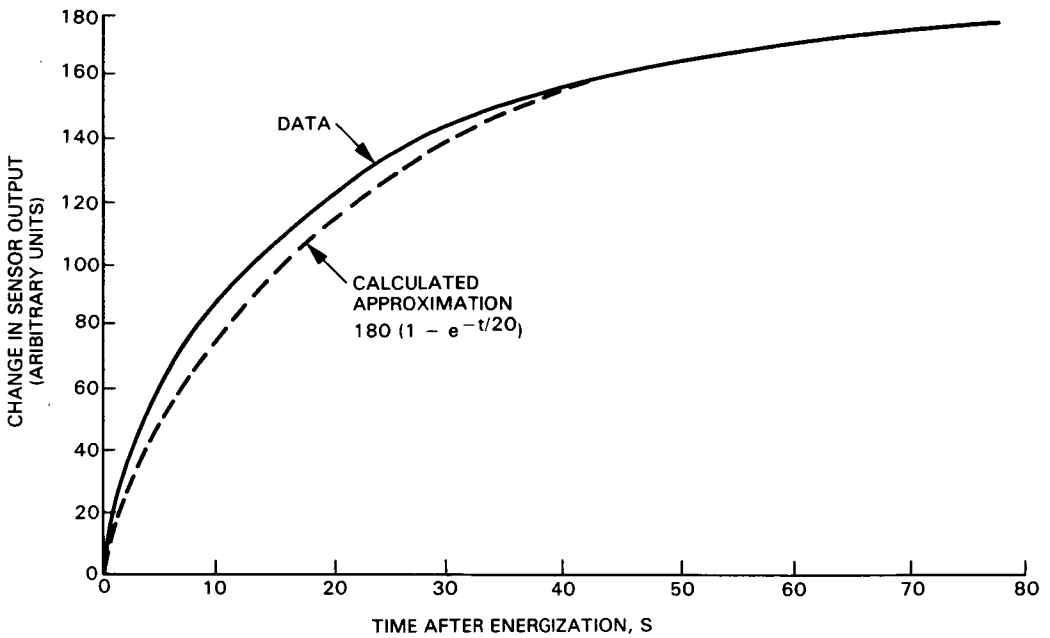

Figure 1-19. Cage energization transient, leaky pole

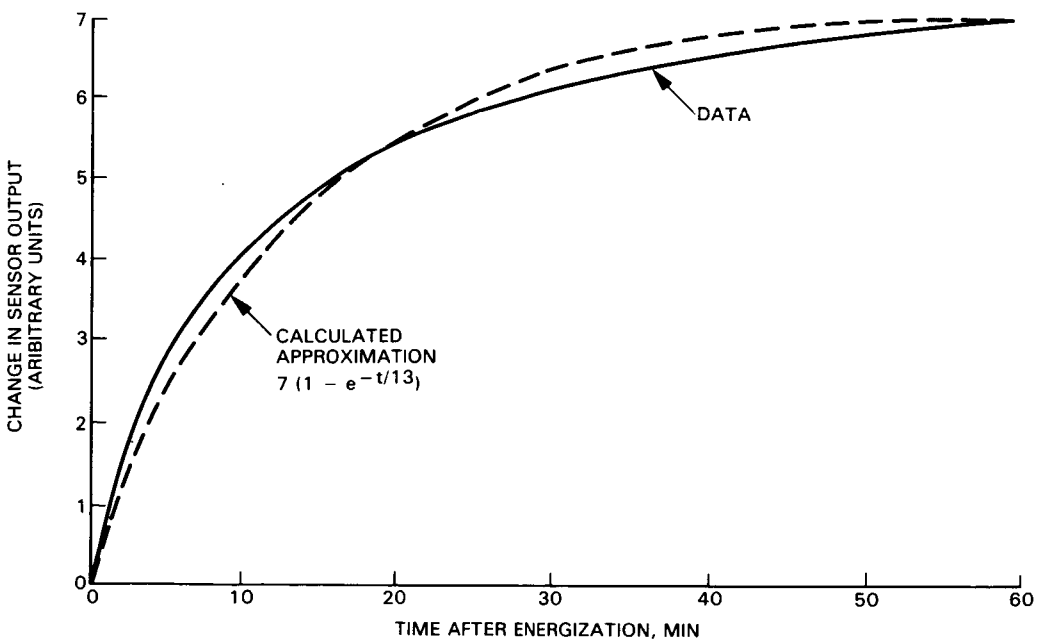

Figure 1-20. Cage energization transient, fiberglass pole

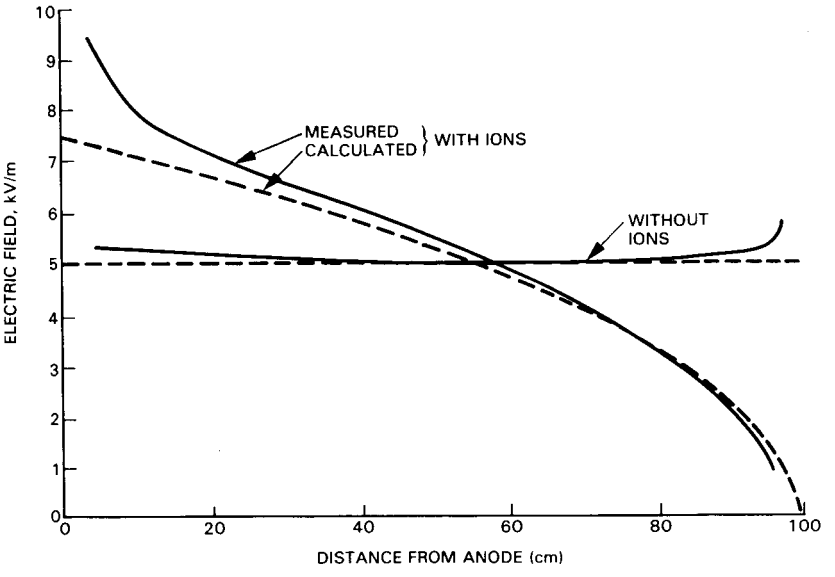

Figure 1-21. Electric Field Profile of Test Cage

The second curve in the figure was taken with a space-charge limited ion source in operation. The observed voltage versus position closely approximates the space charge limited values calculated for a planar diode in Appendix B.

1.3.1.4. Calibration at JPL

Sensor output was measured as a function of field in the JPL field cage before leaving for NBS and again after returning. The applied field was taken as the voltage applied to the cage divided by the plate spacing. The sensor was centered in the cage in all three coordinates. Calculations made by Takuma, Kawamoto and Sunaga (1985) indicate that corrections needed to account for fringing are negligible. Data were taken over a mid-range of field intensity, from a few tens of V/m to 18 kV/m. No attempt was made to reach the dynamic range limits of the device. The results are shown in Figure 1-22. Rather than showing the linearity curve directly, which would have been uninteresting, the instrument scale factor is plotted as a function of applied field. Scale factor is defined as sensor output voltage divided by applied field and is plotted in such a way that variations are easily visible.

It should be noted that large digitization errors were present at the time. An error in the gain distribution in the receiver meant that the full 3 1/2 digits of the display were not usable. This problem was later remedied. The magnitude of the digitization uncertainty is given by the error bars in the figure. The extremities of the bars represent the effect of a change in the last digit of the display.

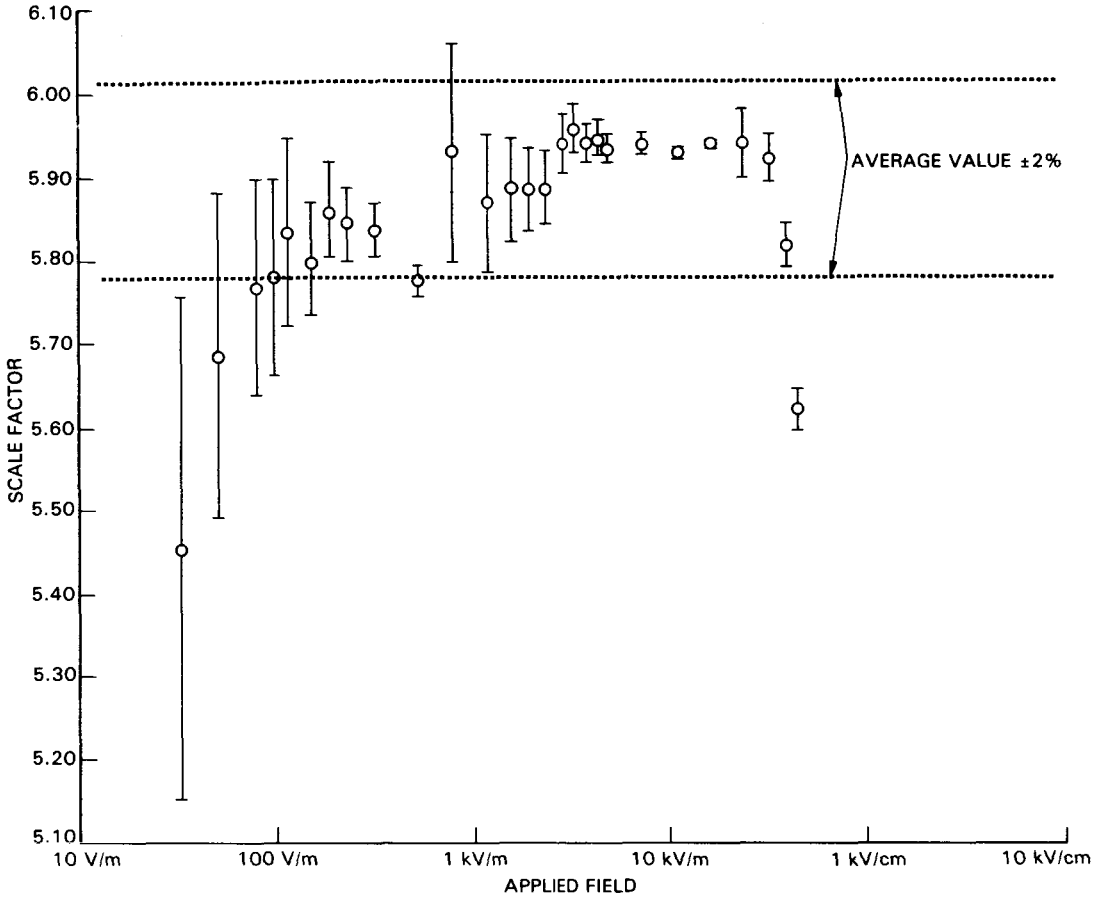

Figure 1-22. Scale factor of field meter as a function of applied field

There is an indication of droop below 100 V/m, reaching an extreme of about 7% at 30 V/m, the cause of which remains undetermined. However, none of the comparisons at NBS were made at these low field intensities. Averages of all JPL data above 3 kV/m both before and after the NBS visit (during which only fields between 5 and 15 kV/m were used) yielded a scale factor of 5.899. This value was used for the comparison at NBS. The difference between the calibration factor before and after the two cross-country trips was 1.4%

A similar set of data was also obtained in the JPL cage, using a different receiver. This receiver had a smaller dynamic range than the synchronous detector type, but internal gains were such that the digitization uncertainty was negligible. These data are given in Figure 1-23, and indicate that the standard deviation of one data point from a best-fit linear response under these laboratory conditions was 0.04%.

Both the envelope detecting and the coherent detecting type receivers were tested at NBS. As will be seen below, there was no significant difference

between the results from the two receiver types in these tests. For future use, the phase detector is a more sophisticated circuit with better noise rejection characteristics. It is capable of reading out both x and y components of field (but not z), but is somewhat more complex than the envelope detector. The latter is subject to error in a rapidly fluctuating field, and its low-field response is masked by a zero-level noise.

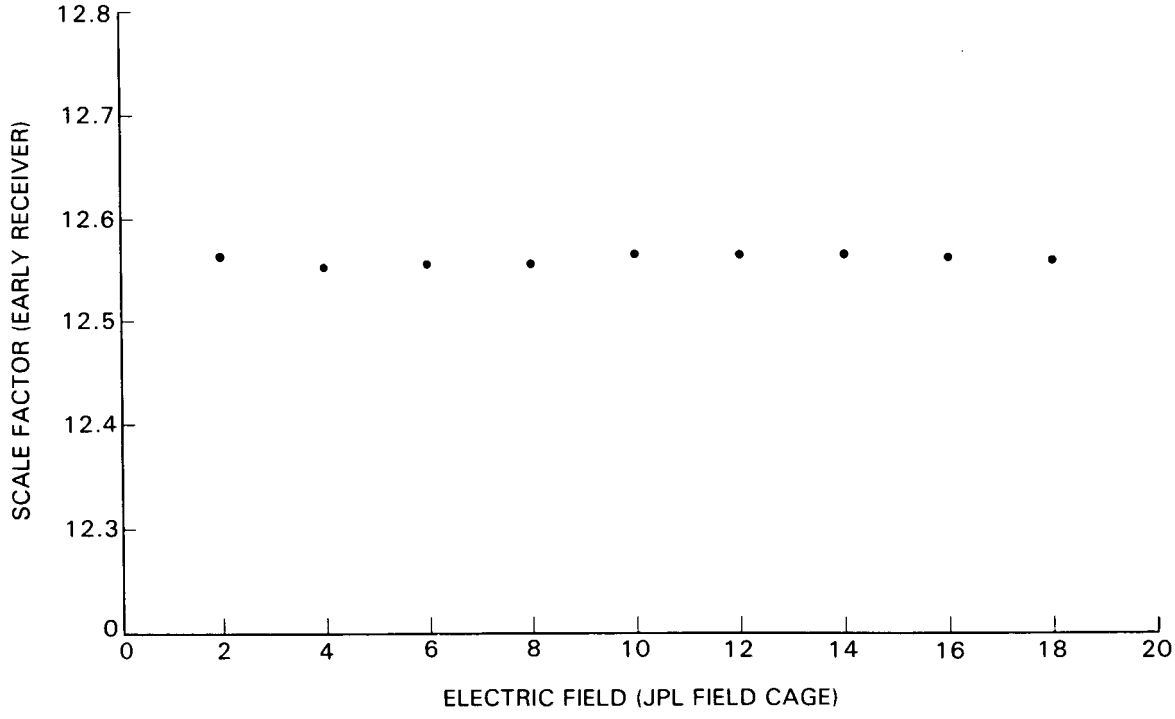

Figure 1-23. Scale factor of field meter, determined with a receiver without quantization problem

After the gain distribution in the synchronous detector receiver had been modified, and the scale factor adjusted so that the panel meters indicated the field values directly, the linearity of the meter was again evaluated. The results are shown in Figure 1-24.

In the data set shown in Figure 1-24, droop is again evident below 100 V/m. On other occasions, the linearity seemed to be good down to about 10 V/m. The reason for these uncertainties is not known, but it is possible that the explanation lies in the difficulty in obtaining an accurately known field of such low value. Stray charge, accumulated on the nylon safety rope around our cage, has been observed to produce a measurable field inside the cage. Charge on the pole holding the probe could also be the culprit.

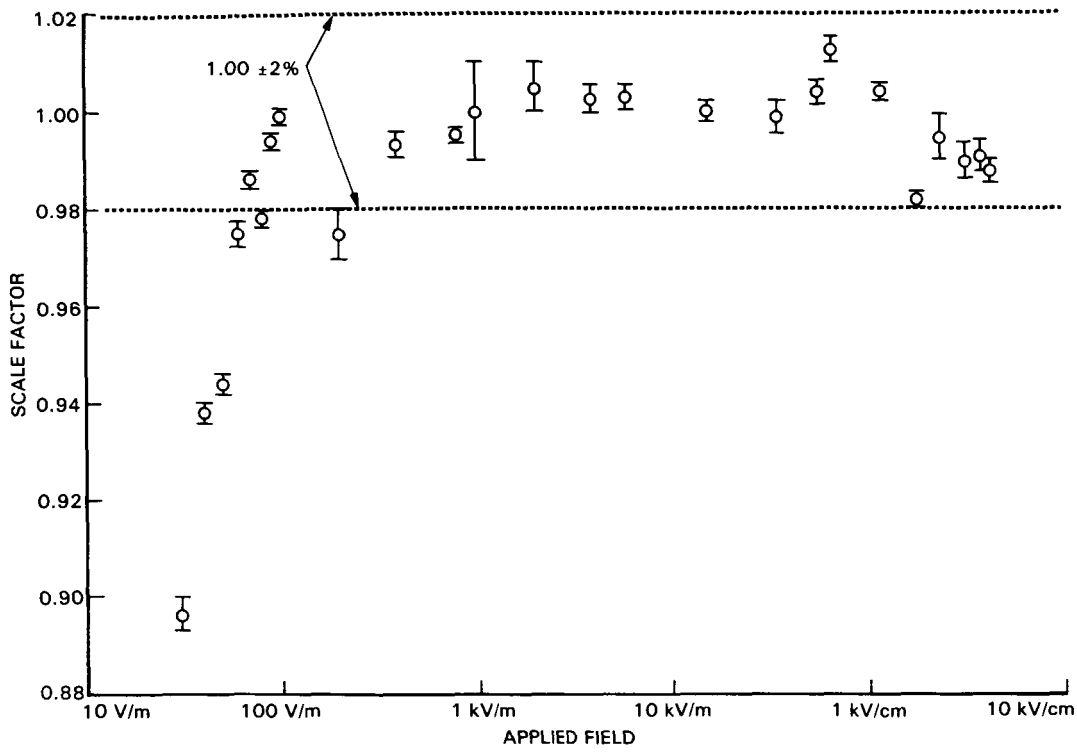

Figure 1-24. Final meter linearity

Above 100 V/m, the linearity of the probe seems to be good, perhaps in the order of ±2%. At the highest fields measured, more than 4 orders of magnitude above the smallest readings obtained, the field in the cage was intensified so much that flashover occured. It was not clear whether or not the flashover involved the probe; in any event the probe survived.

1.3.2. Tests at the National Bureau of Standards

1.3.2.1. Background

The dc field sensor was taken to the National Bureau of Standards in late September of 1986, and measurements were made with it in a test cage designed to produce a very uniform space charge environment. The purpose of these tests was to:

a) Compare the sensor calibration determined in the JPL field cage with an independently determined field in the NBS system.

b) Determine if the sensor could accurately measure field in the presence of a large space charge.

The NBS test cage is a facility that has been developed by Dr. Martin Misakian and his co-workers in order to evaluate various E-field measurement techniques in space charge environment. Prior to the testing of our field meter, testing at NBS had been confined to field mills mounted in the ground plane (bottom plate) of the test cage. The plates of the test cage were about 2 m square, with a separation of 17.08 cm. The top plate was a metal screen, with a corona wire and grid arrangement located above the screen to provide the ion current. Great care was taken in the construction of the cage to hold spacings uniform and to produce uniform current density so that a one-dimensional analysis would be accurate. Additional detail about the NBS system has been published by Misakian (1981).

Although the plate spacing was rather small, no significant error was expected from self charging because of the small size of the sensor (radius ~0.06 of the plate spacing) and the fact that the sensor was accurately located at the midpoint of the gap. The radioactive source described in Section 1.3.1.3 was placed on the sensor housing for all tests.

In contrast to the NBS cage, the plates of the JPL cage were spaced 1 m apart. There was no provision for generating a uniform space charge current density at the time these measurements were made, and none of the JPL calibration measurements were made with space charge present[1]. The instrumentation for charging the plates and for voltage measurement was different for the NBS and JPL cages.

The procedure used at NBS was to locate the dc sensor as accurately as possible midway between the plates, (about ± 1 mm). The voltage between the two plates and their spacing yielded the field with no space charge present. With space charge, additional measurements were made of the field at the center of the lower plate using a commercial field mill, and the current density was measured at the bottom plate. The field at the location of our sensor could then be calculated from the measured data.

1.3.2.2. Test results at NBS

The sensor, using the calibration obtained at JPL, was used to measure the field at the center of the NBS cage, and results were compared to the field values calculated independently from NBS measurements using the procedure outlined above. Observations were made at three values of electric field, between about 5 kV/m and 15 kV/m. For each field value, three space-charge current densities were set up, one with saturated current density, one at an intermediate value, and one with no current. The results are summarized in Table 2. Multiple measurements made under the same conditions (identical NBS readings) have been averaged.

Using the NBS field values as the reference, the difference between the JPL and NBS values are plotted in Figure 1-25 as a function of field. The NBS E-field values were estimated by Misakian to be accurate to 2-3%.

---

[1] Another test cage, based on the design of the NBS cage, was later built at JPL. It is described in Appendix A.

TABLE 2. SUMMARY OF RESULTS AT NBS

Ion Current Density		NBS Electric Field Value	JPL Meter, Envelope Detector	JPL Meter, Synchronous Receiver
(descriptive)	($\mu A/m^2$)	(kV/m)	(kV/m)	(kV/m)
no current	0	5.89	5.93	5.98
no current	0	8.78	8.9	8.81
no current	0	14.37	14.6	14.58
no current	0	0	-	3.8×10^{-3}
intermediate	0.209	6.10	6.2	6.24
intermediate	0.102	5.94	6.05	6.09
intermediate	0.221	8.85	9.0	8.98
intermediate	0.630	14.50	14.9	14.92
saturated	0.304	6.67	6.6	6.45
saturated	0.303	6.64	6.5	6.39
saturated	0.668	9.72	9.6	9.49
saturated	1.77	15.7	15.5	15.6

1.3.2.3. Conclusions

The results of the comparisons at NBS, as summarized in Figure 1-25, indicate that the dc sensor is able to measure electric fields in a space charge environment within 2-3% under the range of conditions which we were able to explore. It is felt that if higher fields were used, similar results would be obtained, but that space charge effects may become more uncertain at very low fields.

These comparisons were done in such a way that errors caused by self-charge with the sensor being near a conducting surface are minimized. Our earlier papers, (Kirkham, Johnston, Lutes, Daud and Hyland, 1984; Johnston *et al.*, 1986) may be consulted for an estimate of these errors. We do not feel that any observable perturbation of the results resulted from this error source.

No significant difference was observed as a function of field intensity, nor was there a systematic difference between our two receiver circuits. However, there does seem to be a systematic effect due to current density. The JPL-NBS difference appears to be approximately 4% lower for saturated ion current than for intermediate or no current. The direction of the difference is for the JPL value to be low or the NBS value high at saturation current density. The cause of this difference is not yet understood.

We have measured a temperature dependence of the reading of 0.1%/°C. This result and the tests at NBS indicate that the inherent stability and accuracy of the sensor electronics are quite good, and will not degrade measurements made under most conditions in the field.

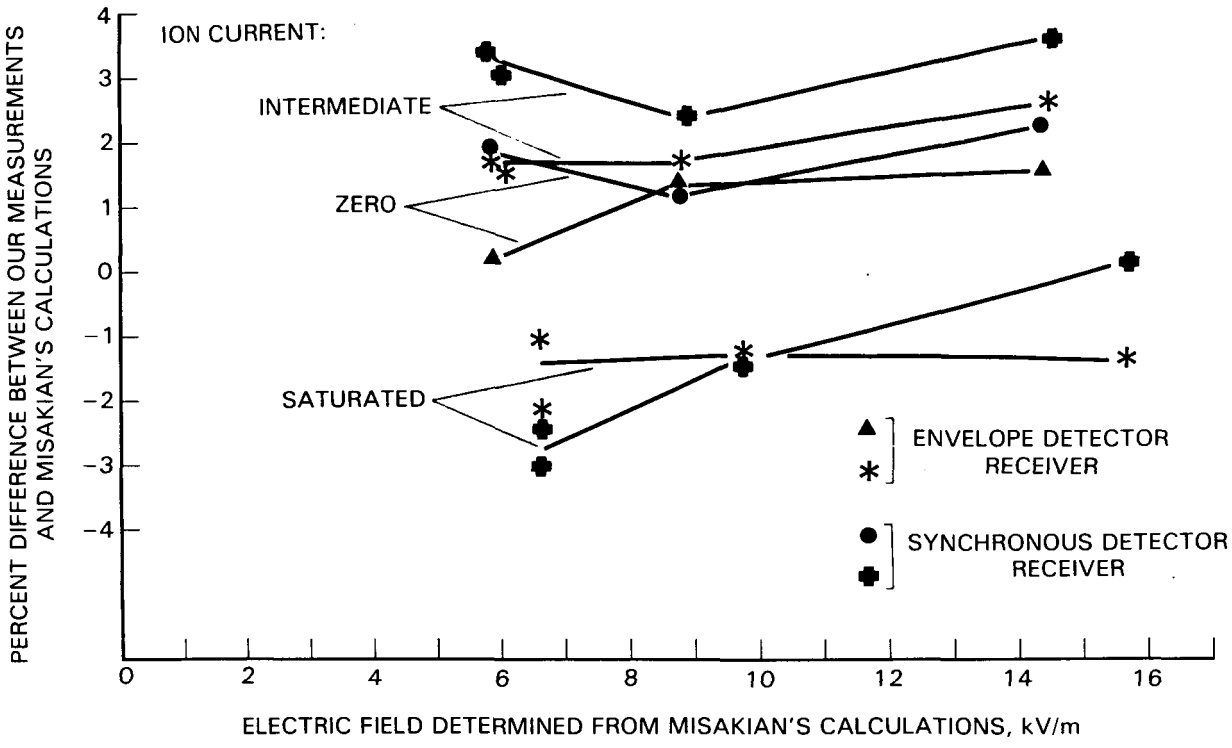

Figure 1-25. Difference between JPL and NBS field values

1.3.3. Measurements at HVTRF

In October 1986 the dc field meter was taken to the High Voltage Transmission Research Facility (HVTRF) in Pittsfield, Massachusetts, for a series of measurements under their HVdc test line. The purpose of this visit was to:

a) Demonstrate measurement of dc electric fields under an HVdc line at points significantly removed from the ground potential, in a realistic environment including space charge.

b) Compare data obtained with the JPL sensor to data from the HVTRF instrumentation.

The HVTRF is a test facility which is operated by General Electric for the Electric Power Research Institute (EPRI) for testing high voltage transmission components and techniques. It provides a short (~1km) section of transmission line under which our measurements were made. Two conductors were used for the dc tests, and could be energized singly or in combination. They were spaced 41 ft (12.5 m) apart and were approximately 51±2 ft (15.5 m) above the ground. A third conductor was located a similar distance west of these two but was not energized.

An instrumentation line was permanently installed on the ground surface along a line perpendicular to the conductors. It consisted of nine stations spaced out over a distance of 165 feet, each providing a measurement of electric field and

ion current density. Electric field was monitored by a vibrating plate type of field meter mounted in an inverted position (to minimize the ingress of rain and snow) over a large plate on the ground surface. Field measurements were referred to a portable transfer standard which was calibrated in a large on-site field cage. Ion current density was monitored by a conventional one meter square guarded plate. Further detail about the instrumentation has been reported in the literature (Comber and Johnson, 1982; Anderson and Doyle, 1975) and the facility has been the site of a workshop for comparison of various types of field mills (Comber, Kotter and McKnight, 1983).

During our tests, field, ion current density and wind data were logged by the HVTRF system at 1 minute intervals, and the data were made available to us.

1.3.3.1. Summary of HVTRF data

In order to provide an overview of the electric field environment when our measurements were being made, the raw data from the HVTRF instrumentation are presented here in the form of isometric three dimensional plots. Field intensity is shown vertically, with lateral position across the line and time as the two horizontal coordinates. The time intervals plotted overlap the times of our measurements. These data are shown in Figures 1-26 through 1-29. Concurrent wind data are shown alongside the time axis as an azimuthal vector plotted in the same perspective as the base of the field plot. Vector length is proportional to wind velocity, and the arrow head points in the direction of air flow.

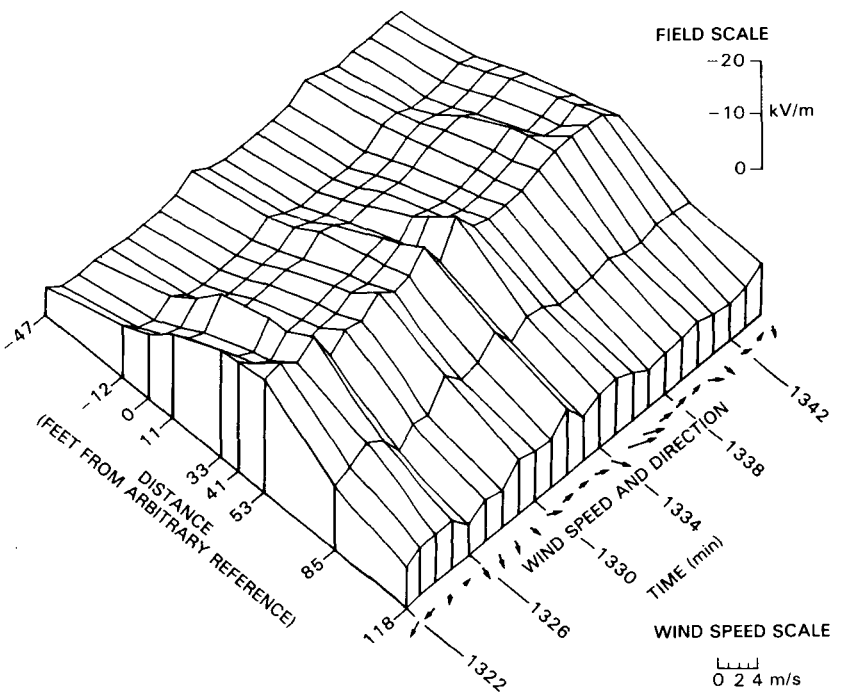

Figure 1-26. HVTRF data, 10-20-86, 1322-1344 hrs e.d.t., Line monopolar

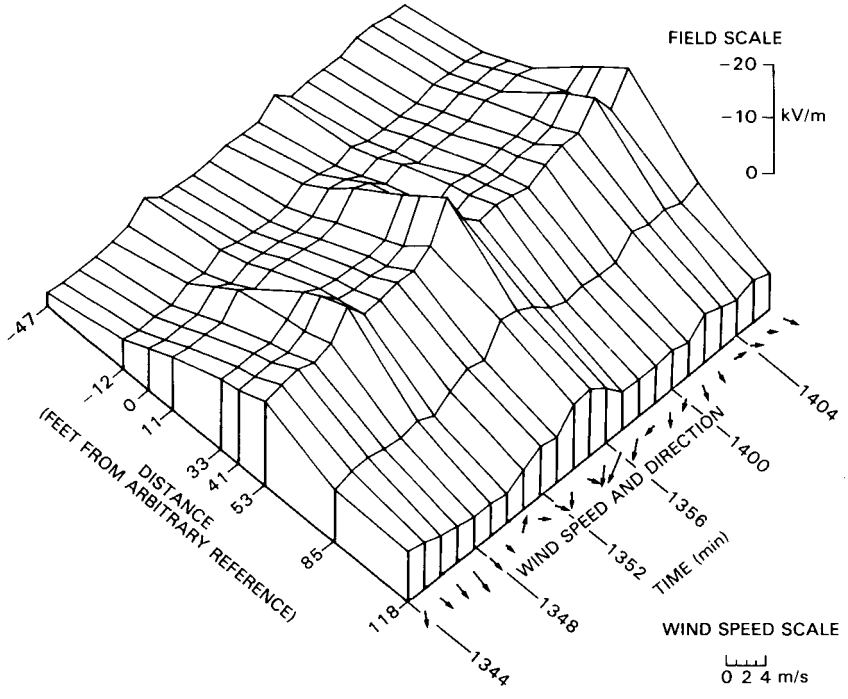

Figure 1-27. HVTRF data, 10-20-86, 1344-1406 hrs e.d.t., Line monopolar

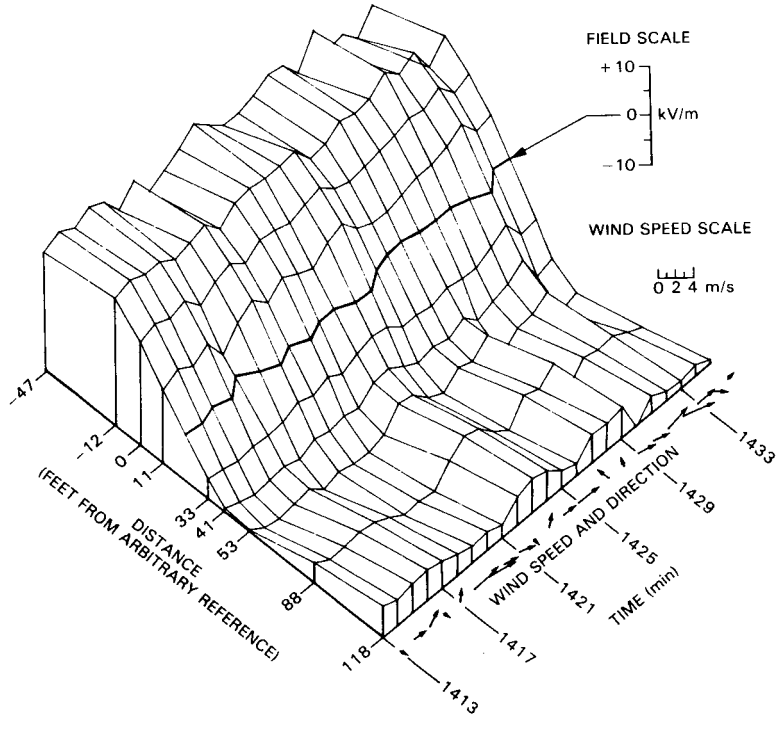

Figure 1-28. HVTRF data, 10-21-86, 1413-1435 hrs e.d.t., Line bipolar

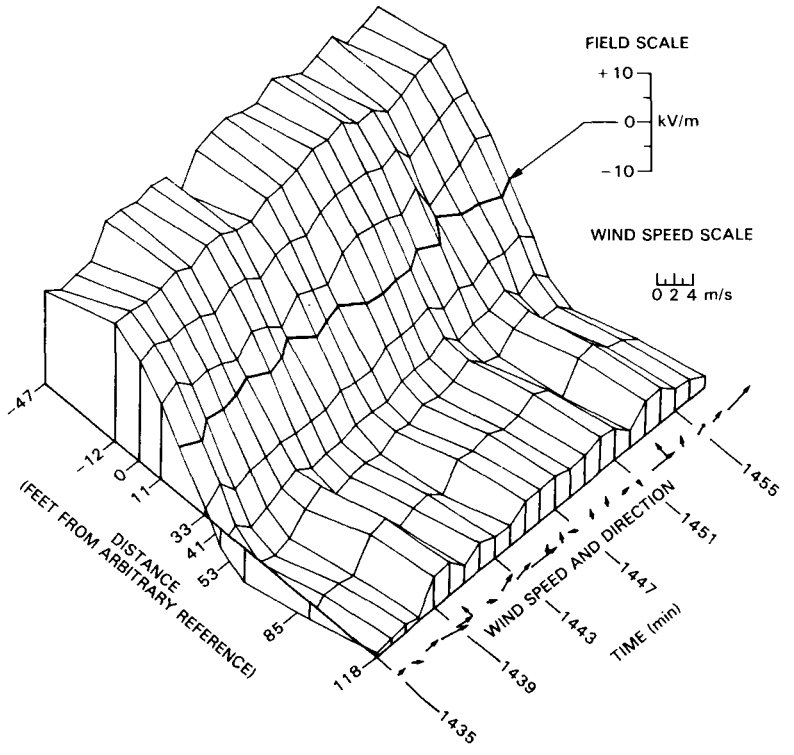

Figure 1-29. HVTRF data, 10-21-86, 1435-1457 hrs e.d.t., Line bipolar

The fluctuations with time seen in these plots are typical. There is a qualitative correlation with the perpendicular (to the HVdc conductors) component of wind velocity. Unfortunately, even though the wind was light during our visit (0-3 m/s) the one minute sampling period was too long to show movement of a charge cloud across the line directly. At even 1 m/s, a given air parcel would drift across the length of the instrumentation line in ~½ minute. However, the onset of a cross-line wind component does appear to correlate with a decrease in field, as would be expected and, with less reliability, a lateral shift in the charge peak.

On October 20, the east conductor was charged to -500 kV and the west conductor was not energized. On October 21, the west conductor was charged to +500 kV, with the system monopolar in the morning, the line was made bipolar at ±500 kV with the east conductor negative in the afternoon. The change was completed at 1307 hrs e.d.t.. The difference in cross line field profile for each condition of the line is evident from the three-dimensional plots.

1.3.3.2. Measurements and comparisons at HVTRF

A new probe shell and electronics was used for our measurements at HVTRF, which were completed after the NBS visit. The new probe was designed with a different scale factor. Our goal was to reach from ambient fields, in the neighborhood of a few hundred volts/meter and approach as nearly as possible to breakdown in air, about 30 kV/cm, with one probe, and without a change of scale on the probe. We have called the new probe the high field probe. The principal modification was to the charge measuring feedback network in the

electronics. As built, the prototype unit reaches ~5 kV/cm full scale, but laboratory measurements of a 10^5 dynamic range indicate that the goal is attainable.

All measurements at HVTRF were made with the synchronous detector receiver, which outputs directly the E_x and E_y components of field. A small bubble level attached to the base of the supporting dielectric pole provided a horizontal reference for the probe. Calibration was done in the JPL test cage just as for the NBS visit. For these measurements, modifications were made to the receiver to enable readout to be made directly in kV/m. The supporting pole was made of fiberglass tubing, the section closest to the probe being 1 cm in diameter and 1.2 m long. The remainder of the supporting pole was a larger diameter tube of the same material which was a slip-fit over the outboard section. The radioactive source was mounted on the probe housing as before. For most of the measurements, the probe and pole were supported by clamping it to a heavy, adjustable metal tripod.

An analytical estimate was made of the error caused by the presence of the tripod or an observer standing beside the tripod, 9 ft (3 m) from the sensor. The estimate was based on a textbook solution for a conducting prolate spheroid in a uniform field parallel to its major axis. The dimensions of the prolate spheroid were adjusted to approximate those of the tripod or the person. An error of about 3½% was estimated, a negligible amount. The dominant uncertainty under the transmission line was real changes in electric field caused by variations in space charge due to the wind.

1.3.3.3. Direct comparison of dc sensor to HVTRF data

The dc probe was mounted directly under the east line for a series of measurements as a function of time, to show correlations in the observed time variations. The east line was energized to -500 kV for these tests. The probe was located 18 inches (50 cm) above the ground, about 6 ft (2 m) from the corresponding HVTRF field meter in a direction parallel to the HVdc conductor.

The results are plotted in Figure 1-30, showing both our dc sensor data, and the HVTRF data from their adjacent sensor. Times throughout are e.d.t., on a 24 hour basis. These data may be compared with a similar set obtained with the beercan sensor in an earlier visit (Johnston *et al.*, 1986). As before, the time variations appear to correlate, although not perfectly. We feel the reason lies in the fluctuations inherent in the somewhat turbulent flow of air involved in the environment of light variable breezes that existed at the time. Note that the electric-field-induced ion drift velocity near ground level is rather slow, of the order of 1 to 2 m/sec, and imperfect mixing in such an environment would be quite possible. In addition, the dc sensor yielded a somewhat lower field value than the HVTRF instrumentation, an issue that has not yet been resolved.

1.3.3.4. Field profiles across the line

Two types of measurements were made with the dc sensor in free space. One was an electric field profile across the test line, and the second involved measurements around a human subject. We will first describe the line profile data.

Profiles made with the line monopolar were not interesting, since the field is essentially vertical near the ground. These data will be addressed below with respect to the possible difference observed in the field magnitude.

Similar data were taken with the line bipolar, first along a line perpendicular to the conductor with the sensor located 2.4 m (94 in) above the ground surface, and second along a vertical line midway between the conductors. The latter data were obtained with the aid of the HVTRF high-ranger (or bucket truck), and reached an extreme height of 8.5 m (28 ft). Both the vertical and horizontal components of field were read out simultaneously using the synchronous detector receiver. One exception was the point at 8.5 m, because the sensor pole was then oriented vertically, thus preventing a coordinate readout.

The results are plotted in Figure 1-31, viewing the plane of observation toward the north. The west conductor was +500 kV; the east at -500 kV. The tail of each field vector indicates the point of measurement. The field geometry is qualitatively correct, and confirms a horizontal field at the midpoint, as is expected above the ground plane. No attempt was made to correct the measured vectors for temporal fluctuations observed by the permanent instrumentation.

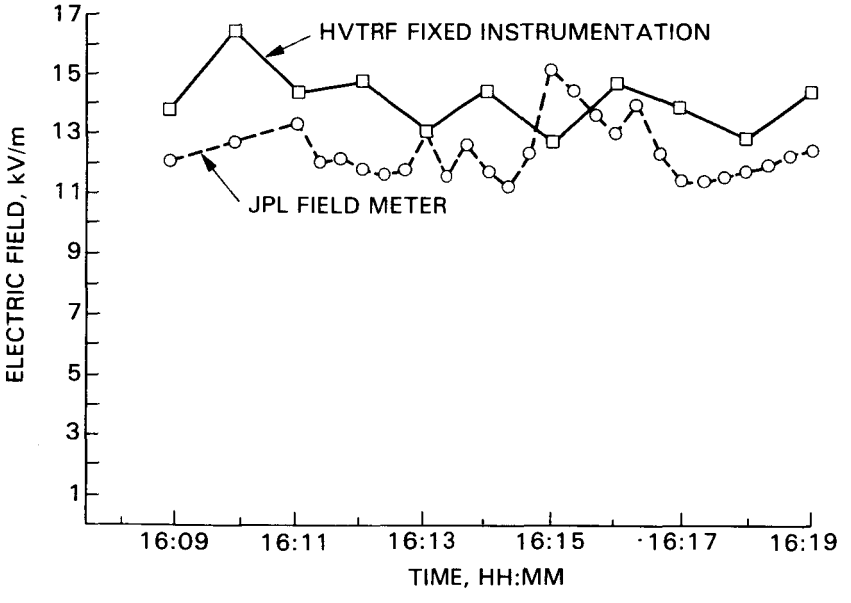

Figure 1-30. Comparison of data

Unfortunately, difficulty with the electronics in the receiver was experienced early in the first sequence (the afternoon of 10-20-86). The difficulty was later traced to a malfunctioning regulator circuit, which caused erratic behavior. As a result, all data taken before we worked on the receiver have been discarded. These data involved a cross-line profile with the line monopolar. The profile was repeated after working on the receiver. The following discussion considers only the later set of data.

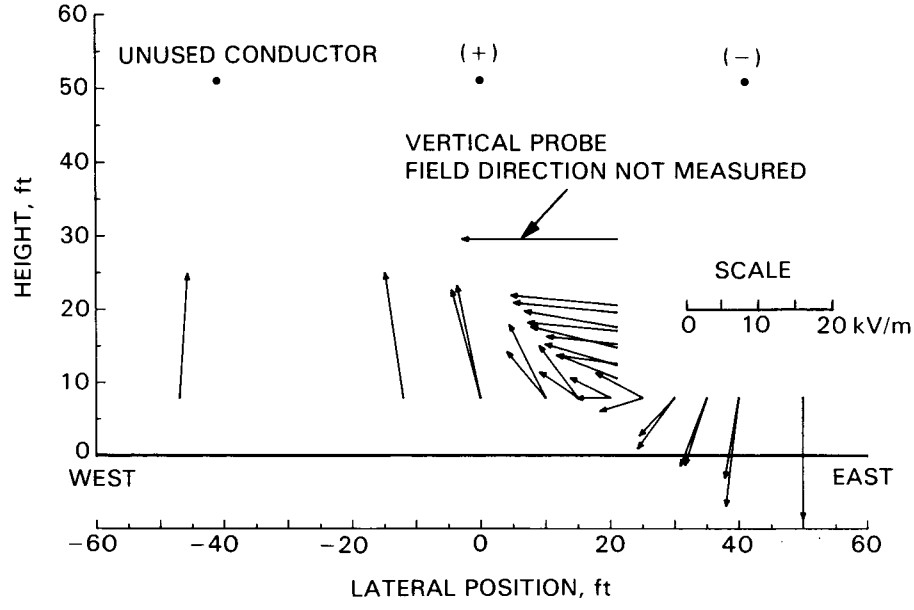

Figure 1-31. Field profile

As already mentioned, the results were not interesting as two-dimensional vector data, but were useful for comparing HVTRF and JPL calibrations. A scattergram of the data from the field meters for each data point where the JPL value and HVTRF value could be compared at the same time (within ~ ½ min) is shown in Figure 1-32. A histogram of the ratio E_v(JPL)/E_v(HVTRF) was compiled from these data, and is shown in Figure 1-33.

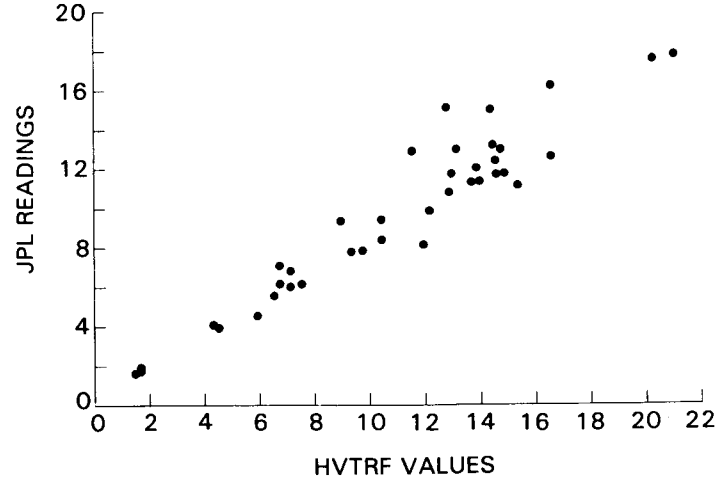

Figure 1-32. Comparison of JPL and HVTRF data

This information can be compared with results, obtained on an earlier visit, from our beercan sensor, which also yielded values which averaged 15% lower than HVTRF, but under the other test line at HVTRF. Similar procedures were used then, but different instrumentation. Note that Maruvada and his colleagues (1983) also measured field values approximately 15% less, without comment, using his large rotating cylindrical field mill. On the other hand, no similar systematic difference appeared in the 1979 field meter comparisons at HVTRF (Comber, Kotter and McKnight, 1983). We feel that the observed variance of individual values of the ratio about the mean represent real spatial fluctuations in the electric field. If this is true, a similar comparison with the two meters located closer to each other would have shown a smaller variance.

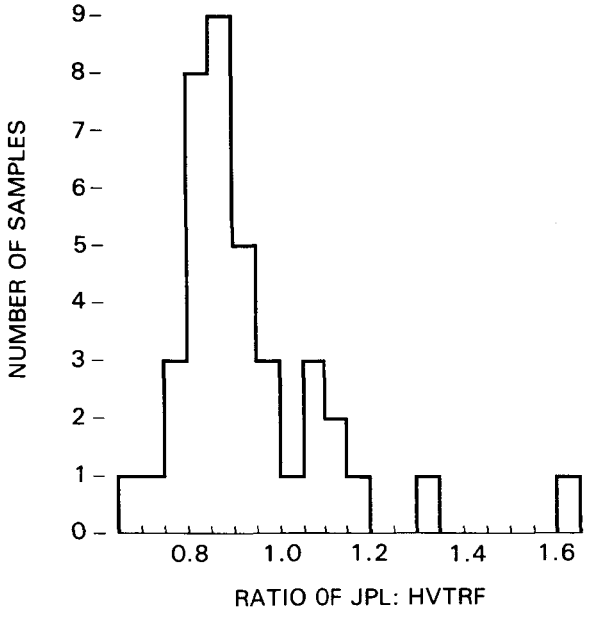

Figure 1-33. Histogram of the ratio of the readings from the two sets of instruments

Looking at the position of the peak of the histogram and its width, we can estimate that $E_v(JPL)/E_v(HVTRF) = 0.85 \pm 0.10$. For the data directly under the line, taken for the time series shown in Figure 1-30, which is a subset of the above, one obtains $E_V(JPL)/E_V(HVTRF) = 0.89$, with a standard deviation of 0.12.

Although the average difference of 11 to 15% is not large compared to the observational repeatability, and although the conclusion is not helped by our electronic malfunction, it does appear to be real. The reason for the difference is not presently understood. Resolution awaits further study, and at this time we have not determined whether to continue this investigation.

Possible causes could include one or more of the following.

1) Error in JPL sensor calibration

2) Error in HVTRF calibration

3) Local variations in field in the neighborhood of an individual HVTRF sensor

A scan at a height of approximately 40 inches (1 m) was made across the instrumentation line, that is, parallel to the conductor. The data are shown in Figure 1-34. The horizontal locations are approximate, being reconstructed from photographs, but the field values (ordinate) are accurately plotted. This is a repeat of a similar scan made earlier (Johnston *et al.*, 1986), and again shows position dependent-variations big enough to account for the difference between the observations. Detailed examination was not possible in the available time.

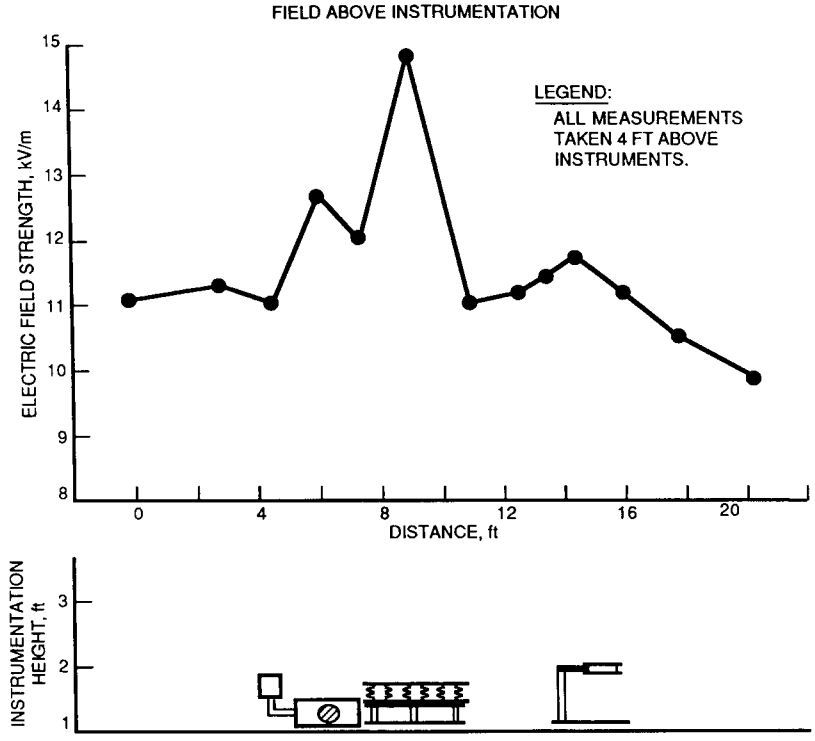

Figure 1-34. Profile across instrumentation line

1.3.3.5. Measurements around a human subject

These observations were made to illustrate further the capability of making free-space field measurements, or field mapping in an environment containing space charge. The subject was located directly under the east conductor, and many points were mapped out in the plane bisecting his body. Both face-on and

profile measurements were done, with and without a plastic hard-hat. The data, including both sensor position and field component readings were recorded photographically and reduced later. Two cameras were used, with synchronized shutters. One photographed the subject and the probe, so that their relative position was recorded. The other recorded the instrument display at the same instant. Using this approach, only 2-4 seconds were required to record one data point. A typical example of the positioning of subject and sensor are indicated in the photograph, Figure 1-35.

Figure 1-35. Instrumentation arrangement for plotting field around human subject

Figures 1-36 through 1-39 present these field maps. In Figure 1-36, the field intensity is presented directly in terms of vector length. The same data are shown again in Figure 1-37, but the vectors now represent the inverse of the field. The length of each vector corresponds to the distance over which a given potential difference would occur. The scaling used is such that the length of each vector represents a potential drop of 520 volts. The location of each measurement is at the end of the line representing the field vector closest to the subject. The inverse representation of field strength clarifies the map considerably by eliminating the overlap of the plotted vectors found in Figure 1-36.

Figures 1-38 and 1-39 present additional data in the same form as that of Figure 1-37. Figure 1-38 shows the same conditions as in Figure 1-37 except the subject is wearing a hard hat.

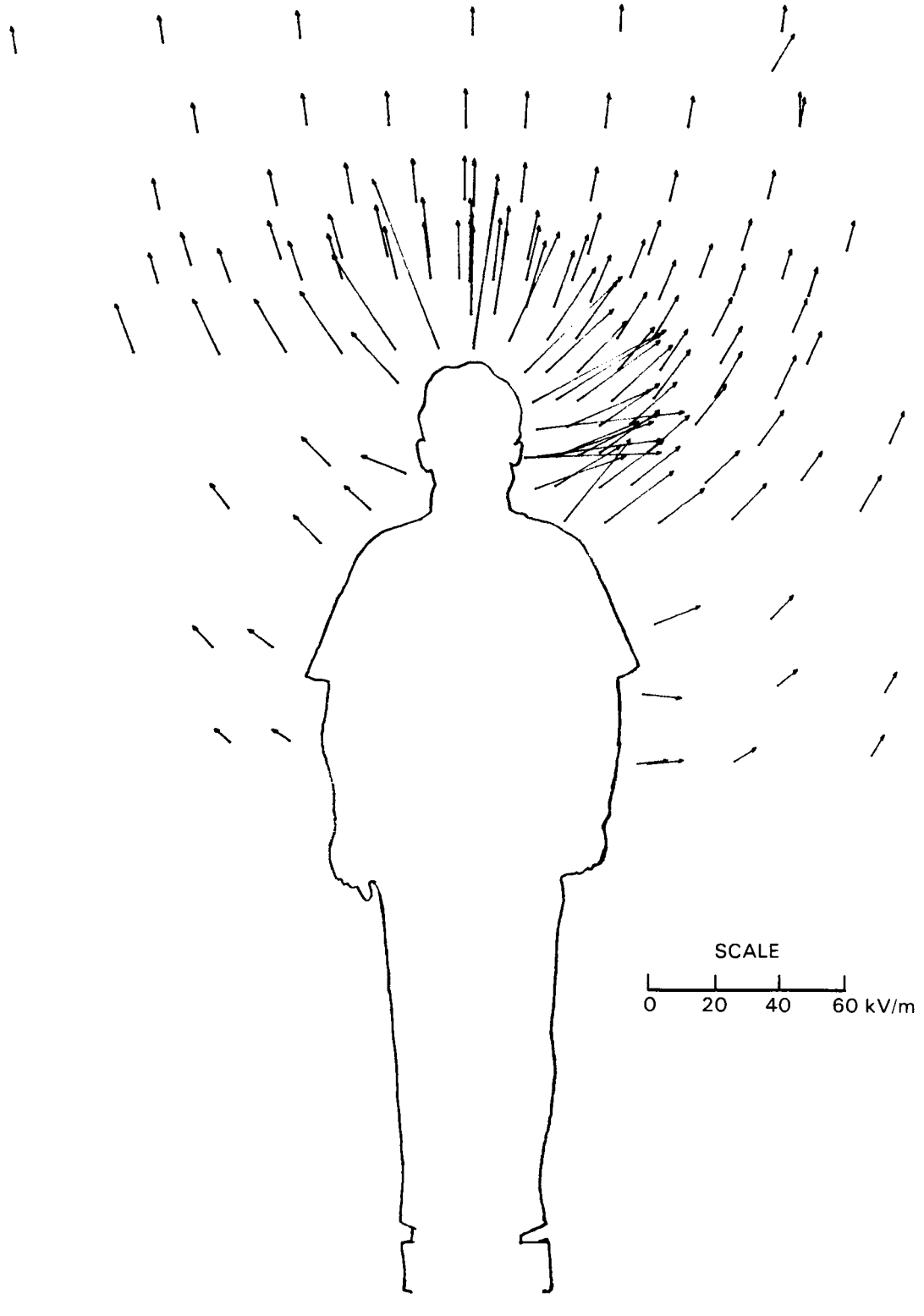

Figure 1-36. Field around human subject, front view, no hard hat

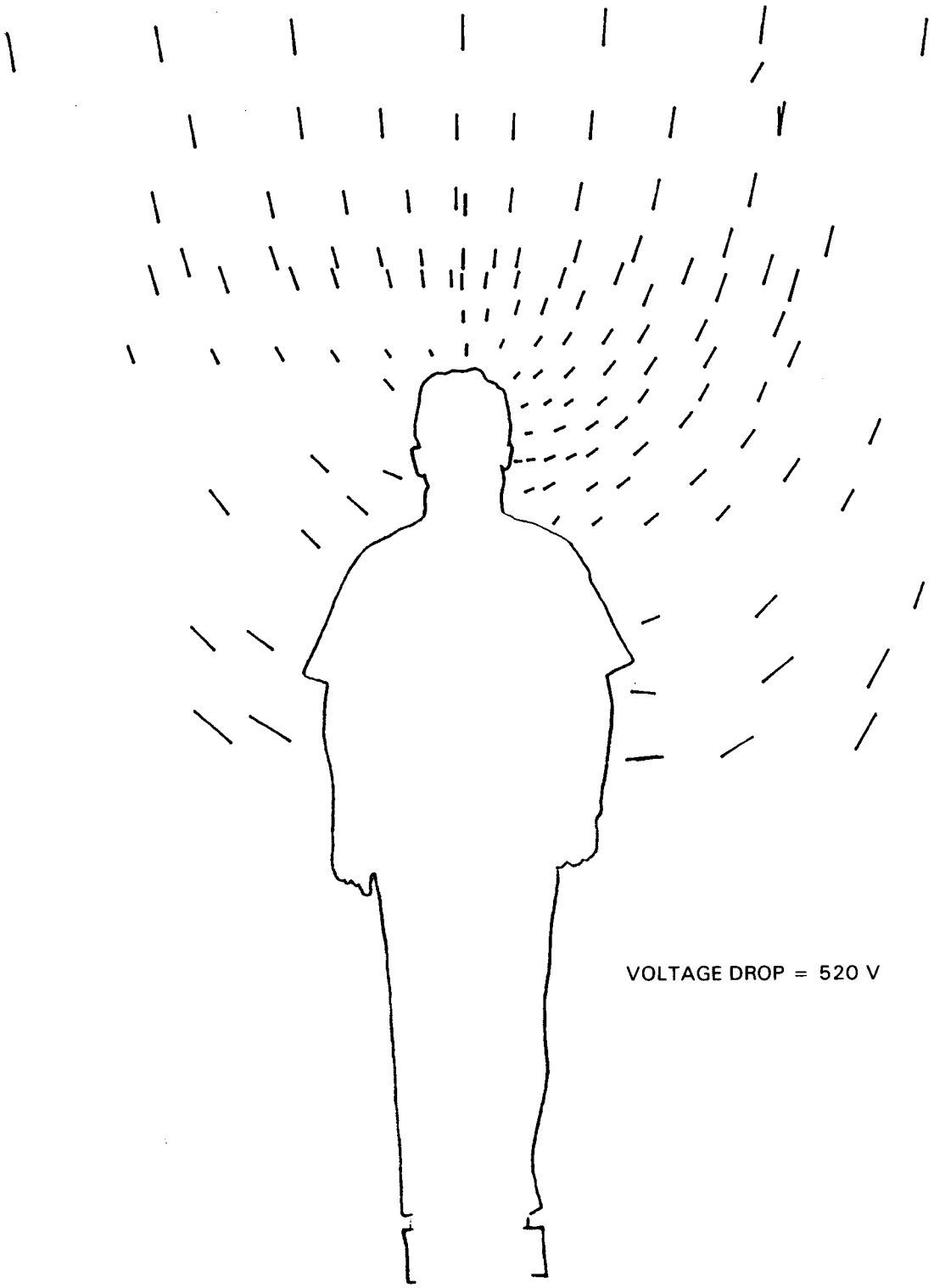

Figure 1-37. Field around human subject, length of line inversely proportional to electric field intensity

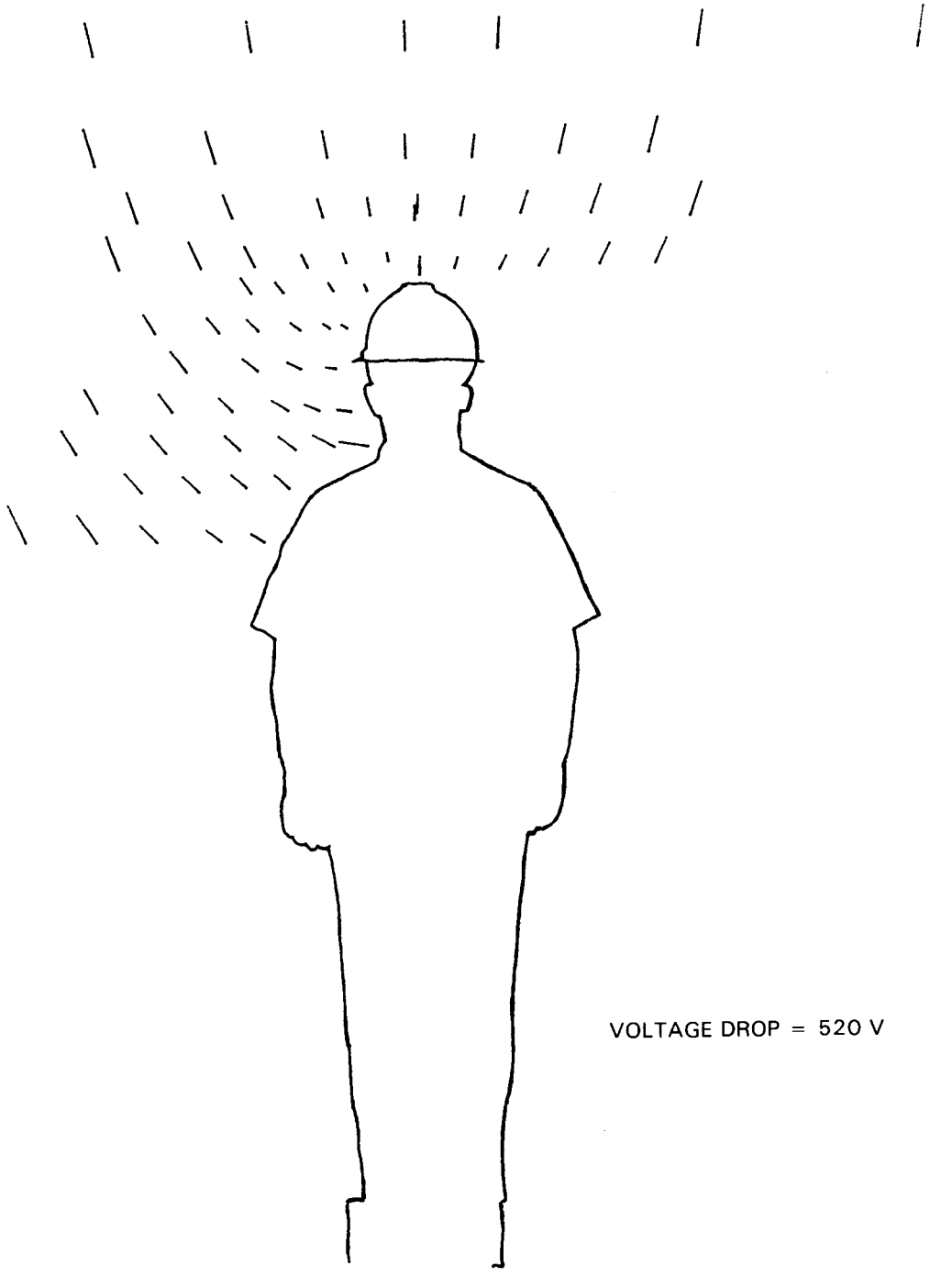

Figure 1-38. Field around human subject, with hard hat

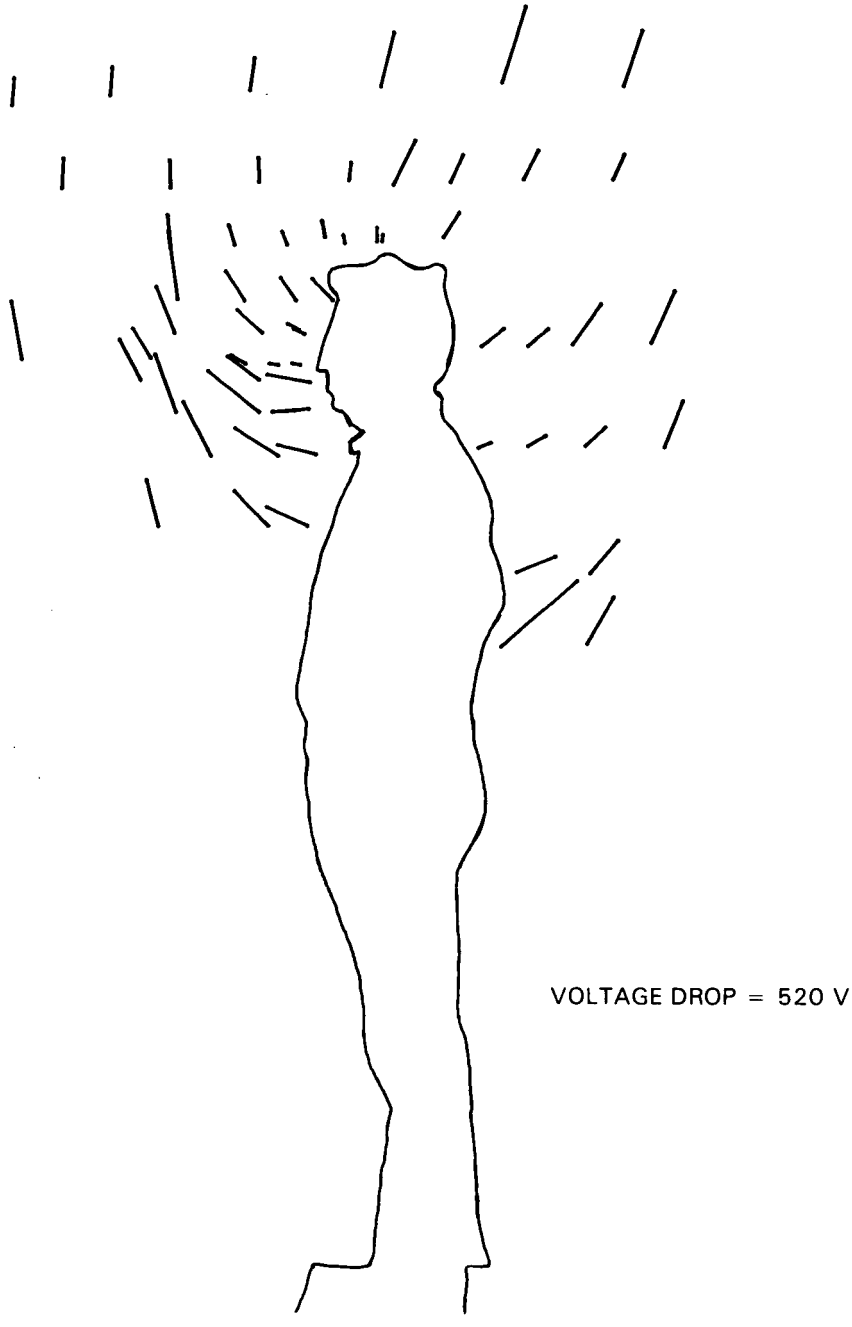

Figure 1-39. Electric field around human subject in profile

The field values over the head of the subject are observed to be 47 kV/m without a hard hat compared to 27 kV/m with a hard hat, a ratio of 1.7 in contrast to the ratio of 2.2 observed on our previous visit. The difference might be explained by a difference in resistivity between the two hard hats.

The line was monopolar for Figures 1-36, 1-37 and 1-38. Unfortunately, the subject was located under the east conductor, while the west conductor was energized to +500 kV, a fact we were unaware of until the data were analyzed later. We feel that no significant difference would have appeared in the data if the east line had been energized except that field magnitudes would have been proportionally larger. In Figure 1-39, the line was bipolar, with the east line at -500 kV and the west line still at +500 kV.

1.3.3.6. Conclusions

Our experience from these experiments indicates that field mapping with the dc sensor is both possible and convenient to do in the outdoor transmission line environment. The most time-consuming part of the data taking involved determination of the position of the probe, which we obtained photographically. A data logging system specifically designed for these measurements and which could automatically record an x, y, z position for the probe and E_x, E_y would be very convenient for field mapping. However, the photographic method is quite practical in the field. For example, the field could be determined on a 5 cm grid over a one meter square plane in about 15 minutes, allowing 2 sec per grid point, a quite practical data rate. The main disadvantage of this method is that the data must be manually transmitted to a computer later. The figures showing the field around a human subject illustrate this type of measurement.

The dominant uncertainty in all these measurements was the fluctuations in field, which are felt to be caused by the wind. It is clear that the space charge is quite variable, both over time and over space. The extreme variations over time as seen by a single detector can approach a factor of two (actually 1.8), although the standard deviation was much smaller, near ±10%.

Surprisingly, the variations between two sensors less than 10 ft apart appear to be just as large, indicating that the charge variations are of the order of a few feet across. However, an indication from the HVTRF data that the field variations are usually slow does not strongly support the idea that small scale fluctuations in space charge are important. It would be very interesting to obtain similar data with much better time resolution, say ~1 second. With this kind of time resolution, the three-dimensional plots shown earlier should show the motion of individual charge clouds.

A technique that may be useful for field mapping under these conditions is to use a second probe as a reference to adjust the data taken over a period of time with the moveable probe. To be effective, the region of interest must be smaller than the physical size of the charge fluctuations and as close as possible to the measurement probe without interfering with it. Figure 1-32 gives an indication of how effective this technique might be on a region approximately 3 m (10 ft) across.

Another type of measurement would be to observe the field downwind of the line, on occasions when the wind is across the line. Both surface field and free space measurements of field could yield data useful for mapping the downwind drift of a charge cloud from the conductors. Differences in charge distribution related to convective (daytime) and stable (nighttime) airflow might be determined.

Finally, an intriguing result has been that the 10-15% difference between calibrations on our sensor and the HVTRF line that was noted on the prior visit persists. Although the difference is masked by the normal field fluctuations, and by an intermittent electronic problem that we now think we understand, we feel it is real. The cause is unknown and must await further investigation to be determined.

PART 2

THE AC FIELD METER SYSTEM

2. THE AC FIELD METER SYSTEM

2.1. Introduction

The problems of measuring ac electric fields are far easier than those of making the same measurement in an dc field. In fact, devices to make space-potential ac electric field measurements have existed for some while. One such instrument which has been used in the power industry is described by Deno and Zaffanella (1975). In this device, the sensing probe and the readout are integrated into one housing, which is held beyond arms length at the end of a fiberglass pole during operation. It was the existence of this meter, and others like it, that pointed up the non-availability of such instrumentation for dc fields.

The capabilities and features of the existing ac field meters provided, in a way, the baseline performance parameters for the DOE dc field meter system. While this was never stated explicitly, it should be clear that the overall object of the dc field meter development was to put the measurement of dc fields on an equal footing with ac fields.

Consequently, as the dc meter was being evaluated, comparisons of its performance with the performance of similar instruments designed for ac use seemed natural. While the dc field meter is somewhat more complicated, it provides performance advantages in several areas over its ac counterpart:

Size: The dc probe is smaller than most commonly used ac probes. This means that readings can be obtained of fields that are uniform in extent over quite small regions. The unit can be used close to distorting objects.

Dynamic Range: The dynamic range of the dc probe is so large that range switching on the probe is unnecessary. This means that there is no need to know the approximate value of the field before measuring it. In addition, the probe can be moved from a low field region into a high field region without the need to approach it.

Power: The probe had no externally controllable power on/off switch. There was no need to approach the probe to turn it on prior to a measurement, or to turn it off afterwards.

Data Acquisition: The DOE dc field meter can be readily connected to a data acquisition system. This is not always true of space potential instruments.

While some of these improvements in performance arose specifically from improvements made to solve the problem of dc measurements, it seemed natural to ask whether some of these advantages could be retained in a redesign of the system for use in ac fields.

Size: The small size of the dc probe was made possible because of the use of hybrid integrated circuit techniques, and because of the small size of

the drive motor (turbine). An ac probe could use similar electronics, and would not need a drive motor.

Dynamic Range: The large dynamic range of the dc probe was largely a result of the use of coherent (synchronous) detection. This approach could also be implemented in the case of an ac probe, even though a synchronous reference pulse was not readily available.

Power: The lack of power switch of the dc probe was a response to the size goals of the design, and took advantage of the rotation of the sensor head. This option would not be available in an ac probe.

Data Acquisition: The dc meter could be connected to a data acquisition system because part of the meter system was at ground potential, interconnected with the probe by means of fiber optics. This design feature could readily be retained in an ac design.

It was therefore undertaken to design an ac field meter that retained as many of the advantages of the dc meter as possible.

2.2. Design

2.2.1. Design Approach

The shape of most existing field meters has been governed by the need to include the readout device in the probe. Accordingly, the side of the probe facing the operator was flat, and the probe overall was box-shaped. Since the proposed ac field meter did not need to rotate, and the readout would be at the remote end of a fiber optic cable, its shape could be chosen arbitrarily. A spherical shape has two advantages: its sensitivity can be calculated from theoretical considerations, and it results in minimum disturbance of the field. Therefore, this shape was chosen for the DOE ac field meter probe.

Spherical field meters have been built, but have not been used to any significant extent in the power industry. A small spherical probe was built by Misakian, Kotter and Kahler (1978) at the National Bureau of Standards. This probe was only 1.2 cm in diameter, and contained no electronics. The system was designed for use in the uniform field of a test cage. However, it was not truly a space-potential device since the probe was connected to its battery-operated electronics by means of a pair of conductors, and space potential was guaranteed by adjustment of an external circuit. In the test cage for which it was designed, the equipotential forced by the output wires was unimportant: the wires could be arranged to be along known equipotential lines.

More recently, in Germany, Feser and Pfaff (1984) built a spherical probe for the measurement of transient electric fields. This probe was similar in some respects to the one we proposed to build; however, the device was quite large (4 cm diameter) perhaps because it was designed to give the x- and y-components of a transient electric field. A somewhat simpler probe was built by Gorakhpurwalla, Cooper and Johnson (1984). This device contained battery-operated electronics, and was 4 in (10.16 cm) in diameter. A different

approach was taken by Friedmann, Curzon, Feeley, Young and Auchinleck (1982). Their probe consisted of a gas-filled bulb 2.5 cm in diameter, and contained no metal parts. The device had the interesting property that it had no directional sensitivity. Its dynamic range was rather small, however.

The size of the DOE ac field meter probe was set by the fact that a suitable hybrid IC had already been designed for the dc probe. A hollow spherical probe of only 1 cm radius (2 cm diameter) would be less than half filled by the existing hybrid IC. This choice would leave a space of equal size for the power source. While it seemed possible to make an even smaller probe, the extra work involved did not seem justified.

As far as possible, the design of the ac field meter was based on that of the dc meter. The probe uses the same IC, with some slightly different component values, and the receiver uses a similar coherent detection method. The method of energizing the probe is, however, quite different.

2.2.2. Power Source

It was intended from the outset to use a photoelectric source for the ac field meter probe[1]. The approach is discussed by Kirkham *et al.* (1984) and work done on the problem is described by Johnston *et al.* (1986). Figure 2-1 shows the proposed means of optically energizing the probe electronics.

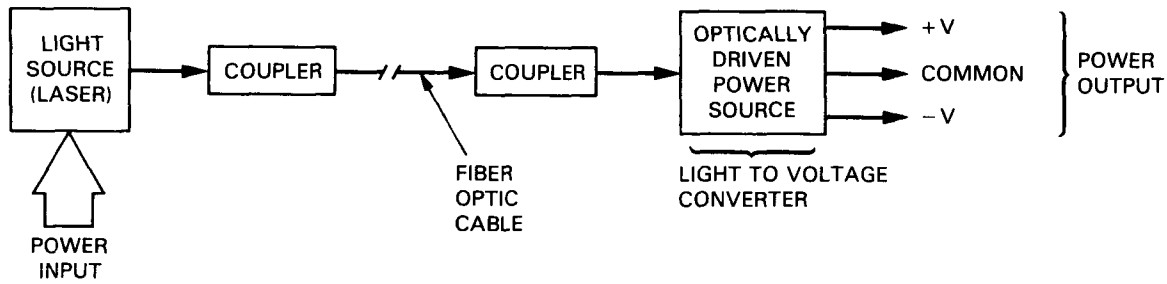

Figure 2-1. Block diagram of optical power transfer scheme

2.2.2.1. Integrated-circuit photodiode array

A small integrated-circuit array of photodiodes was designed to power the ac probe. While production problems eventually forced us to use another approach for the prototype probe, several samples of the IC array were made.

Fabrication of the photodiode array starts with the epitaxial growth of three layers on a semi-insulating (SI) GaAs substrate. The SI substrate is required because of the need for series connection of the photodiodes. The layer parameters are summarized in Table 2-1.

---

[1]In fact, it had originally been planned to use optical power to energize the electronics of the dc sensor probe. However, delays in designing and producing the required photodiode arrays required us to use batteries instead.

TABLE 2-1. LAYER PARAMETERS

Material	Thickness (μm)	Doping ($\times 10^{17} cm^{-3}$)
n-GaAs	3.0	5 to 7
p-GaAs	0.5	1 to 3
p-$Al_xGa_{1-x}As$, x>0.85	0.2	>10

The first photolithography/etching process involves removal of the top two layers to enable subsequent contacting to the n-GaAs layer. Next the individual photodiodes are defined by etching the n-GaAs layer to provide isolation between the diodes. A 20 μm SiO_2 layer is RF sputtered and photolithographically defined both to passivate the p-n junction and to prevent electrical shorts when contact metallization is applied. The AuGe/Au contacts (6 μm/10 μm thick) connecting adjacent devices are then thermally evaporated. The contact pads (for external connection) are evaporated of Cr (2-3 μm) and Au (10 μm) to provide for better adhesion to the SI substrate. Both metallization steps are implemented through a lift-off process. The contacts are sintered at 400 °C for one minute, and finally SiO is deposited on top of the array as an antireflection coating layer.

The fabrication process requires six masks, for p-layer etching; n-layer etching; SiO_2 definition; AuGe/Au contact definition; contact-pad definition and SiO definition.

A cross-section of one photodiode of the array with its connection to the adjacent photodiode is shown in Figure 2-2. (The anti-reflection layer is not shown.) A top view of the photodiode array is shown in Figure 2-3. The array consists of 16 diodes which are connected in series in four groups of four elements each. Since the operating voltage of each photodiode is approximately 0.9 V, the array can produce the versatile voltage combinations of 14.4V, $\pm$7.2V, or 2$\times(\pm$3.6V).

The active area of each photodiode in the current array design is approximately 750 $\times$ 750 μm^2, and the entire array size is approximately 3.2 $\times$ 3.2 mm^2. An I-V curve of the photodiode array is shown in Figure 2-4.

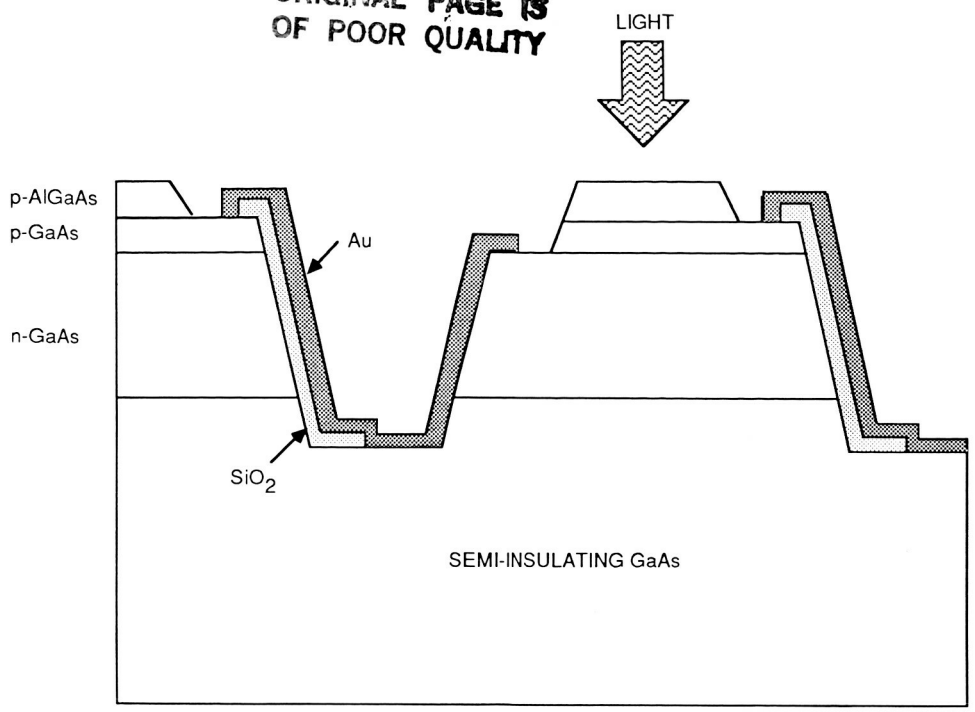

Figure 2-2. Cross section of diode array

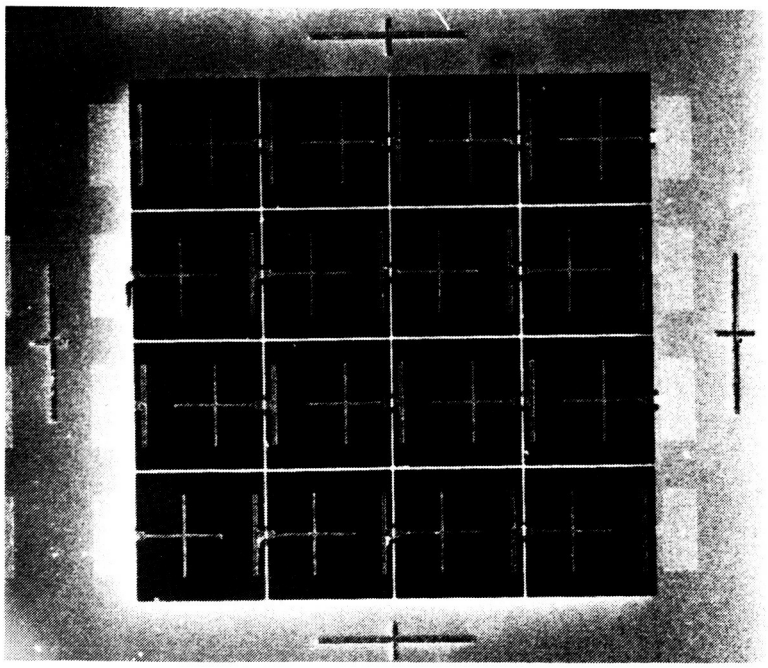

Figure 2-3. Top view of photodiode array

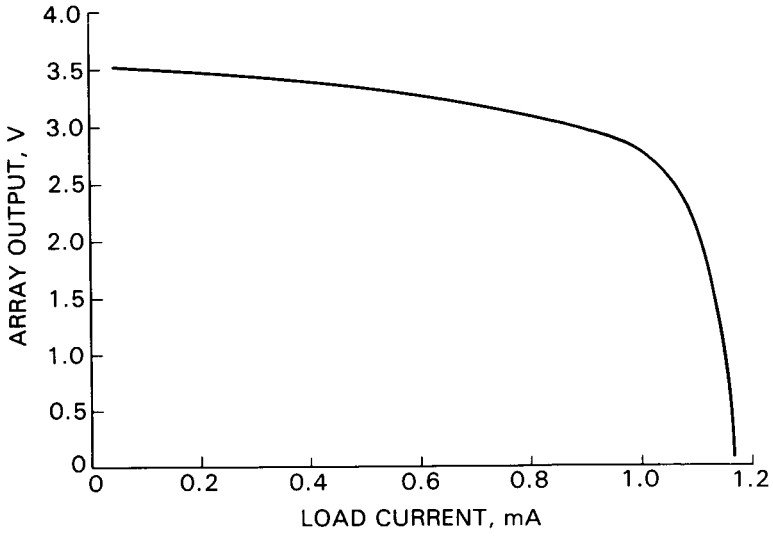

Figure 2-4. I-V curve of photodiode array

Measured efficiency of the photodiode array is approximately 10%. It can be increased by a decrease in the series resistance, brought about by optimization of the layer doping and thickness, a better contact pattern, and improvements in the anti-reflection layer.

2.2.2.2. Hybrid photodiode array

Only a small number of samples of the IC array were produced. Because of the fact that the power source had been the pacing item on the development of the ac meter for so long (about 2 years), it was eventually decided to power the prototype ac probe by means of a hybrid (rather than integrated) array.

For some while, the quality of the material and the processing of the gallium arsenide had been gauged by producing small diodes on test wafers. These diodes had been routinely produced, for example, to test the uniformity of the growth of an epitaxial layer across the surface of a 3 in (7.6 cm) wafer. The diodes are simply produced, and tested by cleaving the wafer after metallization of the contacts. Each diode is about 0.1 inch (2.5 mm) in diameter. Usually, each diode is tested as part of a square of material a little over 0.1 in on a side.

For our purposes, four diodes were required to produce the voltage level needed for both the positive and the negative power supply, making a total of eight in all. Eight diodes of this size would have required eight fibers to illuminate them, an impractical proposition. Therefore, the approach of further cleaving the diodes was adopted. By dividing each circular diode in half, and then again dividing each half, a set of four diodes little larger than the original circular one were made. The JPL hybrid laboratory interconnected the four in series on a small insulating substrate (because, in general, the diodes were not built on SI material), and mounted the group on the rear of the header used for the probe electronics.

The hybrid array, mounted on the TO-8 header, is shown in Figure 2-5.

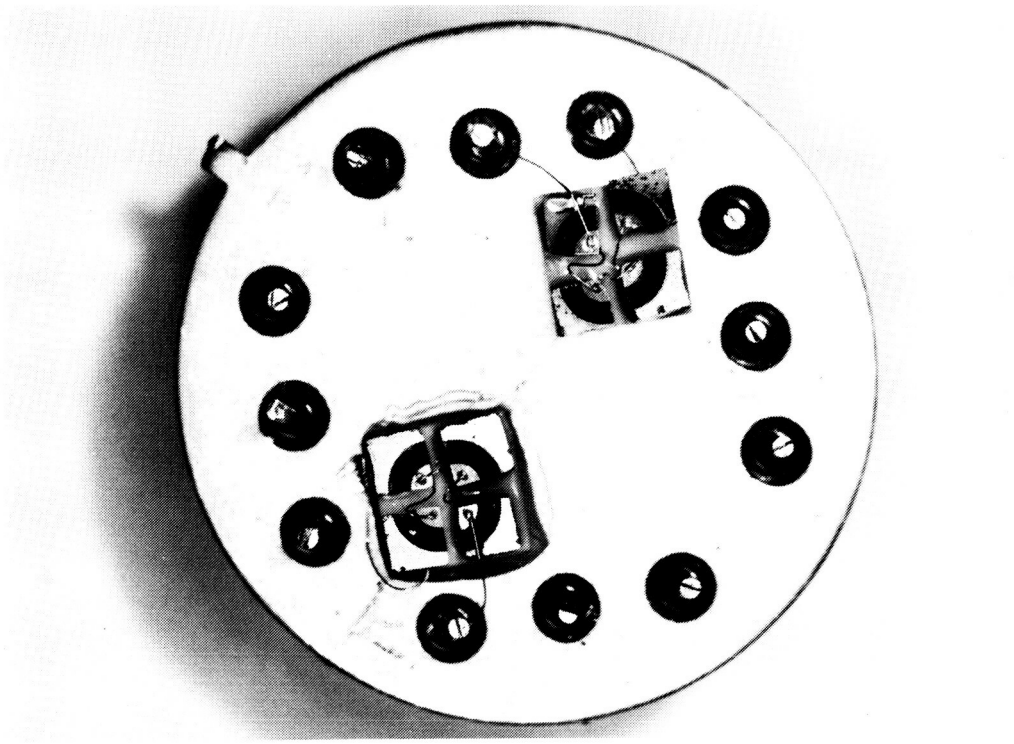

Figure 2-5. Hybrid photodiode array

2.2.3. Mechanical Design

The DOE ac field meter probe is mechanically very straightforward, as shown in Figure 2-6.

The outer shell of the probe forms the electrode pair, in much the same way that the shell of the dc probe comprises the semi-cylindrical electrodes of that device. In the case of the ac meter, the electrodes are spherical. Since there is no motion associated with the ac meter, there is no need to consider the weight of the structure or its balance. Spun brass hemispheres, with an outside diameter of 2 cm, form a relatively simple and sturdy housing for the device.

Inside the sphere, the various parts are held in the proper relative position by two pieces of machined phenolic material. One piece holds the hybrid integrated circuit, and insulates it from the electrodes. Both electrodes are attached to this piece. The other phenolic part is attached to one of the electrodes, and is used to hold the entire assembly to the handle.

Three optical fibers are used. Two bring power to the electronics, via the gallium arsenide photodiode arrays described above. There is an air gap of about 4 mm between the ends of the fibers and the diode arrays, to allow the incident power to spread over the entire array. The other fiber has an LED attached to it, and carries the data from the probe to the receiver. The three fibers are held against a fiberglass "paddle" as they enter the probe. This provides a measure of mechanical support for the fibers.

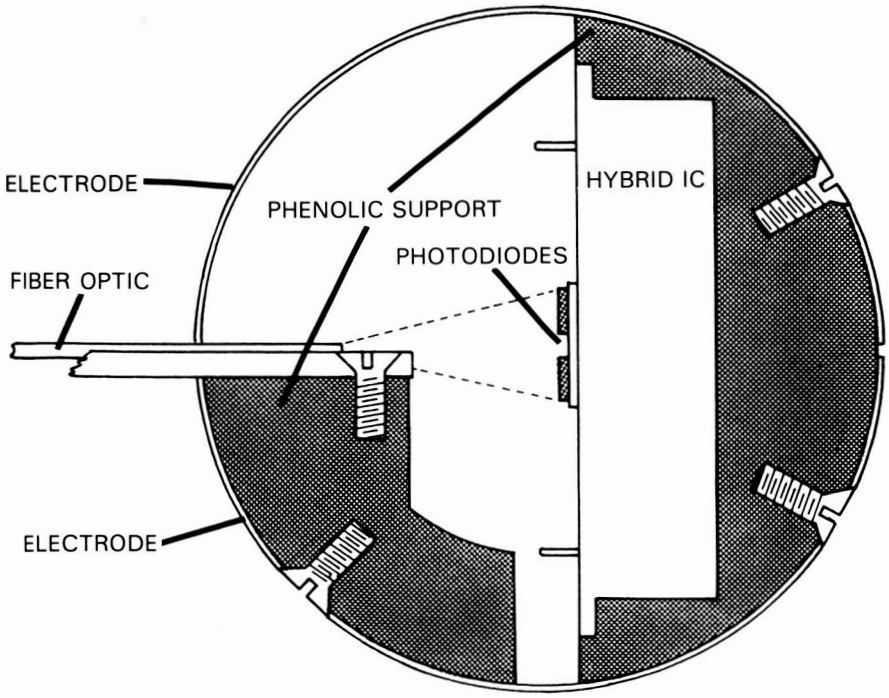

Figure 2-6. Cross section through the ac field meter probe

There is a small rectangular opening in the shell to admit the paddle. The opening is about 1 cm wide and 1 mm high. The "missing" electrode area is therefore about 0.1 cm^2. Since the total surface area of the electrodes is over 12.5 cm^2, the error caused by the opening is not likely to be significant.

Figure 2-7 shows the completed probe with one of the electrodes removed to reveal the interior.

2.2.4. Electrical Design

The ac field meter was designed to take advantage of the work already done for the dc meter. Accordingly, the two are very similar indeed electronically.

2.2.4.1. Probe Design

The probe electronics for the ac probe is based on the same data encoding scheme as the dc probe. A charge measurement circuit modulates a VCO, which produces short optical pulses at a frequency proportional to the input current. The configuration of the hybrid is identical to the hybrid used in the dc meter; the values of some of the components are changed because of the different size of the electrodes, and the lower frequency of the input.

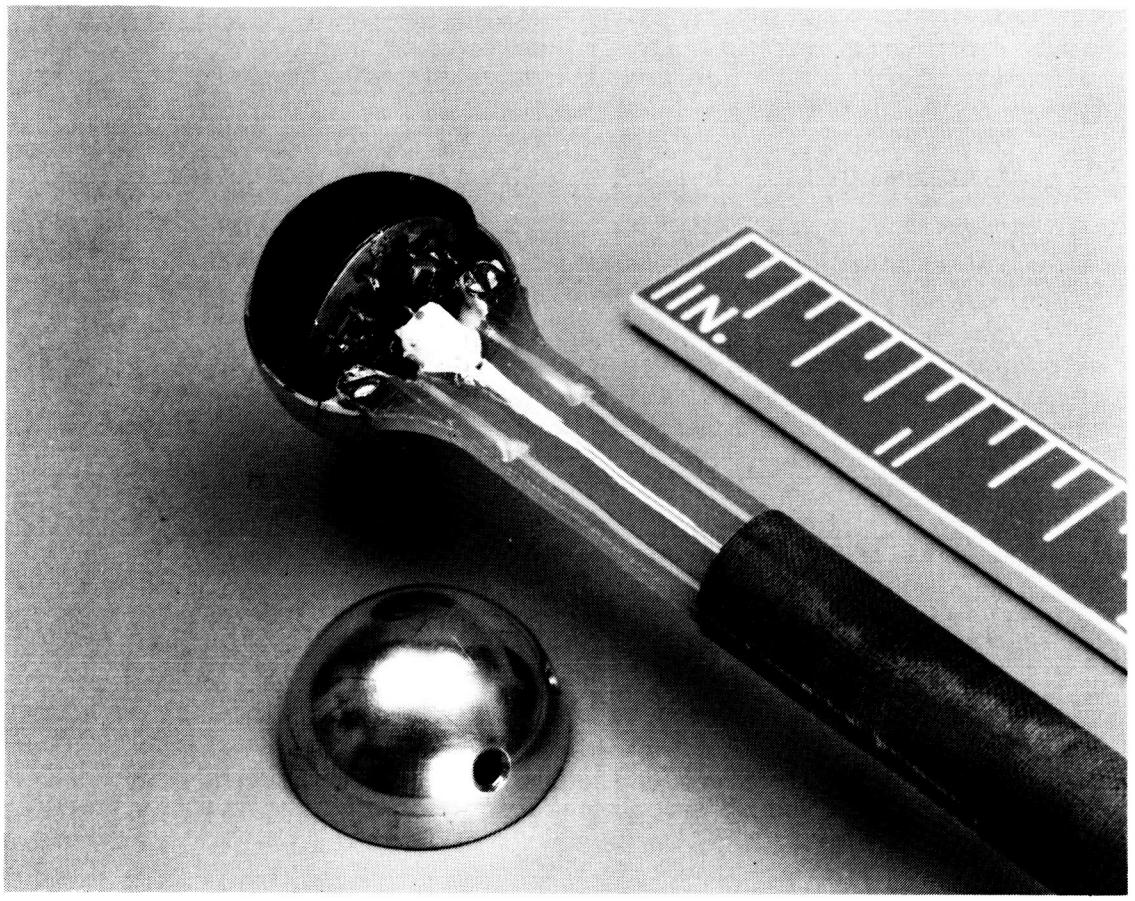

Figure 2-7. Photograph of the ac probe with one hemisphere removed

Additional changes were made to accommodate the limited power available from the optical power source. A low-power amplifier was used in the first stage of the probe, and the frequency of the VCO was decreased. In the prototype system, about half the power of the IC was dissipated in the first stage. This power was the quiescent power of the operational amplifier used. When this was reduced by the use of a different amplifier, the dominant power user in the hybrid became the LED transmitter.

With optical pulses as narrow as practical (~100 ns), the power was further reduced by decreasing the free running frequency of the VCO to 10 kHz. This was 9 times lower than the frequency of the VCO in the probe of the dc probe, and further reduced the power consumption. The first miniaturized dc probe had consumed 8.4 mW — the power demand of the final ac probe was less than 2 mW.

Active "zener" diodes were used to stabilize the voltage applied to the hybrid IC. There are small power variations caused by changes in the fiber loss as the fiber is bent during normal use. It was found that, without stabilization, these power fluctuations resulted in large changes in the power supply voltage,

and modulation of the VCO. While this modulation is not at power frequency, it did add low frequency noise to the signal. The lock range was therefore reduced at small signal. The zener diodes completely eliminated this effect.

2.2.4.2. Receiver design

Since the data encoding method is the same as that used for the dc meter, it may be expected that the receiver design is similar, and indeed, such is the case. There are two differences. They arise from the fact that the dc meter has a synchronous reference pulse obtained from the rotating shell of the probe, and there is no corresponding pulse in the case of the ac meter. This reference pulse enables the dc meter to use coherent detection in a very straightforward way, and to present the data resolved into two components.

Without the reference pulse, coherent detection becomes more difficult, and the output cannot be resolved into components. During development, envelope detection (rather than synchronous detection) was evaluated for this application, in view of its simplicity. The dynamic range was found to be much less than that of the dc meter. It became clear that synchronous detection would have to be used to achieve the potential dynamic range of the instrument.

One of the early uses of the phase locked loop, before it became available on an integrated circuit, was the tracking filter. In particular, the PLL was applied to the problem of recovering signals deeply embedded in noise. Much of this work was done at the Jet Propulsion Laboratory (see, for example, Gilchriest, 1964)[1] where the object was to recover the weak signals from distant spacecraft. Apart from the much lower frequencies involved, our present problem is the same.

It is convenient to view the problem in terms of a radio receiver. The system consists of a frequency modulated carrier where the modulation happens to be at a fixed frequency (60 Hz, in the case of the ac meter). It is the amplitude of the modulation signal (i.e., the magnitude of the 60 Hz signal) that is of interest. A phase locked loop is readily used for the FM demodulation, because the FM carrier is very strong (the 10 kHz optical pulse train). Unfortunately, the process of frequency modulating the carrier, and particularly the process of demodulating it, results in the addition of a large amount of noise to the recovered modulation.

This is particularly true of the kind of data link used in the field meter. With a large modulating signal, the carrier frequency can be significantly different from its nominal value, and may even approach zero. No demodulating scheme could be expected to reproduce the modulation when the carrier frequency is so low. Distortion caused by very low carrier frequency has been observed on the recovered signal at large fields. It is, nevertheless, a straightforward matter to recover the signal.

---

[1]Coincidentally, Carl Gilchriest was, during the early 1980s, the Manager of the JPL Project that later did the work reported here.

At the other extreme, with a very small signal, the noise of the carrier demodulation process may be larger than the signal itself. In the limit, even with no modulation, there will be noise at the FM detector. The problem of recovering a signal from this noise presents more challenge.

In a manner analogous to the application of a PLL to the problem of reception of weak AM signals, it is possible to use phase lock to measure the amplitude. Because the error voltage in the loop can be extensively filtered, a clean switching signal can be generated by phase locking an oscillator (at the modulation frequency of 60 Hz) to this (noisy) input signal. Only loop response speed is lost as the filtering becomes more extensive. The frequency of the signal, i.e., the power system, is unlikely to change appreciably, either in the short term or the long term.

The switching signals for the ac field meter are derived by means of a phase locked loop from the signal itself, whereas in the dc meter, these signals were derived from the synchronous reference pulse. Figure 2-8 compares the receivers of the dc meter and the ac meter.

Advantage was taken of the fact that a printed circuit had been designed for the dc field meter receiver. A small number of changes converted this circuit into one suitable for use as the receiver of the ac meter. Thus, the components were changed so that the PLL in the data channel had a free running frequency of 10 kHz, to match the probe used. The PLL used to generate the quadrature switching signals, originally in what was described as the reference channel, was modified to have a free running frequency of 4×60 Hz. One of the two synchronous switches was used as the phase detector for this loop, so that the loop locked to the signal rather than the external reference.[1] The panel meter originally used to display the magnitude of the signal component was retained as a lock indicator.

In the time since the dc meter was developed, an improved synchronous detector was designed. This circuit, based on the "conditional inverter", performs full-wave detection of the signal. The arrangement is shown in Figure 2-9.

[1] It is usual, in the design of radio receivers, to have two phase detectors in the PLL system. One acts as the synchronous detector, and the other generates the loop error signal, as here. The two phase detectors are usually operated in phase quadrature by phase shifting the signal 90 degrees. Since the logic to generate quadrature switching signals (rather than quadrature versions of the received signal) had already been developed for the dc meter, that approach was retained here.

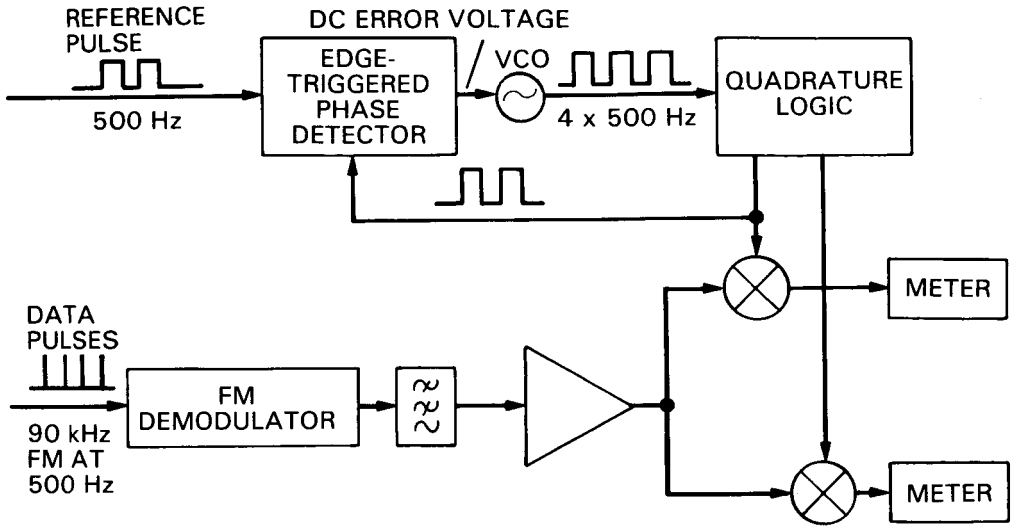

(a) DC FIELD METER RECEIVER

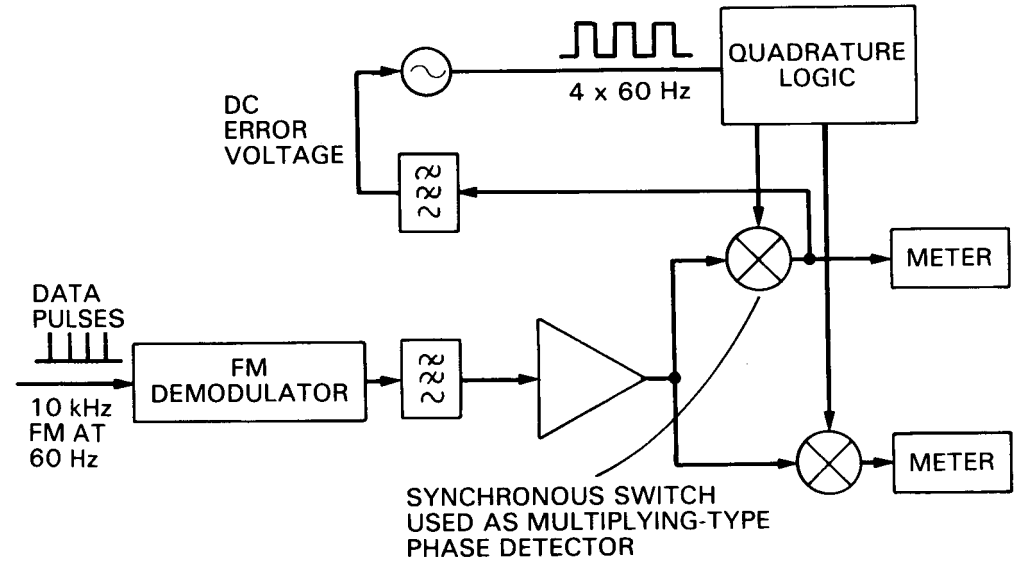

(b) AC FIELD METER RECEIVER

Figure 2-8. Block diagram of the dc and ac field meter receivers

Passive filtering was used to drive the panel meters, without further amplification. The receiver gain distribution was adjusted so that there was no range changing after the synchronous switch. This, and the use of high-quality amplifiers in the conditional inverter stage, eliminated the need for an output offset adjustment.

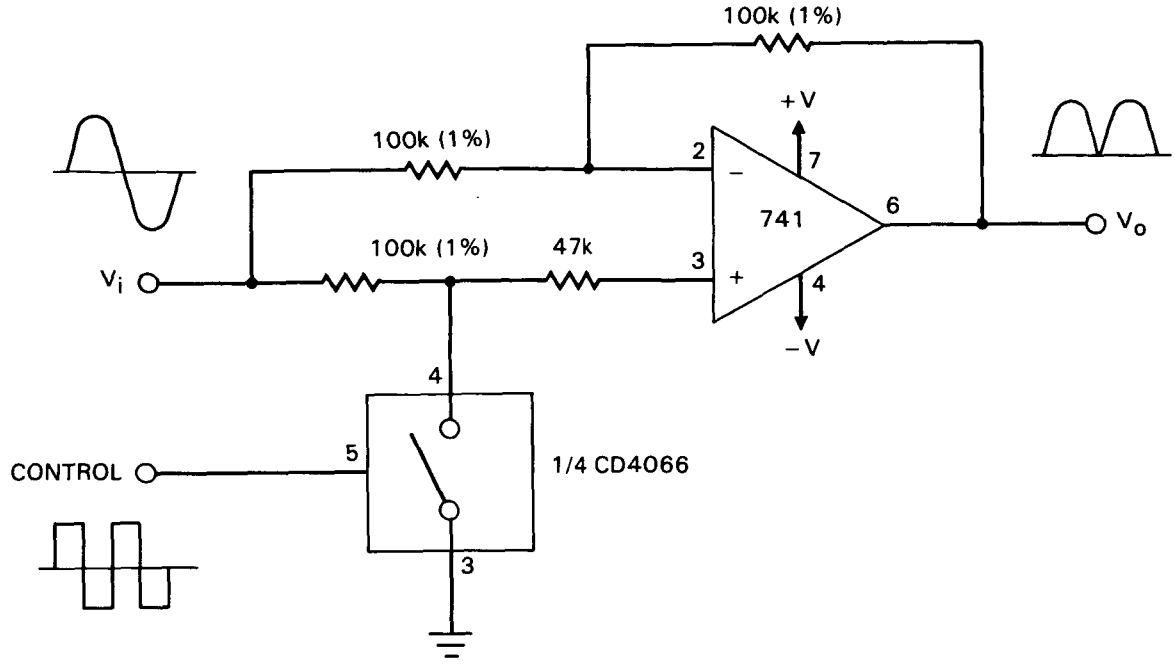

Figure 2-9. Conditional inverter

Apart from these changes, the ac meter has a laser power supply that has no counterpart in the dc meter. Multi-stripe laser diodes are particularly susceptible to damage by noise spikes in the power supply. The circuit used here provides a stable current source for the lasers, and an extensively filtered supply.

Figures 2-10 through 2-12 show the complete circuit.

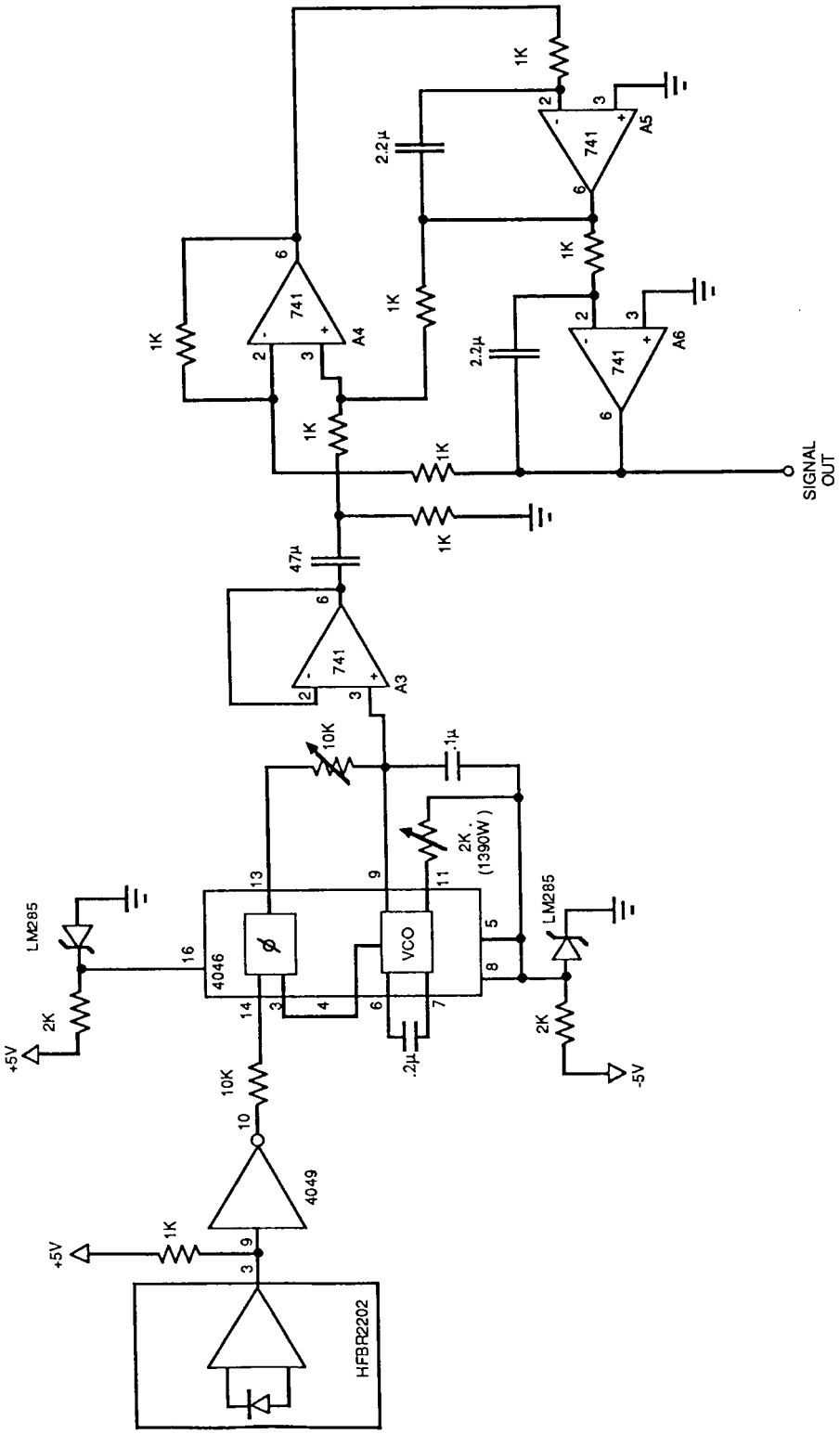

Figure 2-10. Receiver data channel

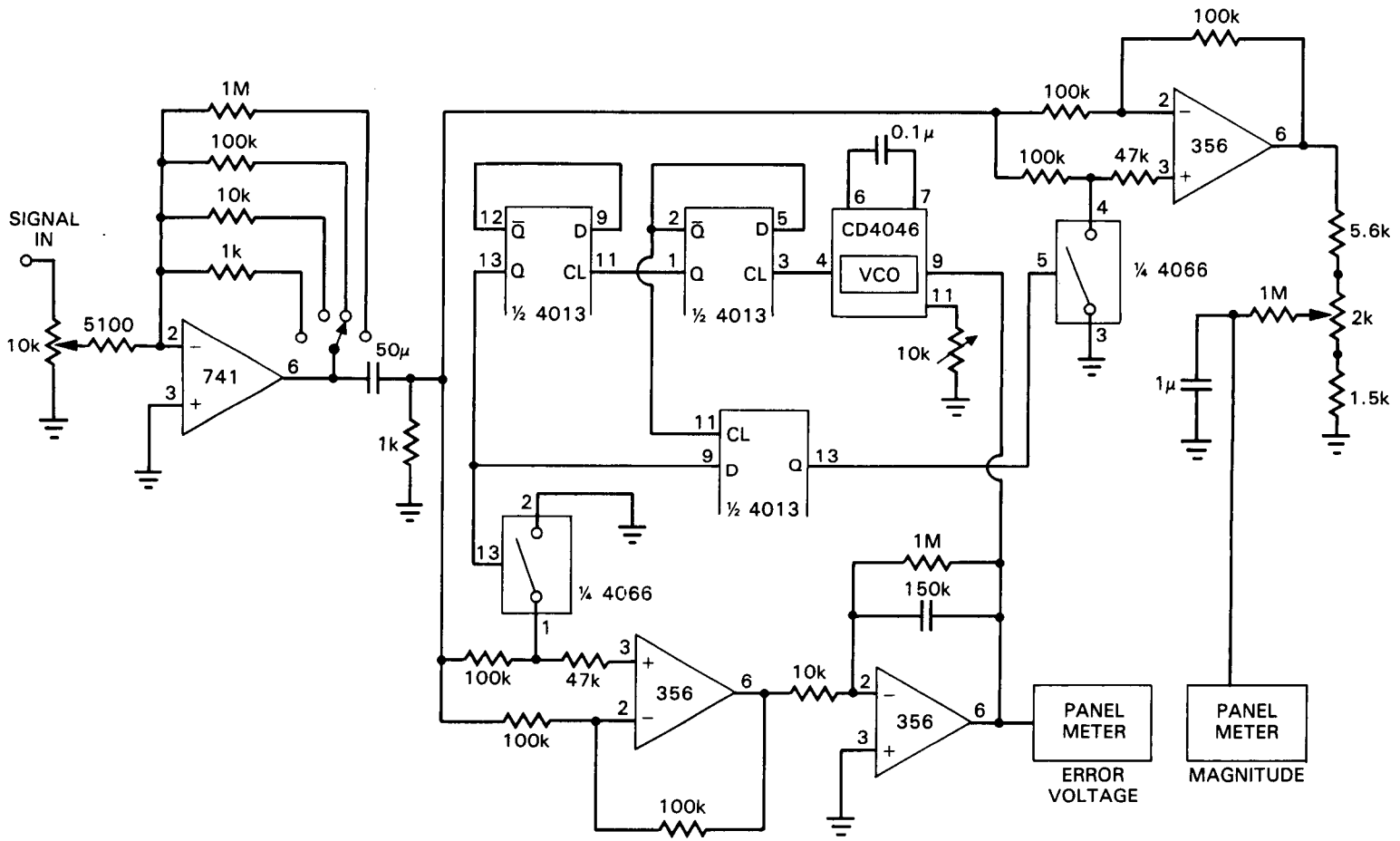

Figure 2-11. Circuit of ac field meter receiver, showing measurement and "reference" sections

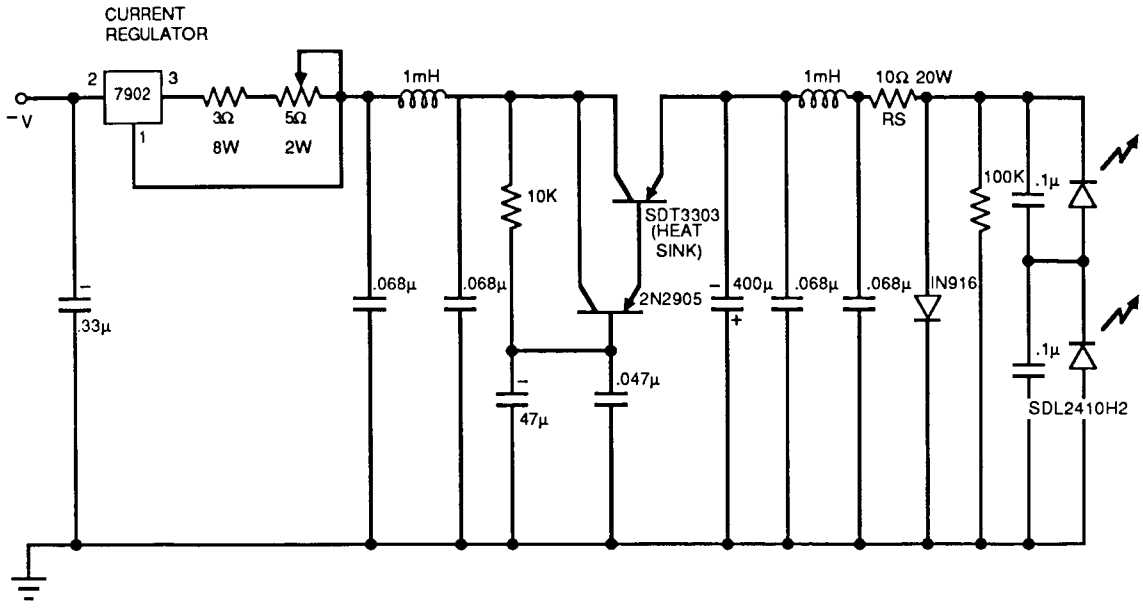

Figure 2-12. Laser power supply

2.3. Test results

2.3.1. Calibration

Because the ac field meter is spherical, the distortion it causes in an otherwise uniform field can be calculated. This results in the possibility of a calibration from first principles, rather than an experimental calibration. Wilhelmy (1973) examined the distribution of charge around a conducting sphere in a time-varying homogeneous field. His work was aimed at a probe that could provide information on the x-, y-, and z-components of the field. Of more direct application to our situation, Deno and Zaffanella (1975) derived the expression

$$i = j\omega 3\pi r^2 \epsilon_o E \qquad (2\text{-}1)$$

where i is the current between two hemispheres whose polar axis is aligned with a field of magnitude E. The radius of the sphere is r, ϵ_o is the permittivity of free space, and ω the angular frequency. To obtain a calibration from first principles, all that is needed is to inject a known current at power frequency and adjust the gain of the receiver until the display reads the value of field corresponding to the input current.

A high quality calibrated signal source was used to generate power frequency current. The signal source was terminated with a 50 Ω load, and capacitors were used to feed a small amount of current to each of the electrodes in the probe. The necessary adjustment was then made in the receiver. The arrangement is shown in Figure 2-13.

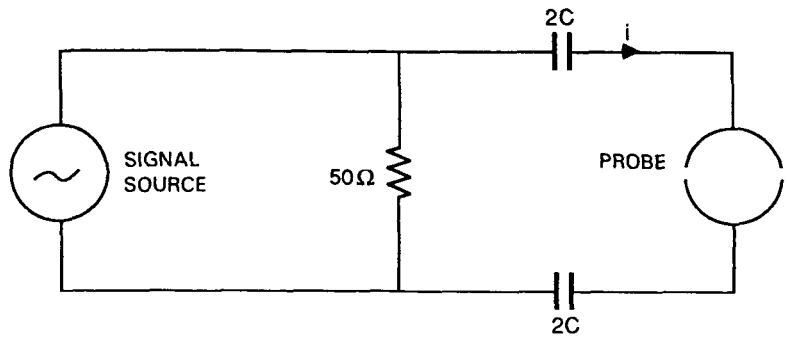

Figure 2-13. Calibration arrangement for ac meter

The injected current, i, in Figure 2-13 is given by

$$i = V_{app} \times \omega C \tag{2-2}$$

where C is the value of the two capacitors in series, and V_{app} the applied voltage. The current can be eliminated between equations 2-1 and 2-2:

$$E = \frac{V_{app}\, C}{r^2} \times \frac{1}{3\pi\epsilon_o} \tag{2-3}$$

With the values used, equation 2-3 gives that $E = V_{app} \times 63.308$. If V_{app} is measured in mV, the field is expressed in V/m.

2.3.1.1. Sources of uncertainty in calibration

When it was inserted into an electric field, the probe measured a value that seemed to be a few percent different from the one calculated for that field. The discrepancy was eventually traced to distortion of the waveform of the ac source energizing the test cage. Once this distortion had been removed, the probe seemed to measure very accurately the value of the field.

This high degree of accuracy should not be surprising. Most of the sources of error in the receiver are removed by the method of calibration. Sources of uncertainty in the calibration include uncertainty in the value of injected current, errors in the range-changing resistors in the receiver, and digitization error.

With a 3½ digit display, the digitization error can normally be held below one percent. On the range for which calibration was done, the predominant uncertainty is in the current fed into the probe. The measurement uncertainty is the sum of that due to the current, and that due to the range change resistors. One percent resistors are used in the range-changing switch in the prototype receiver.

As mentioned above, the current injection was from a high quality signal generator terminated in 50 Ω. Series capacitors from the 50 Ω termination to the probe provided essentially a current source. It is difficult to measure

such a small current; however, the current is eliminated in the procedure we used. Instead, it is necessary to know the voltage across the 50 Ω terminating resistor and the value of the series capacitors.

While the voltage across the resistor could be estimated from the signal generator readings, it can also be measured as an AC voltage to an accuracy of better than 0.5%. Since the injected current is given by this voltage divided by the impedance of the series capacitors, uncertainty in the value of the capacitors adds to the uncertainty in the measurement of voltage to produce the total uncertainty in the current. In our calibration, 10% capacitors were used. This 10% would become the dominant uncertainty in the calibration procedure. To reduce this uncertainty to an acceptable value, the capacitors were measured. The two 1-nF capacitors measured 527 ±3 pF in series.

One remaining source of uncertainty is the precision with which equation 2-3 above fits the geometry of the probe. If the probe is not perfectly spherical and divided precisely in two, the equation cannot be expected to fit exactly.

The housing of the probe was fabricated from spun brass. It is expected that each hemisphere is identical to all the others (20 were made in a single batch). Consequently, no attempt was made to measure how precisely the sphere was bisected. Measurements of the hemispheres used in the probe indicate that the average radius is accurate to 0.2%, but that the probe is spherical only to within about 0.5%. An average weighted to enhance the contribution of the polar direction of the sphere was used for the radius in equation 2-3. It should be noted that the missing electrode area (necessary to accommodate entry of the fibers and the mounting paddle) is also very small, accounting for less than 1% the total surface area. Further, this surface area is at a part where, during operation, the induced charge is close to zero. No appreciable error is therefore expected from geometrical considerations of the probe.

Considering all the above uncertainties, the ac meter can be expected to have an uncertainty of about 2% on any range. The accuracy should be somewhat better on the range for which calibration was performed.

2.3.2. Laboratory tests

A number of tests were done to examine the performance of the ac field meter. Of particular interest was the question of the dynamic range, since the phase-locked loop detector was different from the one used in the dc meter; the stability of the probe, with its optical power supply was also of interest.

Later, the meter was taken to the National Bureau of Standards, in Gaithersburg, Maryland, for tests in a field known to greater accuracy than any we could establish at JPL.

2.3.2.1. Power supply

The output of the photodiode array is dependent on the level of illumination. Figure 2-14 shows the performance of one of the probe power supplies with and without the active stabilization. For these tests, a resistor was used to simulate the load of the hybrid integrated circuit. It can be seen that, with

the stabilizing diodes in use, the voltage at the output of the diode array is constant once the laser current reaches 220 mA, corresponding to an optical power of about 40 mW. The electrical power delivered at this point is 0.85 mW. This is adequate to supply the probe electronics, whose power consumption is only ≈ 1.7 mW. During normal operation, the laser would be driven at a slightly higher current than this threshold.

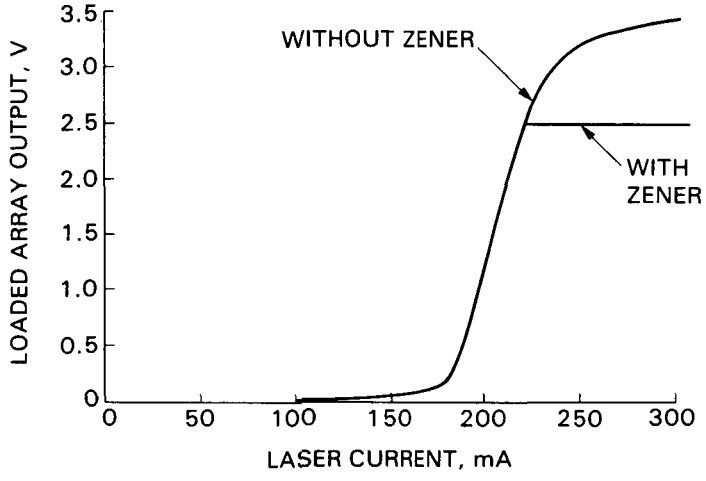

Figure 2-14. Performance of photodiode hybrid array

2.3.2.2. Dynamic range

The considerations that determine the dynamic range of the ac field meter are not the same as for the dc meter. In the case of the dc meter, the upper limit of signal-handling capability is defined by saturation of the signal chain and the lower limit by the level of synchronous noise in the system. In the ac meter, the upper limit is the same, but the lower limit may be set by other effects. For example, because the phase-locked loop used to synchronize the detector to the signal operates on the signal itself, and not a reference pulse, the loop can lose lock when the input signal is small or changes abruptly. This cannot happen in the dc meter.

Theoretically, the receiver can measure fields that produce voltages far below the level of random noise in the signal path. In practice, this limit has not been achievable because of the loss-of-lock problem. In addition, the 240 Hz oscillator used to produce the synchronous switching signals is subject to drift, and consequently there is a phase error when the field being measured is small.

Demodulator noise begins to mask the signal at about 50 V/m. Although lock can be maintained for signal levels 20 dB lower than this, a practical lower limit for the prototype meter is about 10 V/m, with an upper limit of 2 kV/cm. Figure 2-15 shows the output of the conditional inverter for inputs roughly corresponding to these extremes.

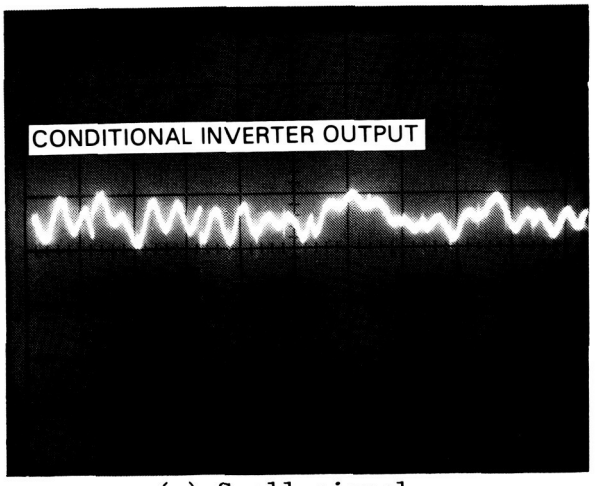

(a) Small signal

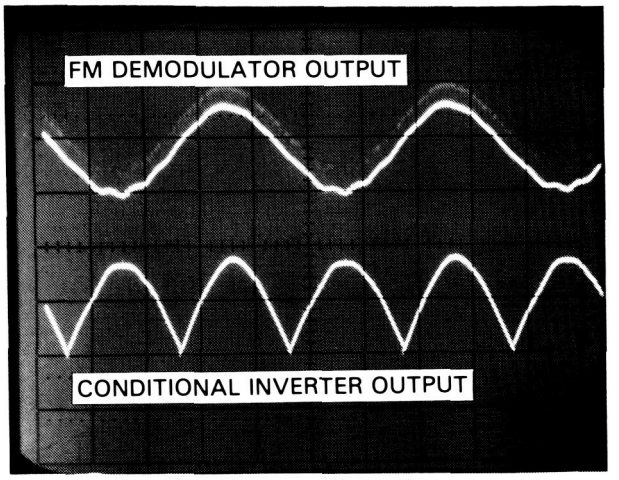

(b) Large Signal

Figure 2-15. Output of conditional inverter at small and large signals

The noise in the smaller signal, Figure 2-15a, is clearly evident. The signal here is about 20 dB below the noise, but the meter reads the field quite accurately. Trace discontinuities are switching operations. In Figure 2-15b, which represents a field of 2.5 kV/cm, the waveform at the conditional inverter (lower trace) appears relatively undistorted. However, the filtering removes some of the distortion present at the PLL FM detector output, as shown in the upper trace. The meter is showing some nonlinearity at this point.

2.3.3. Field tests

2.3.3.1. Tests at the National Bureau of Standards

On April 8, 1987, the ac field meter was taken to the National Bureau of Standards to examine the performance of the meter in a field known more accurately than any we could produce at JPL. The field was produced by applying a known voltage to an accurately measured parallel-plate arrangement. The field meter had been calibrated from first principles, as described in Section 2.3.1. The results of the tests are given in Table 2-1.

Although a 5-digit meter was used to measure the voltage applied to the plates, it was the opinion of Dr. Misakian, who conducted the tests, that the uncertainties in the system might total 0.5%.

The test results are shown graphically in Figure 2-16, which is drawn so as to exaggerate the differences between the calculated and measured values of the field. In the figure, horizontal dashed lines are drawn at ±0.5%. It can be seen that the measured values of the field are almost all within or close to the 0.5% lines.

The exception is the point corresponding to a field of 1.66 kV/m. It happens that this was the first point measured. There is a possibility that something in the receiver or probe electronics had not, at the time the reading was

taken, reached a stable operating condition. If allowance is made for the digitization uncertainty (vertical bars in Figure 2-16), the readings are within 1% ± 1 digit.

TABLE 2-1 SUMMARY OF NBS TEST DATA

Applied Voltage (kV)	Calculated Field[a] (kV/m)	Measured Field (kV/m)	Percentage Difference (%)
0.29934	1.661	1.643	-1.1
0.18943	1.0514	1.045	-0.61
0.26187	1.4534	1.444	-0.65
0.31801	1.765	1.753	-0.69
0.35544	1.9728	1.962	-0.55
0.35331	1.961	1.951	-0.51
0.35318	1.9602	1.97	0.5
0.44625	2.4768	2.48	0.13
0.53265	2.95637	2.96	0.12
0.63243	3.5101	3.52	0.2
0.7396	4.105	4.12	0.37

[a]based on a plate spacing of 0.1802 m

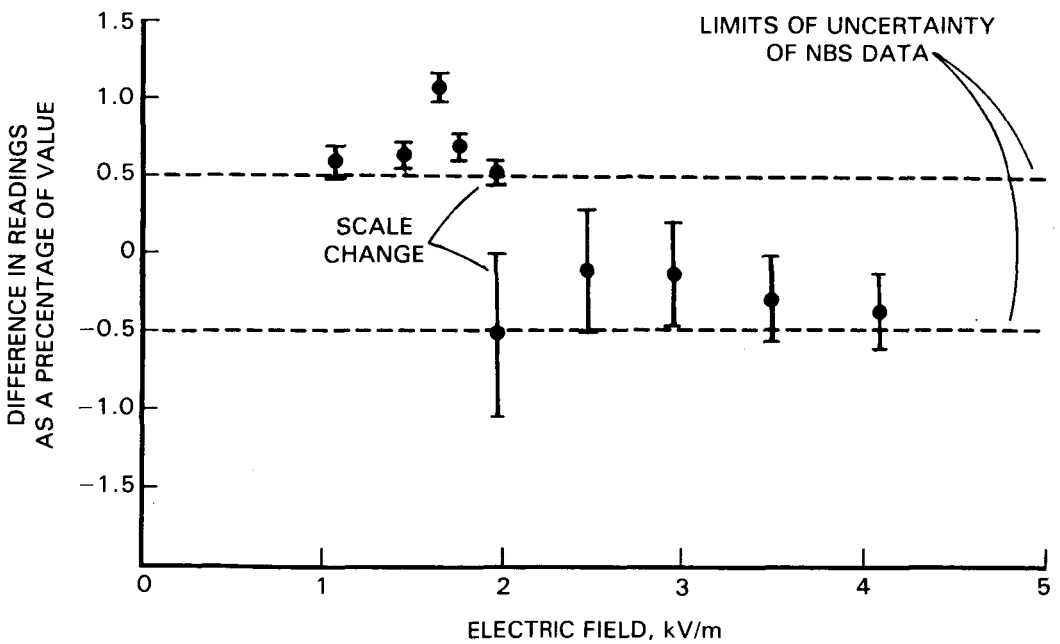

Figure 2-16. Differences between calculated and measured fields in NBS tests

The change in sign of the differences at a field value of 2 kV/m occurs because of a range change on the JPL meter. (The meter had been calibrated on the least sensitive of the two ranges used in the tests at NBS.) A trim resistor on each range would reduce this effect, but such a refinement is not thought worthwhile.

An indication of the linearity of the meter over a wide range may be obtained from Figure 2-17, which shows calibration data obtained synthetically.

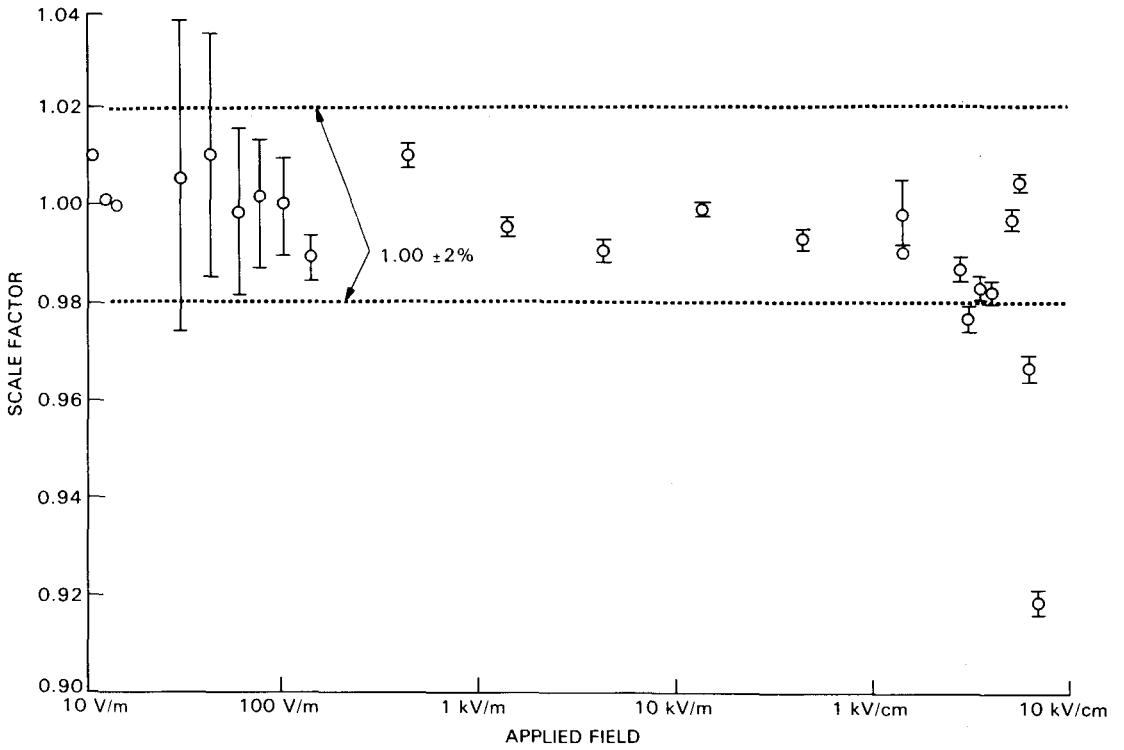

Figure 2-17. Scale factor of ac meter as a function of applied field

The vertical bars in Figure 2-17 represent the effect of changing the last digit of the display. The actual measurement uncertainty is somewhat larger.

Field values below 10 V/m can be obtained, but are of little real use. The decrease in sensitivity above about 6 kV/cm is due to saturation of the data channel, in particular the probe VCO. Between these two extremes, the linearity is excellent.

The dotted lines represent 2% of the actual value. Most of the data lie within 2% of the true value. Knowledge of the value of a field to an accuracy of better than 2% is sufficient for all practical purposes.

PART 3

CONCLUSIONS

3. CONCLUSIONS

In a way the title "Conclusions" is misleading. The work on the ac and dc field meters is not, at the time of writing, concluded. However, prototype ac and dc free-body electric field meters have been developed, and this is an appropriate time to review what has been accomplished and what remains to be done.

3.1. Review

The most important accomplishment of this effort has been the development of a small, portable, free-body dc electric field meter. This meter puts the space-potential measurement of the field due to dc lines on an equal footing with the same measurement for ac lines. For the first time, the measurement of dc fields above the surface of the ground is possible even in the presence of a distorting object.

This is an important development because models developed for alternating fields are not necessarily valid for dc fields. Experimentally measured fields can provide data to refine these models. For example, many materials which are considered to be good insulators when stressed with alternating voltage are not good dc insulators. A vehicle parked under an ac line may have a considerable induced voltage. The same vehicle under a dc line will be at ground potential: the tires are no longer good insulators.

Space charge provides a further example of the difference between ac and dc fields. Only in a dc field does space charge accumulate on insulating surfaces. This accumulated charge modifies the external field, but only if the field is dc. This effect is most dramatically demonstrated by the way the hair of a person under a dc line stands up, away from the head. No such effect is observed under an ac line.

The new information that can be provided by the dc field meter should lead to better models of the behavior of conductors, insulators and space charge in direct fields. A better understanding of the interactions of dc fields and the things that inhabit them should result.

The measurement of ac fields in air has also been improved by the development of a very small spherical field meter.

The small size of the ac field meter probe (1 cm radius) is made possible only by the method used to energize the electronics it contains. Optical power, furnished by a pair of solid-state lasers, is converted to electrical form by gallium arsenide diode arrays. This method of powering the probe occupies less volume than even the smallest batteries, and has the further advantage of requiring no power switch in the probe. This technique could find application in other power system measurements.

The dc and ac electric field meters are shown in Figures 3-1 and 3-2.

Figure 3-1. Complete systems for dc and ac field meters

Neither the ac nor the dc field meter have any controls on the sensing probe. This means that during operation the meter can be moved from a region of low field to a region of high field without the need to approach the probe. Beside being very convenient, this aspect of the design increases operator safety.

Another advantage shared by the ac and dc field meter is that, unlike most of their predecessors, they can both be connected to data acquisition systems. Most space-potential field meters built to date have not had this capability.

To go along with these new field meters, a novel photographic technique has been developed for the collection of data in two dimensions. By using cameras with linked shutters, the position of the sensing probe and the reading of the field meter at the same instant can be captured on film. A computer program has been written to facilitate the transfer of the probe position data and the field readings to the familiar field map form. A convention that the length of the line representing the field vector at any measured point is inversely proportional to the strength of the field generates a map which greatly resembles a conventional field plot. The use of accurately drawn maps like

this should enable the accurate estimation of field intensities in regions where the distortion caused by the presence of the probe is unacceptably large (generally this means closer than a few probe diameters to a conducting surface). This approach should increase the range of applications of both the ac and the dc meter.

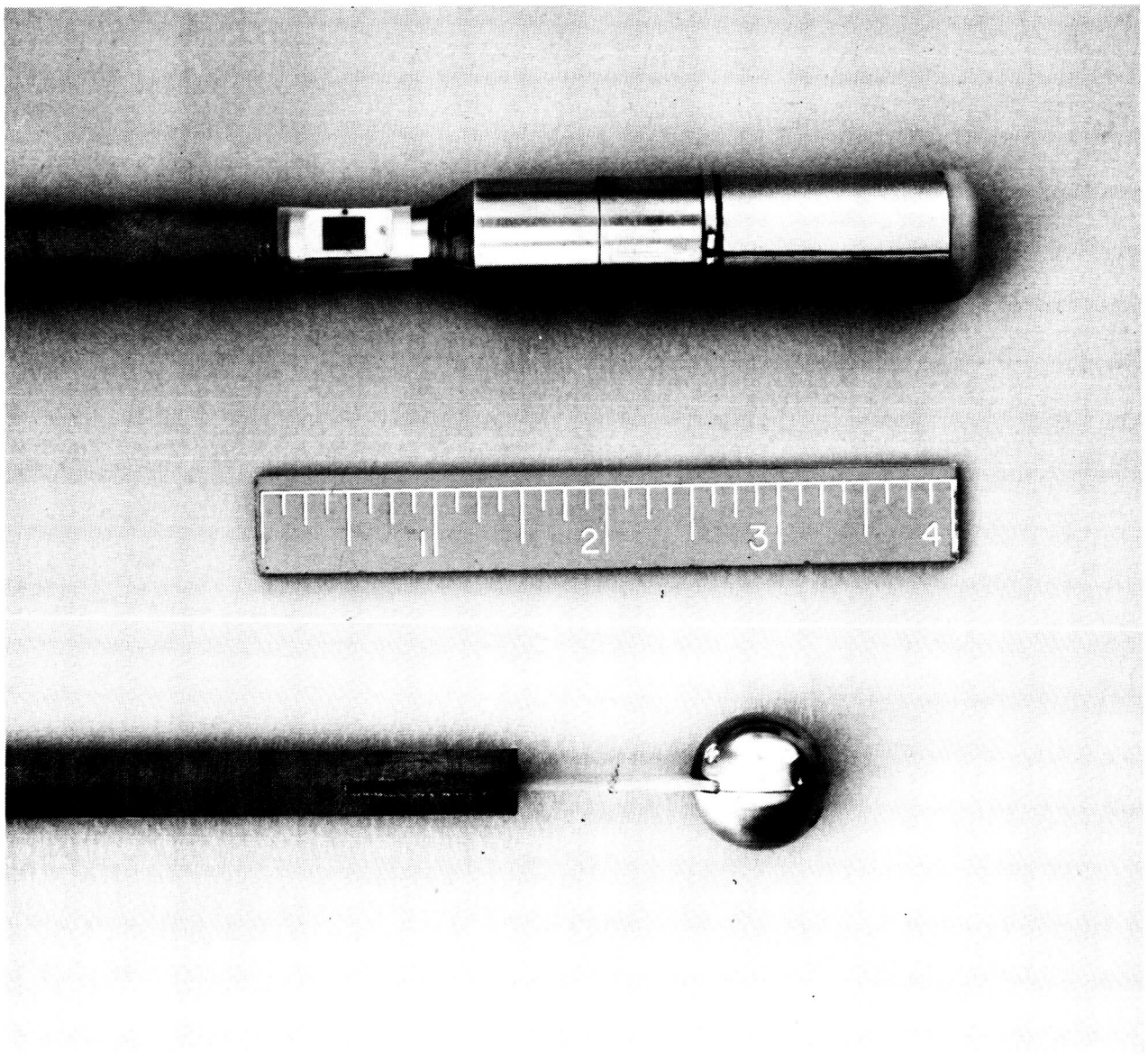

Figure 3-2. Probes of dc and ac field meters

3.2. Future Developments

At the time of this writing, three developments are being discussed for these field meters. First, it may be noted that the ac field meter reads only the magnitude of the electric field. Its direction must be deduced from the

position of the handle holding the sensing probe. It might be more convenient if the receiver were to display the field components in the x-,y-, and z directions. Such a development is, in principle, possible. It is not clear, however, that the rework of the electronics that would be entailed is justified.

Second, it should be a fairly straightforward matter to convert both the ac and the dc electric field meter into meters of magnetic field. If the electrode structure of each meter is replaced with a suitable search coil, the same probe electronics and receiver electronics could, in principle at least, display magnetic fields. This modification is planned for 1987.

Third, it would greatly facilitate the drawing of electric field maps if a computer program were available to draw the field and equipotential lines according to the rules of the curvilinear square method. The boundary conditions would be applied and the measured data would appear as constraints in the drawing process. This method would have advantages in cases where conditions at the boundary of the measured region were not perfectly understood, for example, in the case of a contaminated insulator. Such a computer program is receiving consideration at this time.

APPENDIX A

THE JPL ELECTRIC FIELD TEST CAGE

APPENDIX A. THE JPL ELECTRIC FIELD TEST CAGE

An electric field cage capable of producing uniform electric field with space charge was constructed at JPL for use with the electric field probes. The cage, shown in Figure A-1, is a "parallel plate" type, measuring 6 ft (1.8 m) on a side. The cage is modeled after the NBS field cage.

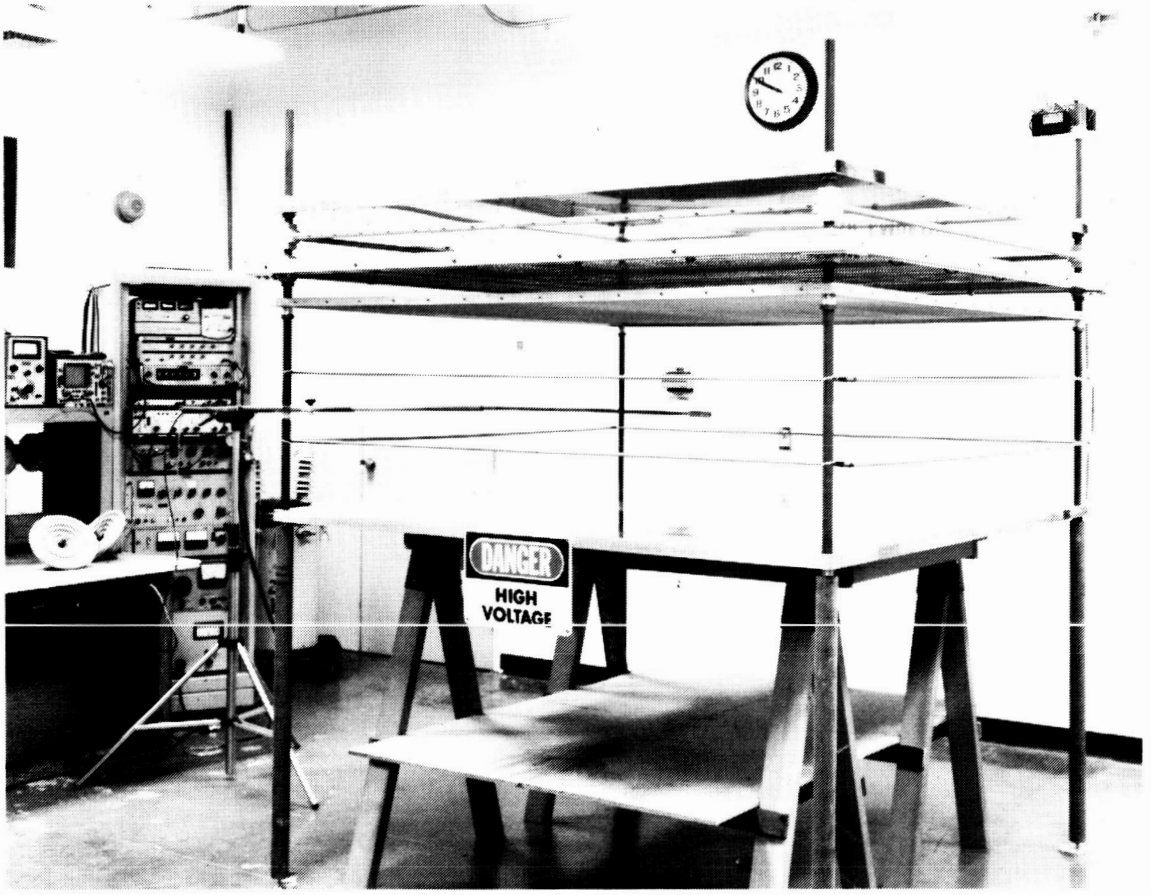

Figure A-1. JPL electric field test cage

A schematic view of the apparatus is shown in Figure A-2. Elements 1 and 2 are the "parallel plates" used to produce the electric field. The bottom plate, made from 1/4 inch aluminum sheet, is reinforced with cross-braces and saw horses from beneath to guarantee a uniformly flat surface. The upper "plate" is a tightly stretched aluminum screen which permits the entry of ions into the field area from the generator above. The vertical dimension of the plate spacing is adjustable, but in practice it is kept to less than half the side dimension. Takuma and his colleagues (1985) showed that this keeps the field value at the center of the cage within 1% of the uniform field value given by V/d even without guard rings.

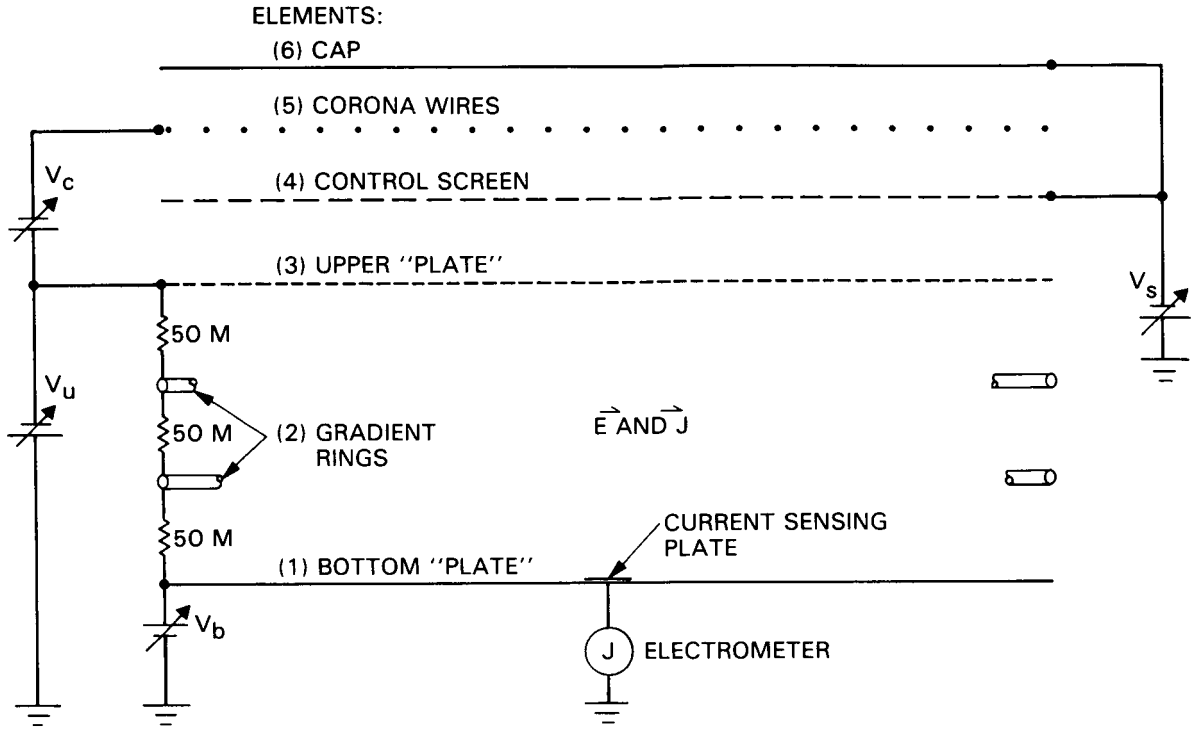

Figure A-2. Diagram of test cage

Field uniformity is further improved through the use of two gradient rings (element 3) located at the perimeter of the cage, evenly spaced between the two plates. The rings, made from 3/8 inch tubing, are connected to the plates through a resistive voltage divider network, charging them to the voltage they would have in a uniform field in the absence of space charge. We have not studied the effect on field uniformity of the constant voltage on the guard rings even when the space charge is present.

Space charge within the cage is produced and controlled by elements 4, 5 and 6, located above the plates. Twenty-four 0.006 in (0.15 mm) diameter corona wires (element 5) generate ions which are attracted to the aluminum cap (element 6) and to the control screen (element 4), made from 0.030 in (0.76 mm) diameter wire. Many of the ions pass through the control screen's 0.4 in (10 mm) square openings and travel downward to the upper "plate". Ions which make their way through this plate continue downward to the bottom plate, constituting the ion current within the cage.

The current density near the bottom plate is measured using a very thin movable sensing plate, made from foil and mica, connected to an electrometer.

APPENDIX B

SOLUTION OF THE TRANSIENT FIELD PROBLEM

IN THE TEST CAGE WITH ION CURRENT

APPENDIX B. SOLUTION OF THE TRANSIENT FIELD PROBLEM IN THE TEST CAGE WITH ION CURRENT

B.1 Transient Field

Field measurements in the test cage showed a transient overshoot as the ion source was energized. An example is shown in Figure A.1.

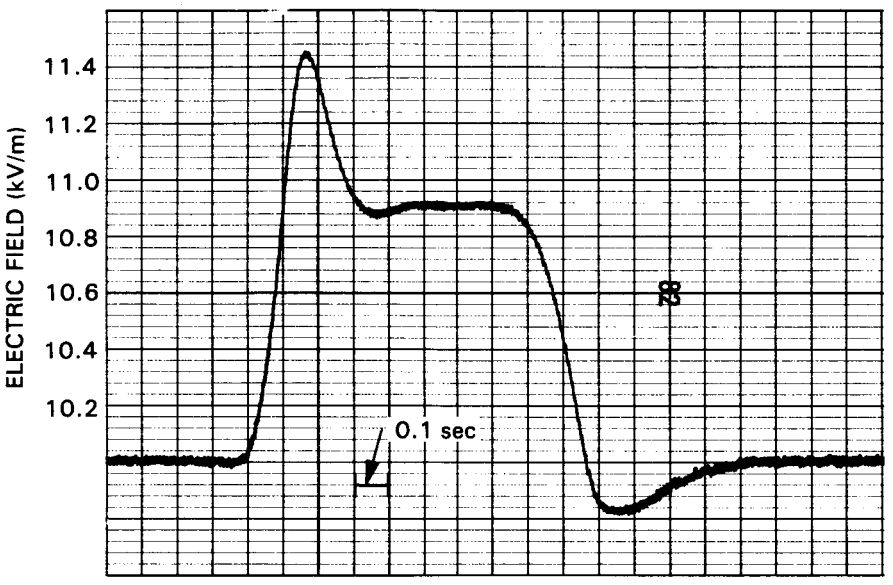

Figure B-1. Example of overshoot of measured field following ion source energization

It was reasoned that the overshoot, which persisted for a good fraction of a second, was a genuine result, rather than an artifact of the instrumentation. It seemed reasonable to suppose that the ion current resulted in an increase in the gradient in one part of the cage (and a decrease in another) which eventually disappeared as a steady state was approached. In particular, it was thought that when only part of the cage contained ions, the ionized part of the cage would have less voltage across it, and the non-ionized part more, than when the entire cage was devoid of ions, or when the ions completely filled the cage. It will be shown that these initial ideas were not quite correct.

To analyze this problem, the cage can be divided into two regions, above and below a moving boundary. Above the boundary, ions are present, and the distribution of voltage and gradient can be described by Poisson's equation. Below the boundary there are no ions, and the conditions for Laplace's equation exist.

Figure B-2 shows the cage with the ionized region part way down. The effect of diffusion is neglected. It is assumed that the front edge of the ionized region remains sharply defined as it moves into the cage.

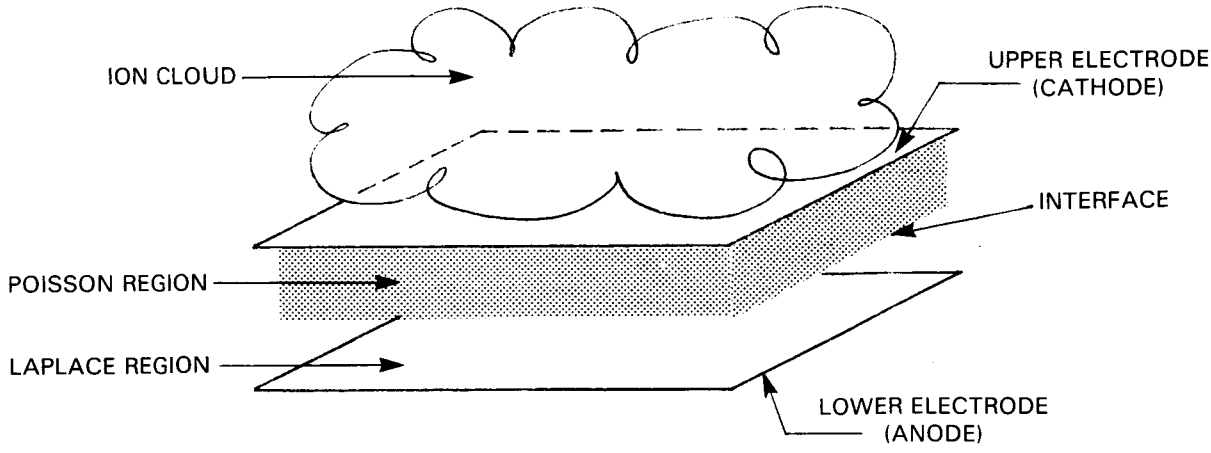

Figure B-2. Test cage with ionized region

In the Poisson region above the boundary, Poisson's law in rectangular coordinates

$$\nabla^2 V = \frac{\partial^2 V}{\partial x^2} + \frac{\partial^2 V}{\partial y^2} + \frac{\partial^2 V}{\partial z^2} = \frac{-\rho}{\epsilon} \qquad \text{(B-1)}$$

can usually be reduced to the complete differential equation

$$\nabla^2 V = \frac{d^2 V}{dz^2} = \frac{-\rho}{\epsilon} \qquad \text{(B-2)}$$

for the one dimensional case, in view of the x and y symmetry. Here V is the potential, ρ the space charge density and ϵ the permittivity of free space. The cloud of charge is assumed to be moving in the -z direction. Until the steady state is achieved, the equation should in fact show the variables also as a function of time:

$$\frac{\partial^2 V(z,t)}{\partial z^2} = - \frac{\rho(z,t)}{\epsilon} \qquad \text{(B-3)}$$

In addition to Poisson's equation, B-3, there are constitutive relationships describing the behavior of the charge. The current in the cage is given by the sum of two components, the conduction current, which exists only in the Poisson

region and the displacement current, which is necessary to avoid violation of Kirchoff's law at the boundary. Thus

$$J_{total} = J_{cond} + J_{displ} \tag{B-4}$$

where J_{cond}, the conduction current density, is given by the product of charge density and carrier velocity

$$J_{cond}(z,t) = \rho(z,t)v(z,t) \tag{B-5}$$

and the displacement current, J_{displ}, is given by the time rate of change of the electric field

$$J_{displ}(z,t) = \epsilon \frac{\partial E(z,t)}{\partial t}$$

$$= \epsilon \frac{\partial^2 V(z,t)}{\partial z\, \partial t} \tag{B-6}$$

The total current is therefore given by

$$J(z,t) = \rho(z,t)\, v(z,t) + \epsilon \frac{\partial^2 V(z,t)}{\partial z\, \partial t} \tag{B-7}$$

Note that the charge carriers move with a velocity v given by the magnitude of the field E:

$$v(z,t) = \mu E(z,t) = -\mu \frac{\partial V(z,t)}{\partial z} \tag{B-8}$$

where μ is the parameter termed mobility, assumed constant. (This expression is equivalent to the statement that energy is not conserved, and it may be derived from energy considerations of a nonconservative system.)

Therefore,

$$J(z,t) = \epsilon \frac{\partial^2 V(z,t)}{\partial z\, \partial t} - \rho(z,t)\, \mu \frac{\partial V(z,t)}{\partial z} \tag{B-9}$$

This can be rearranged to yield an expression for $\rho(z,t)$:

$$\rho(z,t) = \left[\epsilon \frac{\partial^2 V(z,t)}{\partial z\, \partial t} - J(z,t) \right] \Big/ \mu \frac{\partial V(z,t)}{\partial z} \qquad \text{(B-10)}$$

Substitution of this value for $\rho(z,t)$ into equation B-3 (Poisson's equation) yields

$$\epsilon\mu \left[\frac{\partial V(z,t)}{\partial z} \right] \left[\frac{\partial^2 V(z,t)}{\partial z^2} \right] + \epsilon \frac{\partial^2 V(z,t)}{\partial z\, \partial t} = J(z,t) \qquad \text{(B-11)}$$

A number of workers have investigated the question of gaseous conduction[1]. It transpires that equation B-11 has other applications : we are indebted to Professor W.J. Gajda of the University of Missouri at Rolla for pointing out the similarity of our problem to the problem of current injection in solids.

The solution to the problem of SCL injection in solids is given by Lampert and Mark (1970)[2]. There it is shown that the injection current increases to a peak value about 21% above the final steady state value by the time the front edge of the charge reaches the anode. From this value, there is a decrease in current, with a slight undershoot. The time taken for the leading edge of the charge to reach the anode is about 78% of the time calculated for the transit of a single ion in an otherwise Laplace region.

The current waveform after Lampert and Mark is shown in Figure B-3, where it is compared with the field measured by the probe in the JPL test cage. The current curve is normalized; time and field scales are given for the cage field results. In the examples shown, the anode-cathode spacing was 60 cm, and the applied voltage was -6 kV.

---

[1]Zahn, Tsang and Pao (1974) present an analysis of unipolar ion conduction which includes a transient similar to the one we observed. Their paper presents its results chiefly in the form of computer-generated graphs, although much of the analysis is closed form. The work is extended by Zahn and Pao (1975) and by Zahn, Pao and Tsang (1976). A model for bipolar conduction is developed by Zahn (1975). The problem is analyzed for spherical and cylindrical geometries with unipolar conduction by Zahn (1976). Crow, Auer and Allen (1975) discuss the expansion of a plasma into a vacuum, but the plasma is collisionless.

[2]The question of the transient in solids is also examined by Many and Rakavy (1962) for SCL currents both with and without trapping.

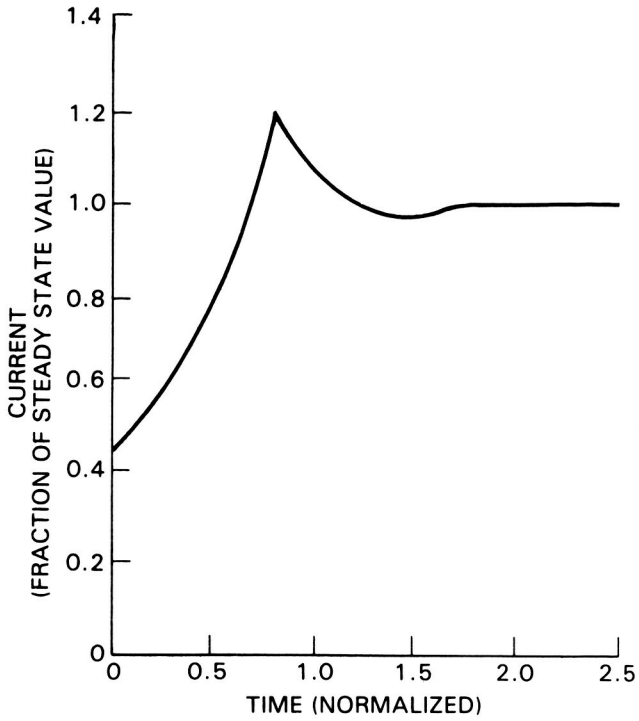

(a) Current transient
(after Lampert and Mark)

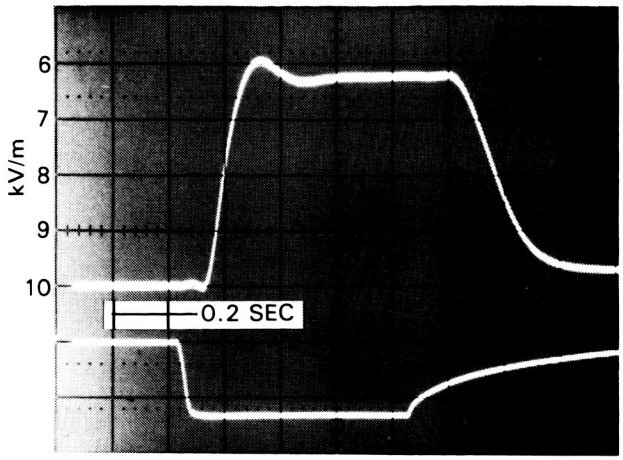

(b) Field near cathode

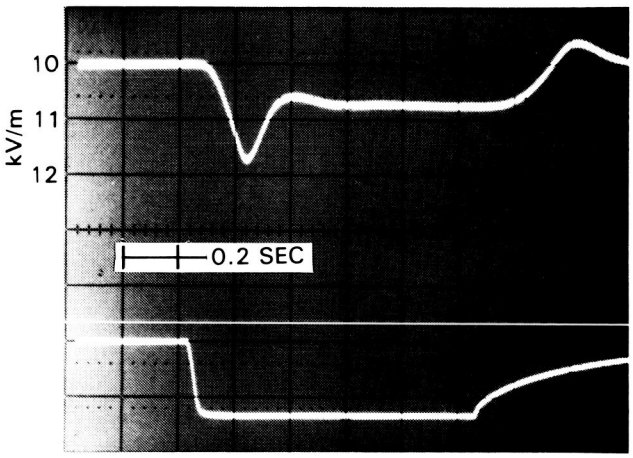

(c) Field at center of cage

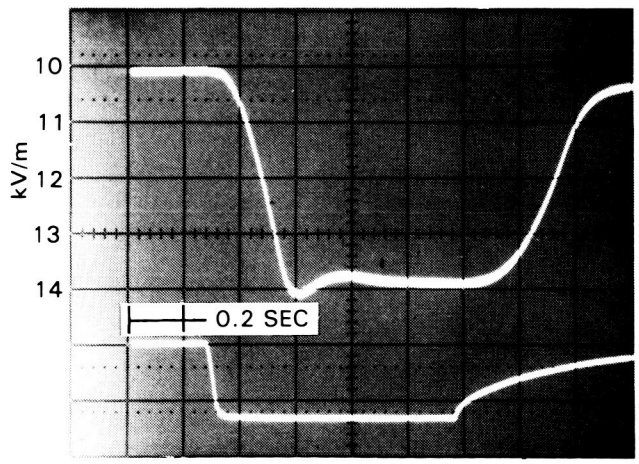

(d) Field near anode

Figure B-3. Field transient in test cage

The cage results show that, as expected, the field near the cathode decreases when the ion source is energized. The field at the anode increases. The cage center is near the point at which the field changes little (in the final steady state) as a result of the ion current. Nevertheless, the transient is still clearly visible.

The lower trace in the oscilloscope pictures (Figure B-3; b, c and d) is a marker to show when the ion current source was energized. In each case, there seems to be a small delay between the energizing of the ion source, and the appearance of the transient in the field. This may be due to the transit time of the ions from their true source to the cathode. The delay is no different whether the probe is near the anode or the cathode. The calculated transit time for an isolated ion in the cage under these conditions is 0.4 s, (assuming an ion mobility of 1.5×10^{-4} m^2/V s) so that the current peak should be reached after about 0.31 s. This is in good agreement with the measured results.

It is clear that most (if not all) of the transient increase in the field can be attributed to the increase in the current. The rounding of the field waveform is due in part to diffusion effects, and in part to the filtering of the output signal from the field meter. Apart from this, the comparison is clearly very good.

B.2 Space Charge Limited Current

The question arises, is there a way to calculate the value of the steady-state current in the cage, to "denormalize" the curve given by Lampert and Mark? If so, the calibration of the field meter would no longer rely on the measurement of current in order to know the field in the cage when there was ion current.

The steady-state problem is soluble in closed form. By taking only the steady-state part of Equation B-11, we obtain

$$\epsilon\mu \left[\frac{dV(z)}{dz} \right] \left[\frac{d^2V(z)}{dz^2} \right] = J(z) \qquad \text{(B-12)}$$

Simplifying,

$$\epsilon\mu \, E \frac{dE}{dz} = - J \qquad \text{(B-12)}$$

so that

$$\frac{dE}{dz} = \frac{-J}{\mu\epsilon E}, \qquad \text{(B-13)}$$

integration gives that

$$\int E \, dE = \int \frac{-J}{\mu\epsilon} \, dz, \qquad \text{(B-14)}$$

or

$$E^2 = \frac{-2Jz}{\mu\epsilon} + C \tag{B-15}$$

where C is a constant of integration.
Therefore

$$E = \pm \left(C - \frac{2Jz}{\mu\epsilon} \right)^{1/2} \tag{B-16}$$

(It will be seen later that the negative root is required for a solution.)

This can be integrated by means of a substitution. First, we simplify by letting

$$a = \frac{2J}{\mu\epsilon} \tag{B-17}$$

so that Equation B-16 becomes

$$E = \pm (C - az)^{1/2} \tag{B-18}$$

Next, we let

$$F^2 = C - az \tag{B-19}$$

so that

$$2F\, dF = -a\, dz \tag{B-20}$$

and

$$V = -\int E\, dz = -\int \pm (C - az)^{1/2}\, dz \tag{B-21}$$

At this point it is clear that the negative root must be used if V is to be positive. Thus

$$V = \int F \frac{2F\, dF}{a} \tag{B-22}$$

$$= \frac{2F^3}{3a} + K$$

$$= \frac{2}{3a} (C - az)^{3/2} + K$$

$$= \frac{\mu\epsilon}{3J}\left(C - \frac{2J}{\mu\epsilon} z\right)^{3/2} + K \qquad \text{(B-23)}$$

where K is another constant of integration.

K can be evaluated directly. Since we have V=0 when z=0, it follows from B-23 that

$$K = -\frac{\mu\epsilon}{3J} C^{3/2} \qquad \text{(B-24)}$$

whence

$$V = \frac{\mu\epsilon}{3J}\left\{\left(C - \frac{2J}{\mu\epsilon} z\right)^{3/2} - C^{3/2}\right\} \qquad \text{(B-25)}$$

It is an experimentally observed fact that the field decreases near the source of the ions, and is zero at the boundary in the space-charge-limited case. (This zero field is equivalent to the definition of space charge limiting.) This being the case, E=0 at z=h, so that the value of the constant of integration C can be found directly from Equation B-16:

$$C = -\frac{2J_{SCL}\, h}{\mu\epsilon} \qquad \text{(B-26)}$$

(J is negative in this coordinate system.)

We can also use equation B-25 for voltage to apply a boundary condition that at z=h, $V=V_h$. In the SCL case the term inside the parentheses (which represents the gradient) vanishes, so that

$$V_h = -\frac{\mu\epsilon}{3J_{SCL}} C^{3/2} \qquad \text{(B-27)}$$

whence

$$C = -\left(\frac{3J_{SCL}\, V_h}{\mu\epsilon}\right)^{2/3} \qquad \text{(B-28)}$$

The two values of C, in B-26 and B-28, must be the same, i.e.

$$\frac{2J_{SCL}\, h}{\mu\epsilon} = \left(\frac{3J_{SCL}\, V_h}{\mu\epsilon}\right)^{2/3} \qquad \text{(B-29)}$$

$$\left(\frac{2J_{SCL}\, h}{\mu\epsilon} \right)^3 = \left(\frac{3J_{SCL}\, V_h}{\mu\epsilon} \right)^2 \qquad \text{(B-30)}$$

$$J_{SCL} = \frac{3^2\, V_h^{\,2}\, \mu\epsilon}{2^3\, h^3} \qquad \text{(B-31)}$$

We therefore arrive at the interesting result that the value of current at which space charge limiting occurs can be calculated in a fairly straightforward way once the size of the cage and the applied voltage are known.

For example, during the tests at NBS we had

$V = 1006$ V

$\mu = 1.5 \times 10^{-4}$ m^2/V sec

$\epsilon = 8.854 \times 10^{-12}$ F/m

$h = 0.17$ m

from which a value for the SCL current can be found. The result is approximately 307 nA. This compares well with the current actually observed, 303 nA.

Equation B-31 can serve as a simple way to measure the mobility of the charge carriers. Indeed, it is likely that the NBS value for the ion mobility used in the tests in Gaithersburg was obtained by recasting equation B-31 to yield a value for μ.

B.3 Gradient in a Poisson field

So far, we have considered the voltage and current conditions in the cage. The equations developed can also be used to find the gradient as a function of height, assuming space-charge-limited conditions. Thus, from Equation B-16 and assuming $J = J_{SCL}$:

$$E = \pm \left(C - \frac{2Jz}{\mu\epsilon} \right)^{1/2} \qquad \text{(B-32)}$$

From B-26 we have

$$C = -\frac{2Jh}{\mu\epsilon} \qquad \text{(B-33)}$$

so that

$$E = \pm \left(\frac{2Jh}{\mu\epsilon} - \frac{2Jz}{\mu\epsilon} \right)^{1/2} \tag{B-34}$$

$$= \pm \left(\frac{2J}{\mu\epsilon} \right)^{1/2} (h - z)^{1/2} \tag{B-35}$$

It is possible to eliminate J, since Equation B-31 gives that

$$J_{SCL} = \frac{3^2 \, V_h^{\,2} \, \mu\epsilon}{2^3 \, h^3}$$

whence

$$E(z) = \pm \left(\frac{2 \times 3^2 V_h^2}{2^3 \, h^3} \right)^{1/2} (h - z)^{1/2} \tag{B-36}$$

$$= - \frac{3}{2} \frac{V_h}{h} \left(\frac{h - z}{h} \right)^{1/2} \tag{B-37}$$

so that the Poisson field can be expressed in terms of the Laplace value V_h/h in the form

$$E_{Poisson}(z) = \frac{3}{2} H(z) \, E_{Laplace} \tag{B-38}$$

where H is a normalized height factor $\sqrt{(h - z)/h}$.

Equation B-38 shows that the maximum field intensification due to ion current in a planar cage is 50%, and as expected the field drops to zero at the cathode.

APPENDIX C

ERROR SOURCES AND SOLUTIONS

APPENDIX C. ERROR SOURCES AND SOLUTIONS

This appendix will discuss the sources of error that arise in a measurement system of the kind used in the dc field meter. The design of the meter system, and how the effects of these sources of error were dealt with in the design are described in Section C.1. Section C.2 deals with the sources of error that are attributable to physical effects outside the meter.

Figure C-1 shows a generalized measurement system of the type used in the dc field meter. A number of sources of error are discussed with reference to this figure.

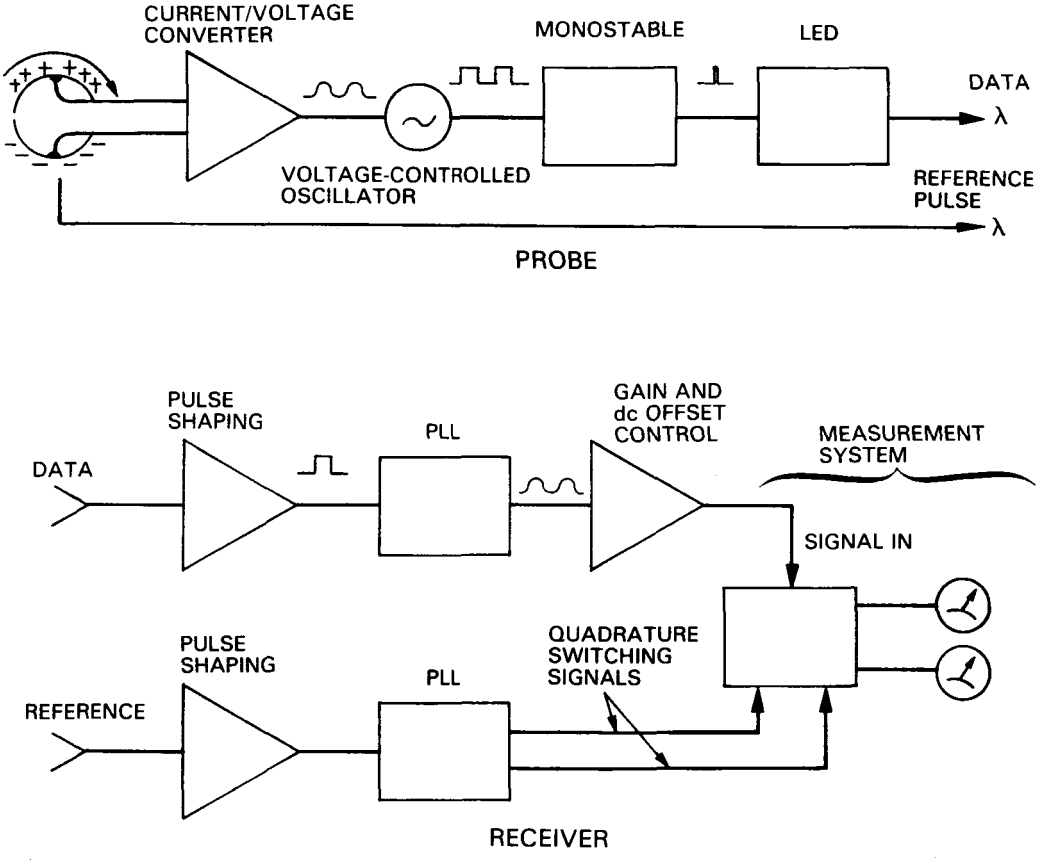

Figure C-1. Generalized measurement system

C.1. Measurement System

The electric field to which the probe is exposed induces a charge on the surface of the probe. The charge is proportional to the magnitude of the field. Suppose that the probe is in a uniform field $E=E_x+E_y$, as shown in Figure C-2.

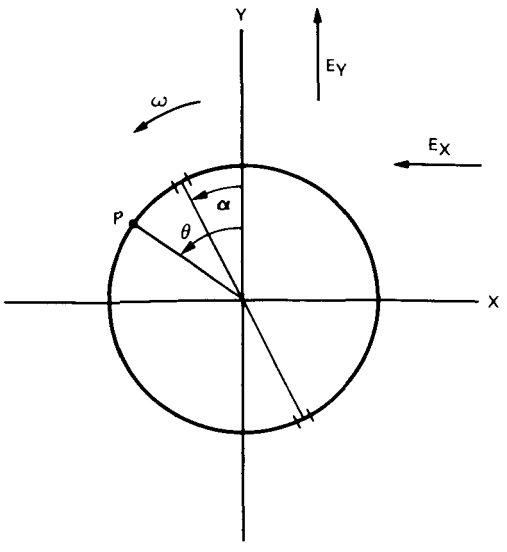

Figure C-2. Probe in electric field

In the figure, P represents a point on the cylindrical probe surface, having a location specified by θ measured from the y axis. If we assume that the electrodes are part of an infinite cylinder, the charge distribution around the probe is given by

$$\sigma(\theta) = 2r\epsilon_o(E_x \sin\theta + E_y \cos\theta) \tag{C-1}$$

per unit length, where r is the radius of the probe and ϵ_o is the permittivity of air. The charge on the electrodes is found by integrating over half the cylinder. For electrode a:

$$q_a = \int_{\alpha}^{\alpha+\pi} \sigma(\theta) d\theta \tag{C-2}$$

whence

$$q_a = -\, q_b = 4r\epsilon_o(E_x \cos\alpha - E_y \sin\alpha) \tag{C-3}$$

where α is the angle of the diameter separating the electrodes. With constant speed of rotation, $\alpha = \omega t$, so that

$$q_a(t) = 4r\epsilon_o(E_x \cos\omega t - E_y \sin\omega t) \tag{C-4}$$

As the electrodes rotate, the charge remains fixed with respect to the field, and so it passes from electrode to electrode by way of the input to the first stage of the amplifier. The current is given by $i=dq/dt$, or

$$i = -\, 4r\epsilon_o(E_x \omega \sin\omega t + E_y \omega \cos\omega t) \tag{C-5}$$

This stage converts the current at its input to an alternating voltage with magnitude proportional to the field-induced charge. The amplifier is configured as an integrator, so that the transfer function includes an effective $1/\omega$ term. The voltage modulates a voltage controlled oscillator (VCO). Narrow pulses are generated by the VCO and converted into optical pulses by a light emitting diode (LED). These pulses are injected into an optical fiber, and transmitted to the receiver portion of the system.

At the same time, an optical pulse is generated once each revolution, for angle reference purposes. In the original version the pulse was generated optically, and encoded onto the data pulses electronically. In that design, only one fiber was required between the sensor probe and the receiver, and the separation of the two pieces of information was electronic. In the newer probe, the pulse is generated by a small reflective spot on the edge of the rotating shell, which reflects light back into the fiber that illuminates it. This is a different fiber than the one that carries the data. A directional coupler separates the reflected energy from the illumination. This leads to a much simpler design for the probe electronics, which is important in terms of reducing the size and power consumption of the hybrid IC used in the probe.

The voltage signal that modulates the probe VCO is regenerated in the receiver by an identical IC configured as a phase locked loop (PLL) detector. It is functionally similar to an fm detector in a radio. The receiver is in fact recovering the modulation from an fm carrier which has been encoded as a low-duty-cycle pulse train for optical transmission.

Synchronous detection is used to obtain maximum dynamic range, and to ease the filtering requirements in the receiver. Compared to the usual synchronous detector, such as might be used in a radio receiver, this system has the advantage of a strong synchronizing pulse, with an amplitude that is independent of the signal being detected. This pulse is used to generate the switching signals for the synchronous detector by means of a second PLL. The switching signals for two quadrature components are generated. Thus, the outputs of the two detectors are, assuming "half-wave" detection:

$$\begin{aligned} E_p &= ki/\omega \qquad \phi < \omega t < \pi+\phi \\ E_p &= 0 \qquad \pi+\phi < \omega t < 2\pi+\phi \end{aligned} \tag{C-6}$$

and

$$\begin{aligned} E_q &= ki/\omega \qquad \phi+\pi/2 < \omega t < \phi+3\pi/2 \\ E_q &= 0 \qquad \phi+3\pi/2 < \omega t < \phi+5\pi/2 \end{aligned} \tag{C-7}$$

where the subscripts p and q stand for phase and quadrature components, k is the gain of the probe-receiver system (in terms of voltage at the detector for a given input current) and ϕ is the phase angle between the signal and the switching function.

In order to display the data, or to provide outputs suitable for data loggers, low-pass filtering is performed on the detected signals, as is standard practice in phase-locked detection. This effectively converts the output of the synchronous detectors into a dc voltage whose amplitude is proportional to the appropriate component, in-phase or quadrature, of the input.

$$D_p = -\frac{4rk\epsilon_o}{2\pi\omega}\int_{\phi}^{\phi+\pi}(E_x\omega\sin\omega t + E_y\omega\cos\omega t)d\omega t \qquad \text{(C-8)}$$

and

$$D_q = -\frac{4rk\epsilon_o}{2\pi\omega}\int_{\phi+\pi/2}^{\phi+3\pi/2}(E_x\omega\sin\omega t + E_y\omega\cos\omega t)d\omega t \qquad \text{(C-9)}$$

so that

$$D_p = -\frac{4rk\epsilon_o}{\pi}(E_x\cos\phi - E_y\sin\phi) \qquad \text{(C-10)}$$

and

$$D_q = \frac{4rk\epsilon_o}{\pi}(E_x\sin\phi + E_y\cos\phi) \qquad \text{(C-11)}$$

where D_p is the amplitude of the displayed signal for the in-phase component of the field, and D_q the corresponding signal for the quadrature component. During calibration, the angle ϕ, which is determined by the position of the reflecting spot on the rotating electrodes, is adjusted to zero, so that the two quadrature components of the output correspond to the two spatial components of the field.

During operation the range is changed (by adjusting the value of k in equations (C-10) and (C-11) above) to accommodate reductions in the incoming signal from a maximum of about a volt.

Having reviewed the data system used in the probe and the receiver, we are now in a position to discuss some possible sources of error. We shall follow the signal from the probe through the receiver.

C.1.1. VCO drift induced offset

There are two kinds of error attributable to VCO drift: offset in the amplifier chain, and changes in the slope of the frequency/voltage curve.
Suppose that the center frequency of the probe VCO and the center frequency of the PLL VCO are identically set. The implication of this is that the output of the receiver PLL will be zero for a null input. Now, if one of the two VCOs in

the system drifts, so that its center frequency no longer matches the other, the output of the receiver VCO will no longer be zero for zero input. Either the probe VCO will be off-frequency, so that the PLL must generate a steady-state offset to compensate, or the PLL center frequency is no longer the frequency corresponding to zero input current, in which case an error voltage must be developed in the PLL to hold lock.

In either case, these problems of drift-induced offset can be solved by ac coupling the receiver amplifier ahead of the synchronous detector. Provided that the waveform of the received signal is symmetrical, ac coupling will ensure that these center-frequency drifts have no effect. This is because the average value of a symmetrical waveform is zero, and ac coupled stages operate about an average value. The question of the reasonableness of the assumption of waveform symmetry is discussed later.

C.1.2. VCO slope changes

Another possible effect of VCO drift is that the slope of the VCO frequency/voltage curve will change. Should this happen, the apparent gain of the system (k in equations C-10 and C-11) would change.

Unlike the effect of center frequency drift, there is no simple cure for this condition. If the slope change were accompanied by a proportional change in the center frequency, the drift could be detected and compensated for in the electronics, but if the VCO gain were to change without a change in the center frequency, there would be no way to detect it.

A way to minimize the effects of this kind of error is to design the probe VCO and the PLL to track one another. Then, as environmental conditions changed and caused one oscillator to drift, the other would (presumably) drift similarly and compensate. Possible VCO nonlinearity provides additional reasons for seeking to have the two oscillators identical.

C.1.3. VCO nonlinearity

The design of modern integrated-circuit RC oscillators is such that they are inherently reasonably linear. However, their linearity is never perfect. Nonlinearities in the VCO or PLL stage can have the effect of producing an asymmetrical waveform from a sinusoidal input current (which can affect the output from a synchronous switch). Extreme nonlinearity can result in clipping, and consequent reduction of dynamic range.

Slight nonlinearities are probably unimportant in the kind of application envisioned here; severe nonlinearities probably cannot be tolerated. Minor nonlinearities can be compensated for by arranging for the receiver PLL oscillator to track the probe VCO nonlinearities. This can be done if the voltage to frequency curve of the probe VCO is the complement of the frequency to voltage curve of the receiver PLL.

Provided the input range is within reasonable limits, nonlinearities in the two curves compensate for one another. Outside the range over which the two curves match, nonlinearities and asymmetries will persist.

C.1.4. Frequency to voltage conversion

A voltage controlled oscillator can respond rapidly to a change in the control voltage. If the VCO frequency is much higher than the modulating frequency, this process is not particularly noisy, and no great error results from the representation of a voltage by a frequency. As the two frequencies become closer, errors are incurred. The process of regenerating the modulating signal is inherently noisy, and becomes noisier as the modulation frequency approaches the carrier frequency. In the case of a frequency modulated carrier, the modulation is usually only a few percent of the carrier frequency. In the case of our VCO, the modulation can cause the instantaneous frequency of the carrier to go to zero. Before this condition is reached, the incoming pulses are far apart in time, and no simple signal processing system can recover the modulation without error. The VCO/PLL approach is no exception; the only way to hold the frequency to voltage conversion noise to a reasonable value is to keep the modulation to a reasonable level.

C.1.5. Phase detector

The wide range of fields, and hence frequencies on the data link, does present some problems as far as the design of the loop phase detector is concerned. Exclusive-OR type phase detectors cannot be operated reliably over such a wide range of frequencies, because they have the property that they can lock onto harmonics of the input signal. Since, in our application, harmonic lock would present problems, it must be avoided by the use of another kind of phase detector. A suitable phase detector is available in the CD4046 which we used in the receiver.

C.1.6. Non-symmetrical switching

In understanding the operation of the receiver, it is assumed that the synchronous detector operates symmetrically. That is to say, it is assumed that each detector is "on" for exactly half the time, and that the phase relationship between the two detectors is exactly 90°. If this is not the case, the asymmetry will cause an error dependent on the phase of the signal with respect to the switching waveform. The error can be minimized by making the switch operate as symmetrically as possible, and by ensuring a 90° phase relationship. The approach we used reduces this error to a very small value, about 1 part in 10^4.

C.1.7. Amplifier offset

Amplifier offset in the probe will result in an apparent drift in the center frequency of the probe VCO. The effect will be the same as discussed above under the heading "VCO drift induced offset".

Amplifier offset after the detector in the receiver has the effect of producing an offset error. The approach used was to hold the gain of the amplifiers following the synchronous switch to a minimum. The amplifiers preceding the switch are ac coupled, so that no dc offset is measured from them.

C.1.8. Synchronous noise

Random noise, that is to say, noise that is not correlated to the signal frequency, has no effect on the signal produced by a synchronous detector, except to introduce random noise into the output. The detector will read only the average value of such noise, and the average is zero. The noise remaning in the output will have a magnitude that varies as $1/\sqrt{\tau}$. Thus, the residual noise can be reduced to an arbitrary level if one is willing to wait long enough for a reading.

Ultimately, synchronous noise is the parameter that defines the dynamic range of the meter. While the magnitude of the maximum signal that can be measured is limited by the operating voltages in the data channel to a few volts, there is no such clearly defined limit to the minimum measurable voltage. Reducing the synchronous noise from a millivolt to 100 microvolts increases the dynamic range of the instrument by a factor of ten. Reducing the level to 10 microvolts furnishes an overall increase of a factor of 100. Clearly, reducing the level of synchronous noise can have a major effect on the system dynamic range.

There are a number of sources of synchronous noise.

In the probe itself, the rotation can cause vibrations at synchronous speed, the amplitude of which depends upon how well balanced it is. This, in turn, could cause synchronous noise at the output of the electronics, through a number of mechanisms. In the receiver, synchronous noise can be introduced by coupling between the reference pulse circuitry (which is operating mostly at synchronous frequency) and the data channel, or by the operation of some the phase locked loops in the measurement circuit.

Probe vibration can cause synchronous noise in two distinct ways. There is likely to be a small direct voltage (the input offset voltage) on the two sensor electrodes, because of the difference in base-emitter voltages of the transistors used in the first stage of the operational amplifier. In a stationary amplifier this voltage will only cause a small offset of the VCO frequency. However, if the probe vibrates mechanically, and if the capacitance between the electrodes and the probe body (essentially a local "ground") is modulated by the vibration, a small current will flow in the input circuit of the first amplifier, thereby modulating the VCO in exactly the same way as a genuine field. The effect is known as parametric modulation. Figure C-3 illustrates the point.

The electrode-ground capacitance is small (only a few picoFarads) and the offset voltage is small (millivolts) so that the overall effect is very small. However, a guard ring was introduced between the electrodes and the body of the probe and was observed to reduce this noise source to an insignificant level.

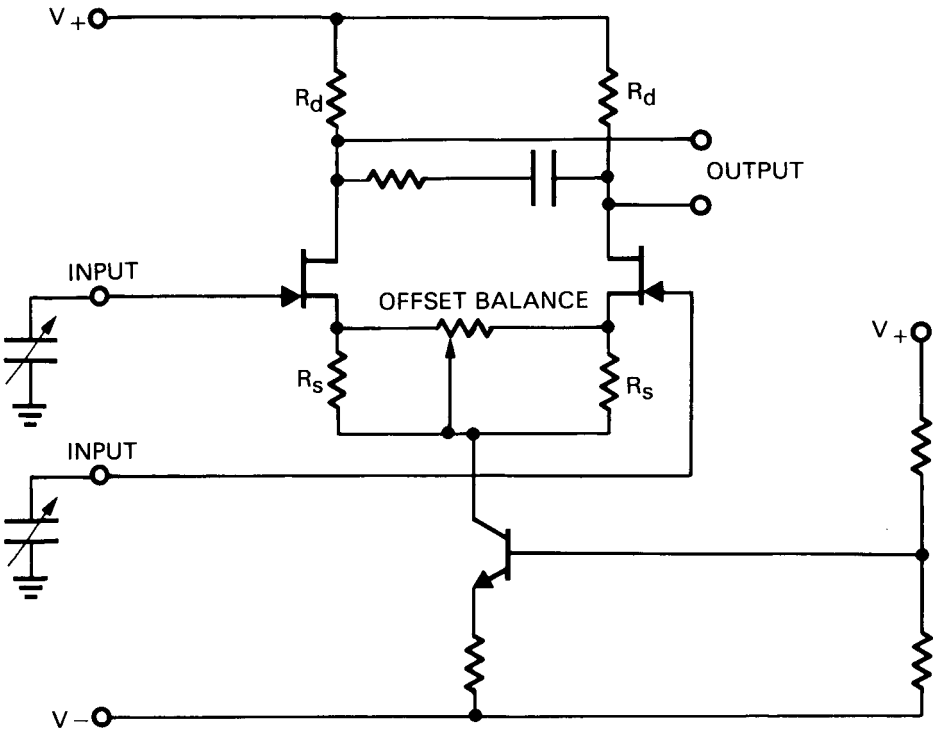

Figure C-3. Operational amplifier, showing parametric modulation of the input offset current.

The other way that probe vibration can increase the synchronous noise level is by direct modulation of the frequency-determining capacitance in the VCO stage. The most likely mechanism whereby this can occur is as a result of vibration in interconnecting wires. To reduce the effect of this vibration, the wires should be as short and as stiff as possible, so that the capacitance variation is minimized, and the fixed capacitance in the VCO circuit should be as large as practicable.

In a conventional field mill, synchronous noise is introduced by the slip-rings. There is no equivalent noise source in this design. The power margin in the data channel is large, and slight misalignment of the coupler between the rotating and non-rotating portions of the probe will only reduce this margin. A considerable alignment error can be tolerated before the effect is noticeable. However, if the error does become large enough, the receiver VCO will have difficulty in maintaining lock.

A synchronous reference pulse is transmitted over a separate fiber, and used to generate synchronous switching signals for the detectors. Since the pulse is transmitted once each revolution, much of the circuitry that processes it is exactly synchronous, and noise from that circuitry, coupled into the data link, could cause an increase in the receiver noise floor. The DOE field meter uses separate power supplies and separate printed circuit board grounds to minimize the amount of noise from this source.

In a conventional PLL, the phase detector is equivalent to a multiplier, and the lock range is maximized by driving the phase detector with symmetrical square waves (Gardner, 1966). Since the reference pulse is very narrow, the

required square wave must be generated by dividing the input pulse rate by two. However, the noise at a phase detector output is at twice the input frequency. If the conventional phase detector is used, and the input pulse rate is halved in order to maximize the lock range, the PLL will contain a component at synchronous frequency. This could only be reduced by filtering, and it is unlikely that it could be eliminated entirely.

A better approach, and the one finally used in the DOE field meter, is to use an edge-triggered type of phase detector. The division of the input frequency is then not required, and the lowest frequency of the noise in the output of the phase detector is twice the synchronous frequency. It is not necessary to filter this particularly well, since it will not affect the noise floor of the receiver.

C.1.9. Speed variation phase shift

One of the properties of a phase locked loop is that the frequency error is zero as long as the loop is locked. However, there can be a phase error. The magnitude of the phase error is proportional to the difference between the operating frequency and the loop center frequency, and inversely proportional to the PLL loop gain. In the field meter application, this kind of error can cause an apparent shift in the reference axis of the probe or, equivalently, a rotation of the field being measured.

The effect can be reduced by increasing the loop gain, and by making the measurements at a constant speed.

C.1.10. Non-flat frequency response

Unless the speed of the probe is held exactly constant by locking it to a reference source, probe and receiver designs should both be tolerant of small speed variations. This means that the frequency response of the various amplifiers must be quite flat over the range of frequencies of interest. In terms of an audio amplifier, a 1-dB non-flatness of response would be considered good. For a measurement system, this would represent an error of 11%. Consequently, considerable attention was given to the design of the amplifiers both in the probe and the receiver.

C.2. Physical Error Sources

C.2.1. Sources of non-symmetrical input current

When the probe is close to a conducting surface, the distribution of charge about the probe's equivalent conducting cylinder is not symmetrical. There will be an enhancement of the field, and hence an increased value of the charge, on the side closest to the conducting surface, as shown in Figure C-4. Figure C-5 shows the surface charge distribution as a function of angle. The question arises, do symmetrical electrodes passing through an asymmetrical field generate an asymmetrical current? Or conversely, do asymmetrical electrodes passing through a symmetrical field produce an asymmetrical current? The answer, paradoxically, is that neither situation will result in an asymmetrical input current.

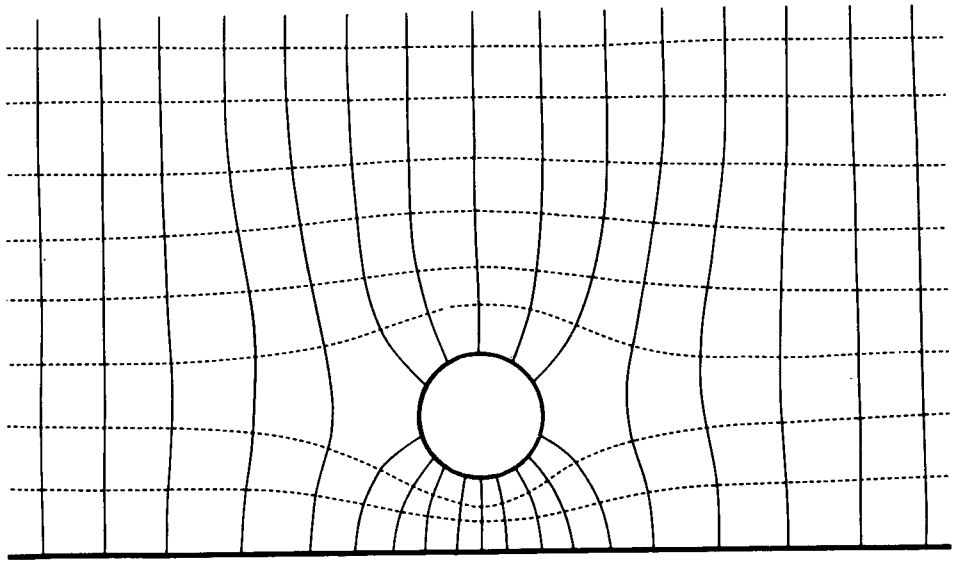

Figure C-4. The effect of asymmetrical field

In the case that the electrodes are symmetrical, the current flowing from electrode A to electrode B when A is uppermost is identical to the current flowing from B to A 180 degrees later. As a result, the output must be an odd function of the angle θ about its zero crossings, or more precisely $v(\theta) = -v(\theta+\pi)$. The two situations are identical, and cannot be distinguished in any way.

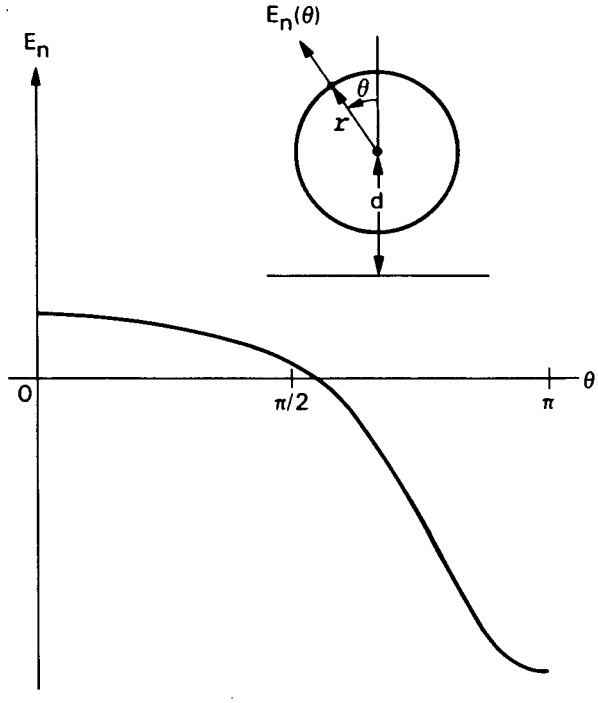

Figure C-5. The form of the surface charge distribution on a cylinder near a conducting surface.

The situation with two non-symmetrical electrodes is not so obvious, although the long term average of the output must still be zero if we restrict our attention to displacement currents (no ion current). Since there is no dc current source to either electrode, there must be no dc component out, regardless of electrode shape.

Figure C-6 shows the circumstances of interest.

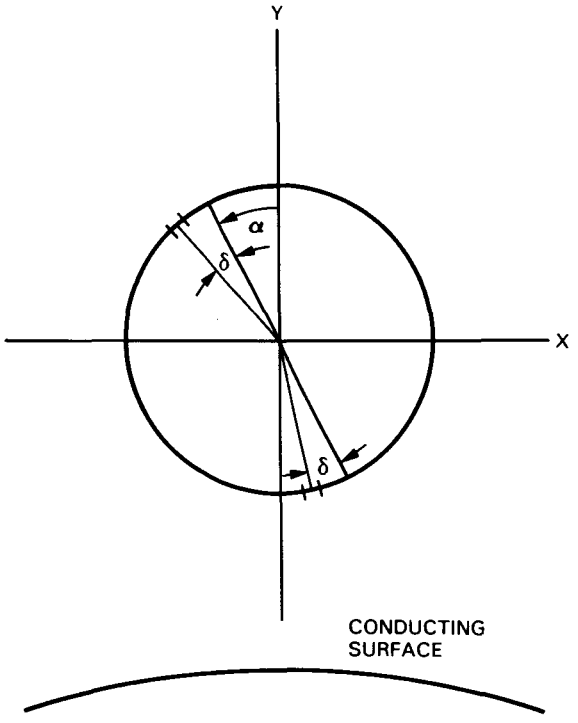

Figure C-6. Geometry for probe with non-symmetrical electrodes.

In general, the induced charge distribution on the cylinder can be given in terms of a Fourier expansion:

$$\sigma = \sum_{n=1}^{\infty} \sigma_n \cos n\theta \qquad \text{(C-12)}$$

The first term, n=1, gives the charge distribution that would be present in a uniform field E_y far from any other conductor. In such a case, $\sigma_n = 2\epsilon_o E_y$, and all other terms disappear. Near a conducting surface, higher harmonics will be present, even terms representing an asymmetrical distribution peaked on the bottom of the cylinder near the conducting surface, and odd terms representing a peaked distribution with top to bottom symmetry. Choosing a cosine series as defined above implies left-right symmetry, but if the nearby conductor and therefore the field did not have left-right symmetry, the analysis could easily be extended by including sin $n\theta$ terms.

The angle α specifies the orientation of the electrode pair. For a constant rotational rate, $\alpha = \omega t$. The electrodes are assumed to be split unequally, one electrode subtending an angle $\pi + 2\delta$ and the other $\pi - 2\delta$. The angle δ is assumed to be small.

If the charge on each electrode is now computed by integrating the expression given above for σ over each electrode, one obtains the result

$$q_a = -\,q_b = \sum_{n\ \text{odd}} \frac{2r\sigma_n}{n} \sin n\alpha + \sum_{n\ \text{even}} 2a\delta\sigma_n \cos n\alpha \qquad \text{(C-13)}$$

where r is the radius. Note that the second series is linear in the angular asymmetry δ, and is therefore like an error term. For symmetrical electrodes in a uniform field, only the leading term of the sin $n\alpha$ series remains, and

$$q_a = 2r\sigma_1 \sin \alpha = 4\epsilon_o r E_y \sin \omega t \qquad \text{(C-14)}$$

in agreement with our earlier analysis of sensor output. The restriction to odd terms confirms the expected inversion symmetry of the output already mentioned.

The waveform of the output, which is proportional to q_a with α replaced by ωt, is also seen to be less peaked than the original charge density $\sigma(\theta)$, in agreement with our experimental observations.

Additional simplification results from the phase sensitive detection used in the receiving electronics. The reference signal used in the phase sensitive detector is derived from a reference marker fixed in the electrode structure, which means that only the leading term in the sin $n\alpha$ series is measured. The phase sensitive detector rejects all harmonics, and since the leading term of the cosine series is at $2\omega t$ there will be no response dependent on δ. A scale factor error, proportional to δ^2 has been neglected by assuming δ to be small. If that assumption is not made, a factor cosδ appears in the leading sinα term.

Note that the rejection of the higher harmonic terms by the receiver circuit does not eliminate the error caused by a nearby conducting surface. The presence of the nearby conductor modifies the fundamental term representing the uniform field component around the cylinder, as well as introducing asymmetry represented by the higher order terms.

C.2.2. Effect of self-charging

Charge collection is a potential error source which is unique to an electrically isolated dc probe, since charging is not possible in a sensor mounted in the ground plane, and is not detected by an ac device. We have therefore examined this error source in some detail.

In this section, we discuss the nature of the problem, some experimental work involving pole leakage, and theoretical and experimental estimates of the expected error in a space charge environment.

The effect of charge collected on the probe can be easily visualized by realizing that the charge must be accompanied by an "image" charge reflected in any nearby conductive surface. It is easier to consider a charge and its image than a charge and a surface. The image charge or charges, together with the real charge on the probe, creates the same field as the probe charge and conductive surface would. The charge on the sensor itself is not sensed, a conclusion that can be reached through a symmetry argument. However, the field of all the image charges is added to the field to be measured and creates an error. The error is important only near a conducting surface; the field due to the image will be larger as the distance is reduced. Unfortunately, a theoretical estimate based on images is intractable, involving problems with slow convergence. Instead, we undertook a theoretical calculation, discussed below, that was based on a finite element numerical technique in which the sensor potential is used as the measure of the amount of collected charge.

In an ion current field, the sensor at space potential (the potential that existed in the undisturbed field at the location of the sensor axis before the sensor was introduced) will collect charge. However, the amount of charge collected is self-limiting. The total field is the sum of the original field and the field due to the collected charge. On one side of the probe, these fields will be additive; on the opposite side they will cancel. No further charge can collect when the outward (repelling) field from the probe cylinder becomes equal to (and cancels) the ambient field at the point on the cylinder nearest the source of ions. In typical ion current density, such as that expected under an HVdc line, the charging current is quite large and electrostatic equilibrium would be reached quickly, in less than 1 second.

The potential reached by the probe when fully charged differs from the free space potential by an amount of the order of the potential drop in the ambient field across the diameter of the probe. This fully charged condition was assumed in the calculations described below. This phenomenon has been treated in papers about the use of fine wire probes to measure potential in an ionized gas.

C.2.2.1. Pole leakage

However, if a current reaches the probe by some other means, such as resistive current leakage to ground, then no potential limiting mechanism operates. The probe can conceivably become charged beyond the fully charged potential in an environment containing only one ion species (i.e., all positive or all negative).

During the development of the test cage at JPL, an experiment was performed to examine the uniformity of the field near the guard rings, using the field meter. Large errors were encountered. These were traced to electrical leakage along the pole that was used to support the probe. In these tests, the probe was located near the high-voltage electrode of the cage, while the opposite

electrode was grounded. Thus, the space potential at the sensor location was nearly equal to that of the high potential electrode. The sensor was partially grounded by the leaky pole. It was this leakage that created the error.

C.2.3. Conclusions

An error is introduced when the charged sensor approaches a conductor, but with good electrical isolation in a space charge environment, the charge and the resultant error will be limited. Under these conditions, the error can be predicted and is given in our earlier paper (Johnston *et al.*, 1986). The error will not exceed 10% at a distance of 5 probe radii from the surface. This is an important reason for preferring a small probe; another being to enable convenient access to a restricted space or irregularly shaped structures. If we can be assured that the probe is isolated and coupled to an ambient space charge, reliable measurements are possible.

However, other effects, such as electrical leakage along the supporting pole can create large errors, especially near a charged electrode. These errors are likely to be more troublesome in a region without space charge or with very small space charge, because the probe potential will be undetermined. The use of a small polonium-α source, in the range of 0.01 to 0.1 microcurie, attached to the sensor housing, was found to eliminate this problem. Care must be taken to ensure the supporting pole is a good dielectric, and the alpha-source intensity must be of the correct magnitude, especially at low field strength. With these two precautions, reliable measurements will be possible, even without ambient space charge.

APPENDIX D

ADDITIONAL EQUIPMENT

APPENDIX D. ADDITIONAL EQUIPMENT

In addition to the electric field cage, several accessories for the sensors were also designed and built. They will be briefly described.

D.1. Universal Field Probe Breadboard

The field probe electronics, complete with a fiber optic output, was duplicated on a breadboard as a design aid for both ac and dc sensors. By simply changing a "plug in" on the breadboard, which contains the amplifier feedback and VCO R-C components, it can emulate the low-field dc probe, the high-field dc probe or the ac probe. This non-spinning version is useful for verifying such things as VCO center frequency, probe power consumption or optical data link operation. The system is used by coupling the input to the breadboard's integrating amplifier to a signal generator. Figure D-1 shows the arrangement.

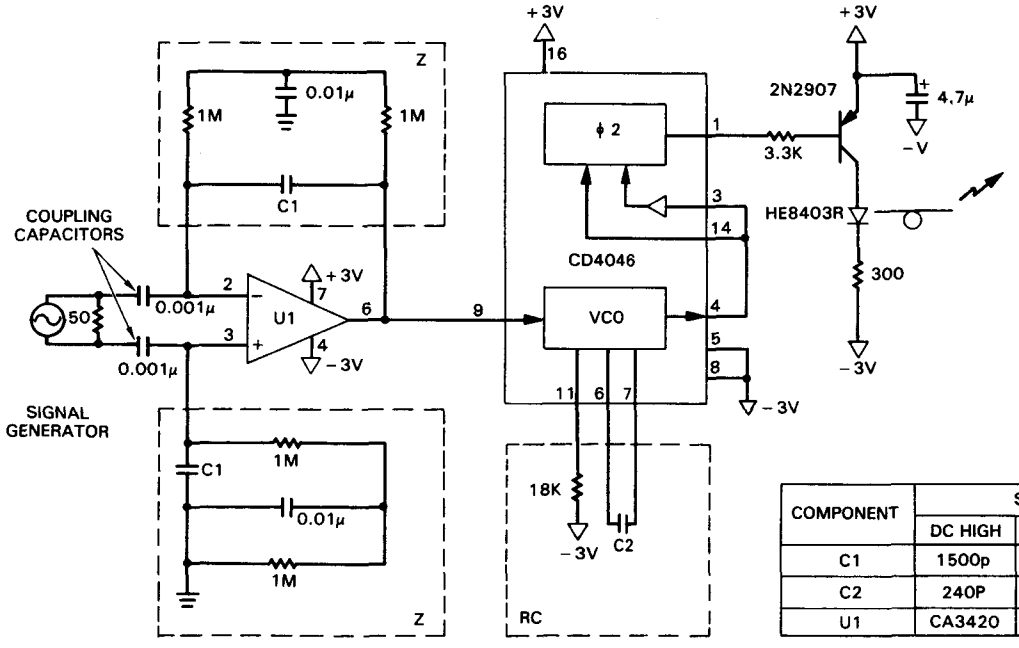

COMPONENT	SENSOR TYPE		
	DC HIGH	DC LOW	AC
C1	1500p	0.01μ	0.01μ
C2	240P	240P	2200p
U1	CA3420	CA3420	OP20

Figure D-1. Universal breadboard

D.2. DC Probe Simulator

A dc probe simulator was built to enable the receiver to be tested without having to spin the probe or create an electric field. The battery operated simulator can be used in the laboratory or field to check receiver performance and calibration. It has optical data and position outputs which closely model the output characteristics of the probe, and it is connected to the receiver via fiber optic cables. The magnitude of the data signal, the phase of the reference signal, and the frequency (common to both signals) can be adjusted from the front panel. The design of the probe simulator is shown in the block diagram of Figure D-2, and in the schematic of Figure D-3.

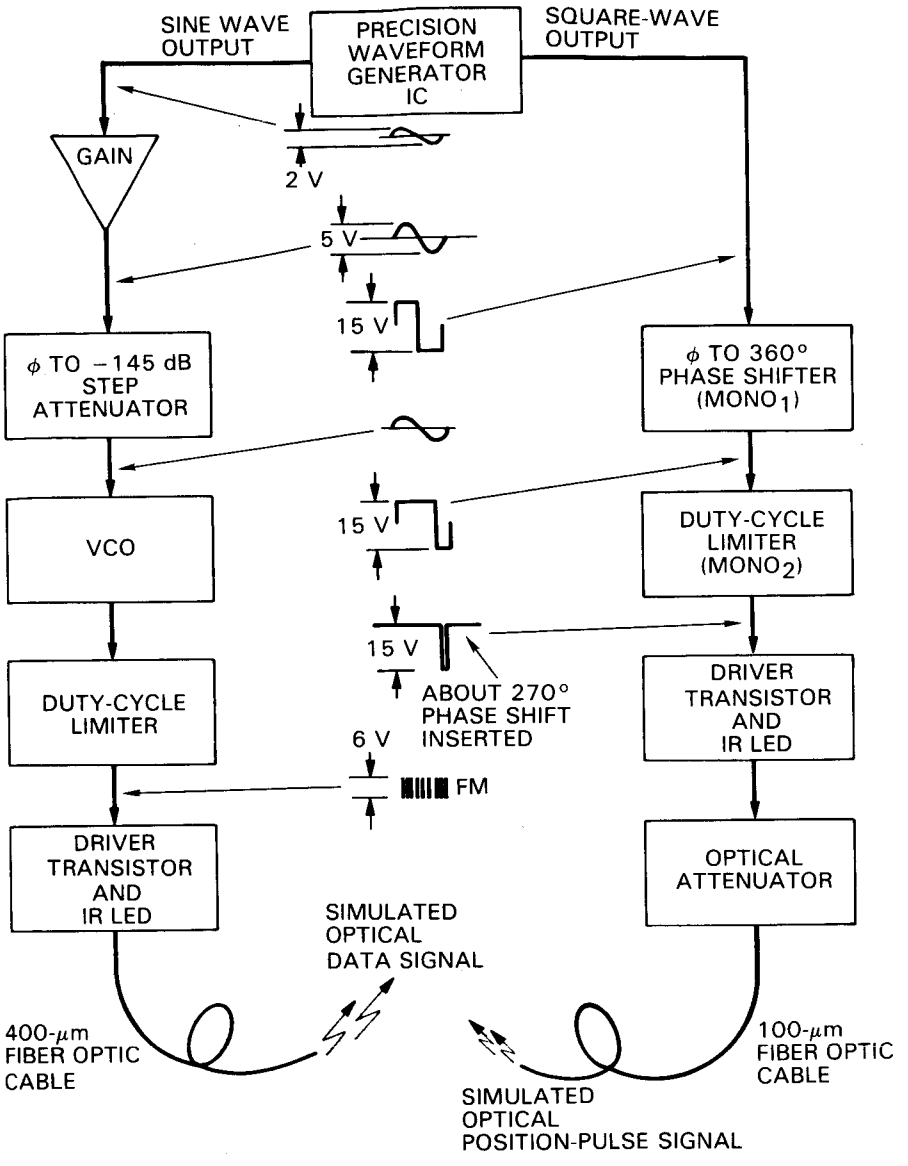

Figure D-2. Block diagram of probe simulator

The three main sections of the simulator are the common waveform generator, the magnitude (data) channel, and the position reference channel.

An ICL 8038 precision waveform generator, U1 in Figure D-3, produces the sine wave used in the data channel as well as the synchronous square wave used in the reference channel. The generator frequency can be varied from 300 to 600 Hz, corresponding to probe speeds of 18 to 36 krpm.

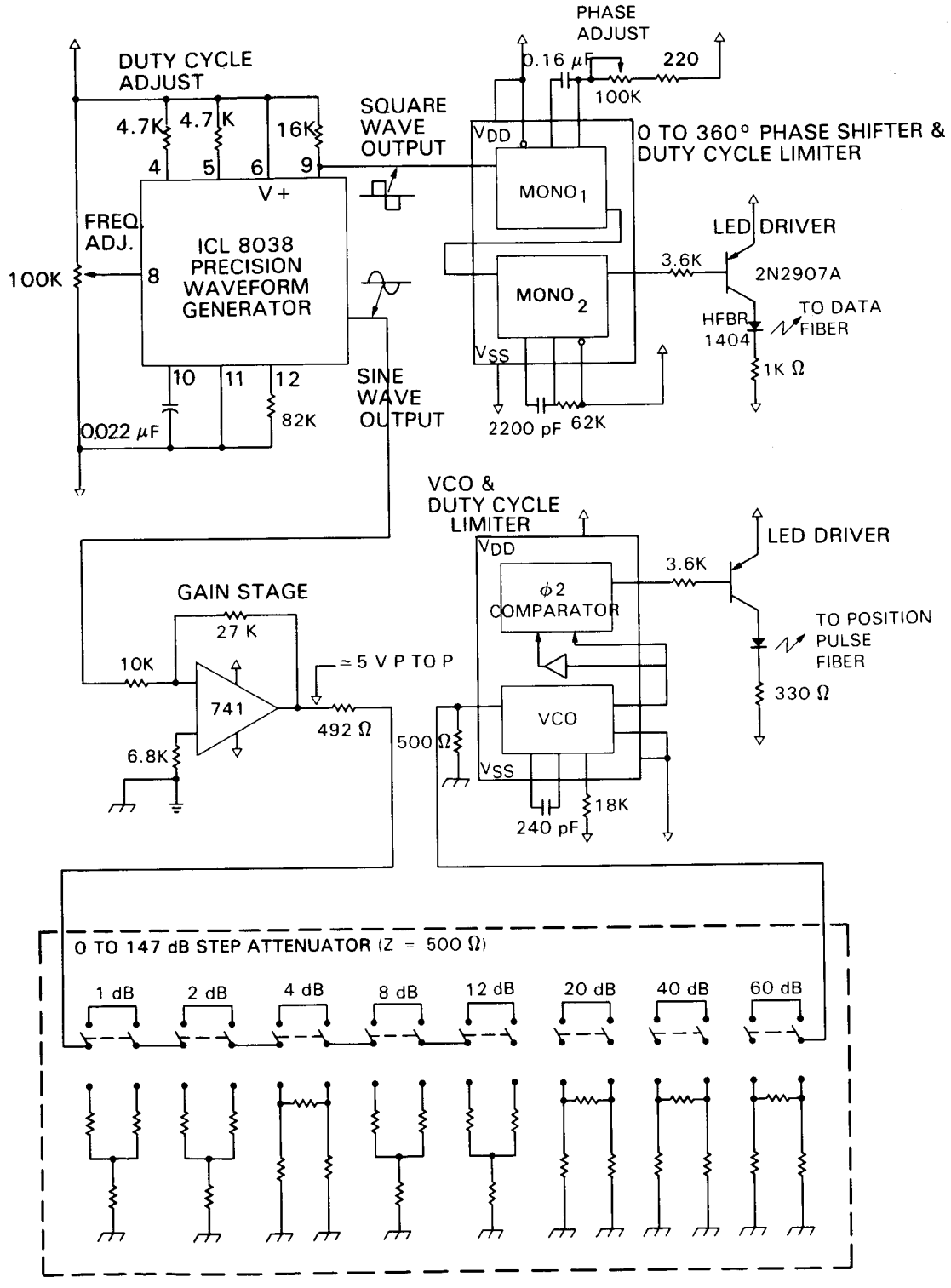

Figure D-3. Circuit of probe simulator

In the data channel, the sine wave output from the generator is amplified by A1 and applied to the input of a calibrated attenuator providing 0-147 dB of attenuation in 1 dB steps. This output modulates the VCO of U2, using the same supply levels and R-C components as the probe. The phase detector in U2 shortens the duty-cycle of the VCO's output, which is then amplified by transistor Q1 to drive an LED coupled to a 400 micron fiber optic cable.

In the reference channel, a dual monostable, U3, is used to convert the generator's square wave to a short pulse and to vary its phase with respect to the sine wave. The pulse is then amplified by transistor Q2 to drive a second LED coupled into a 100 micron fiber optic cable.

D.3. Zero-Field Shield For the DC Probe

The ambient dc electric fields found in the laboratory environment can be of the order of tens of volts per meter. For this reason it was necessary to build a special shield for the probe in order to study the performance of the meter with no applied field.

A shield can measuring five inches in diameter and three inches in length was built to enclose the probe. Using this shield, a 100-μV noise was isolated, thought to be caused by capacitive coupling between the probe electrodes (through its fiberglass shell) and the irregular shape of the turbine housing. By redesigning the turbine housing for a uniform outer surface, and applying conductive paint to the inside of the shell, the noise was reduced to less than 2 μV. This translates into an equivalent increase in the dynamic range of the probe. The shield is shown in Figure D-4.

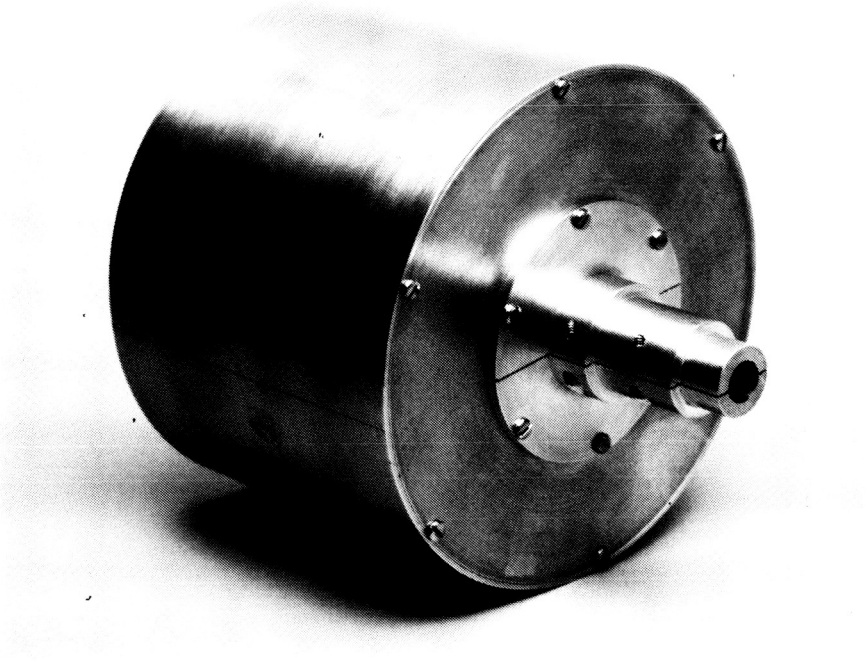

Figure D-4. Zero-field shield for dc probe

D.4. Micro Field Cage

A tiny portable electric field cage was designed, primarily for demonstrations of the field probes (excluding the beer can probe, of course). The cage consists of two 8 inch square parallel copper plates separated by the convenient distance of 10.0 centimeters. The plates are fastened to plexiglass sheets held in position with slotted plexiglass rods, top and bottom. Figure D-5 shows the assembled cage.

A 1.2-kV/m ac field can be produced in the micro cage by merely attaching the power line cord (incorporating series safety resistors) and plugging the device into a wall outlet. The facility to measure the applied voltage is also provided.

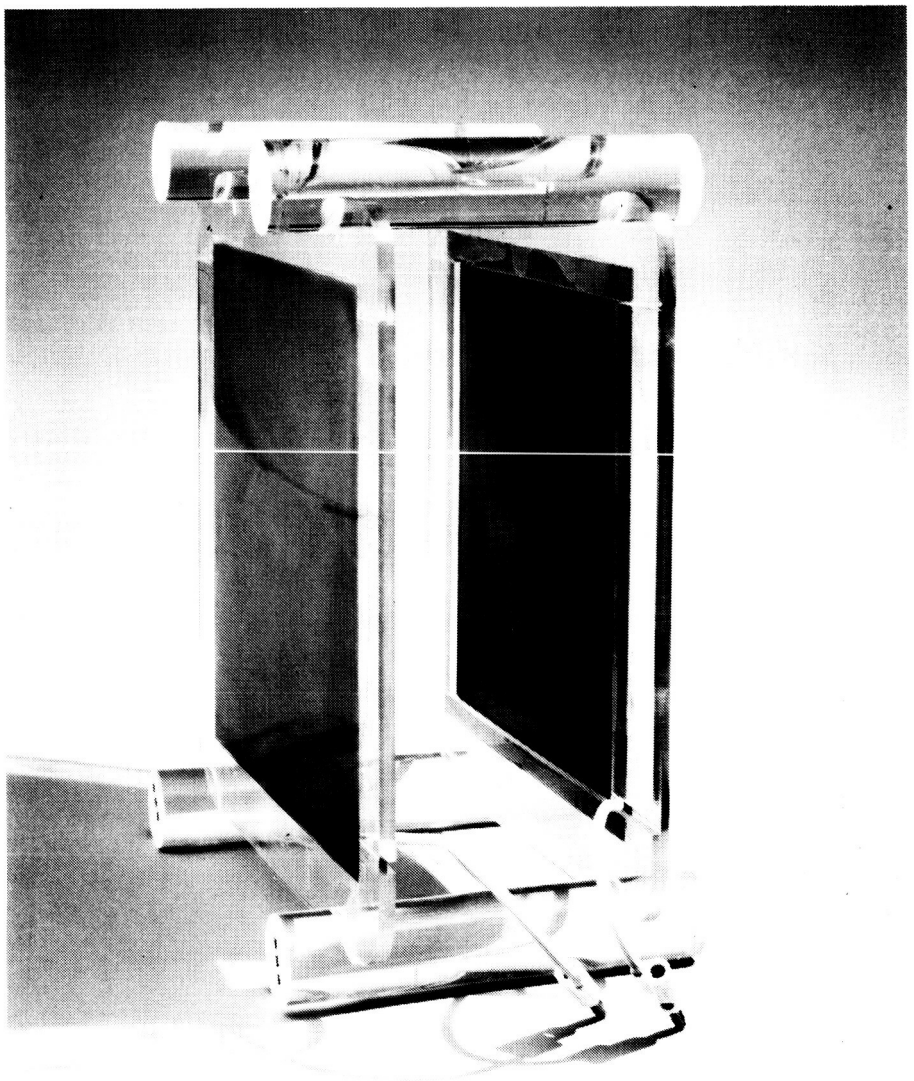

Figure D-5. Micro-cage

BIBLIOGRAPHY

BIBLIOGRAPHY

Anderson, J.G., and Doyle, J.R., (1975), "Project UHV—A Transmission Research Facility", Transmission Line Reference Book, 345 kV and Above, Electric Power Research Institute, Palo Alto, California.

Comber, M.G., and Johnson, G.B., (1982), "HVDC Field and Ion Effects Research at Project UHV: Results of Electric Field and Ion Current Measurements", IEEE Transactions on Power Apparatus and Systems, PAS-101 No. 7, pages 1998-2006.

Comber, M.G., Kotter, R., and McKnight, R., (1983, November), "Experimental Evaluation of Instruments for Measuring DC Transmission Line Electric Fields and Ion Currents", IEEE Transactions on Power Apparatus and Systems, PAS-102 No. 11 pages 3549-3557.

Crow, Auer, and Allen, (1975, August), "The Expansion of a Plasma into a Vacuum", Journal of Plasma Physics, No. 14, pages 65-76.

Deno, D.W., and Zaffanella, L.F., (1975), Electrostatic Effects of Overhead Transmission Lines and Stations", Transmission Line Reference Book, 345 kV and Above, Electric Power Research Institute, Palo Alto, California.

Feser, K., and Pfaff, W., (1984, October), "A Potential-Free Spherical Sensor for the Measurement of Transient Electric Fields", IEEE Transactions on Power Apparatus and Systems, PAS-103, No. 10, pages 2904-2911.

Friedmann, D.E., Curzon, F.L., Feeley, M., Young, J.F., and Auchinleck, G., (1982, August), "Electric Field Meter Based on the Breakdown of Gases", Review of Scientific Instruments, Vol 53, No. 8, pages 1273-1277.

Gardner, F.M., (1966), Phaselock Techniques, John Wiley and Sons, New York.

Gathman, S., (1968, January), "Guarded Double Field Meter", Review of Scientific Instruments, Vol. 39, No. 1, pages 43-47.

Gilchriest, C.E., (1957, January), "The Application of Phase Locked Loop Discriminators for Threshold Improvement and Error Reduction in FM/FM Telemetry", JPL Publication No. 364, Jet Propulsion Laboratory, Pasadena, California.

Gorakhpurwalla, H.D., Cooper, E.H. and Johnson, M.J., (1984), "A Spherical Dipole Probe System (SDPS) for the Measurement of Electric Fields from 30 Hz - 1 MHz", Transactions of IEEE National Symposium on Electromagnetic Compatibility: EMC in the Next Quarter Century, pages 171-179.

Lampert, M.A., and Mark, P., (1970), Current Injection in Solids, Academic Press, New York, New York.

Many, A., and Rakavy, G.,(1962), Physics Review, No. 126, page 1980 *et seq*.

Maruvada, P.S., Dallaire, R.D., and Pednault, R., (1983, March), "Development of Field Mill Instruments for Ground Level and above-ground Electric Field Measurement under HVDC Transmission Lines", IEEE Transactions on Power Apparatus and Systems, PAS-102 No. 3, pages 738-744.

Misakian, M., (1981, May), "Generation and Measurement of D.C. Electric Fields with Space Charge", Journal of Applied Physics Vol. 52, No. 5, pages 3135-3144.

Misakian, M.S., Kotter, F.R., and Kahler, R., (1978, July), "Miniature ELF Electric Field Probe", Review of Scientific Instruments, Vol. 49, No. 7, pages 933-935.

Johnston, A.R., Kirkham, H. and Eng, B.T., (1986, November), "DC Electric Field Meter with Fiber Optic Readout", Review of Scientific Instruments, Vol 57, No 11, pages 2746-2753.

Kirkham, H., Johnston, A.R., Lutes, G., Daud, T. and Hyland, S., (1984, March), "Power System Applications of Fiber optics", JPL Publication 84-28, Jet Propulsion Laboratory, Pasadena, California.

Silvester, P., (1969), "Higher Order Polynomial Triangle Finite Elements for Potential Problems", International Journal of Engineering Science, No. 7, pages 849-861.

Smiddy, M., and Chalmers, J.A., (1958)," The Double Field Mill", Journal of Atmospheric and Terrestrial Physics, Vol. 12, pages 206-210.

Takuma, T., Kawamoto, T., and Sunaga, Y., (1985, February), "Analysis of Calibration Arrangements for AC Field Strength Meters", IEEE Transactions on Power Apparatus and Systems, PAS-104, No. 2, pages 489-496.

Wilhelmy, L., (1983), "Eine Sonde zur potentialfreien Messung der periodischen und transienten elektrischen Feldstärke", Elektrotechnische Zeitschrift, Vol. A94, No. 8, pages 441-445.

Zahn, M., (1976), "Transient Drift-Dominated Unipolar Conduction Between Concentric Cylinders and Spheres", IEEE Transactions on Electrical Insulation, Vol. EI-11, No. 4, pages 150-157.

Zahn, M. (1977), "Transient Drift-Dominated Conduction in Dielectrics", IEEE Transactions on Electrical Insulation, Vol. EI-12, No. 2, pages 176-190.

Zahn, M. and Pao, S.C., (1975), "Effects of Step Changes in Excitation from a Steady State on the Transient Electric Field and Space Cahrge Behavior for Unipolar Ion Conduction; I. Step Changes in Current, II. Step Changes in Voltage", Journal of Electrostatics, No. 3, pages 235-264.

Zahn, M., Pao, S.C. and Tsang, C.F., (1976), "Effects of Excitation Risetime and Charge Injection Conditions on the Transient Field and Charge Behavior for Unipolar Ion Conduction", Journal of Electrostatics, No. 2, pages 59-78.

Zahn, M., Tsang, C.F. and Pao, S.C., (1974), "Transient Electric Field and Space Charge Behavior for Unipolar Ion Conduction" Journal of Applied Physics, No. 45, pages 2432-2440.